REDOX PROCESSES IN SULFIDE MINERALS

by

Devon John Renock

A dissertation submitted in partial fulfillment
of the requirements for the degree of
Doctor of Philosophy
(Geology)
in The University of Michigan
2010

Doctoral Committee:

Associate Professor Udo Becker, Chair
Professor Rodney C. Ewing
Professor Kim Hayes
Professor Stephen E. Kesler
Assistant Professor Greg Dick

For Bevin and Max

and, of course, William H.

ACKNOWLEDGMENTS

Five years ago I decided to quit my job at a company in Ann Arbor and pursue my longtime dream of a graduate degree in geology. I would not have been able to take this step without the love and support of my wife, Bevin. Her patience and encouragement has meant everything to me these last few years. My son Max was born three weeks ago and he has been at my side for every late night writing session since (in between diapers, bottles, and burps, of course). He has been a source of inspiration and great joy, and we are so thankful that he has arrived in our lives. My parents and my family have always been there for me, and I am ever grateful for their love and support.

In my years at Michigan, I am so fortunate to have been able to be mentored scientifically, professionally, and personally by my advisors, Udo Becker and Rod Ewing. It has been a privilege to study in their research group. They have provided me with incredible opportunities and given me a strong foundation from which to launch my own academic career. Most importantly, they have become good friends to me and my family. The rest of my thesis committee has also been very supportive of my work. I acknowledge Kim Hayes for encouraging me to develop collaboration with his research group in order to characterize mackinawite nanoparticles. I have had the opportunity to interact with Steve Kesler on the geology of noble metal incorporation in galena and pyrite and he has been a wealth of insightful ideas and comments.

I am also grateful to Greg Dick for agreeing to join my committee in the final few months to review my manuscript.

I am very appreciative of Tanya Gallegos from the Department of Civil and Environmental Engineering who provided numerous samples of mackinawite and many hours of good discussion that resulted in our Chemical Geology paper. My special thanks go to Dr. Satoshi Utsunomiya for the numerous Saturday mornings we spent on the transmission microscope together. He is one of the most talented scientists I have ever had the pleasure to work with. Haiping Sun and Kai Sun at the North Campus EMAL were also instrumental in helping me with my XPS analyses.

Many other faculty and staff contributed to this work. My conversations and collaborations with Artur Deditius on arsenian pyrite contributed to many of the ideas that went into the galena work. I have to thank Martin Reich for helping to get me started on the calculations about coupled substitutions in sulfides. Lindsay Shuller has been a valuable resource regarding computational simulations, a confidante, a lunch buddy, and a great friend during my time here. Janine Taylor and Mike Messina helped with all of my computer and networking problems. Carl Henderson was a valuable resource for me in EMAL. Nancy Kingsbury and Anne Hudon were invaluable in all things nonscience. I should thank many of my colleagues in our research group for making my time here very rewarding. These include Elizabeth Ferriss, Frannie Skomurski, Chintalapalle Ramana, Darius Dixon, Subhashis Biswas, Qiaona Hu, Maik Lang, Jianwei Wang, Stephen Crabtree, Nadja Insel, Alex Janevski, and Jiaming Zhang.

TABLE OF CONTENTS

LIST OF FIGURES

LIST OF TABLES

Chapter 1

Introduction

Sulfide minerals have historically been of great interest to geoscientists and mineralogists because they are a major host for noble and heavy metals. Determining the fundamental chemistry of sulfide minerals is key to understanding their conditions of formation and, hence, the geological processes that affect the distribution of precious metals in their structures. For example, galena, PbS, can accommodate significant quantities of Ag through a coupled substitution mechanism with Sb and/or Bi. In Carlin-type deposits, Au is incorporated into arsenian pyrite, $Fe(S,As)_2$, in solid solution, and is aptly named "invisible" gold (Cook and Chryssoulis, 1990; Fleet *et al.*, 1993). The incorporation of Au in pyrite, FeS_2, is facilitated by As, and natural samples commonly have a maximum Au/As molar ratio of 0.02 (Reich *et al.*, 2005); above this ratio, Au exists as nanoparticles of metallic gold (Palenik *et al.*, 2004). The close association between Ag and Sb/Bi in PbS, and Au and As in FeS_2 are well known, but the atomic-level processes responsible for these associations are far from being understood.

Recently, interest in sulfides has focused on two additional areas: 1) environmental mineralogy/geochemistry, and 2) geomicrobiology. The former is driven by the need to

understand and mitigate the environmental consequences of human activities, such as acid mine drainage (*i.e.,* the oxidation of sulfides and the subsequent release of acid and toxic elements, such as heavy metal and arsenic into natural waters). The latter involves understanding how microorganisms interact with sulfides, either as part of their metabolic activities or as part of some other function (e.g., the use of magnetic minerals like greigite, Fe_3S_4, for navigation by magnetotactic bacteria). This also includes exciting research into surface catalyzing reactions that form complex organic molecules, and the possibility that life on this planet emerged from the surface of a sulfide mineral.

The importance of sulfides comes from their role (either direct or indirect) in many redox-based geochemical and biogeochemical processes. Many sulfides are electroactive, and thus act as electron sources and sinks, which control the availability of electrons in near-surface environments. The redox potentials that develop on their mineral surfaces establish potential gradients (either through the thin films of water adsorbed to them or the microbial communities that cover their surfaces) that drive a wide range of geochemical processes.

The semiconducting-to-metallic nature of some main group sulfides (e.g., galena, and realgar, As_4S_4) and the presence of *d* electrons in sulfides of transition metals (e.g., mackinawite, FeS, and pyrite) impart them with unique bulk and surface properties (e.g., electrical, magnetic, and optical). It is for this reason that there is extensive cross-disciplinary interest in sulfide materials in chemistry, physics, and materials science. In terms of practical application, the goal is to harness the unique electrical and magnetic properties of synthetic sulfides (mineral analogs) for use in electronic devices (e.g., optical devices, photovoltaic cells, photodiodes, and magnetic recording devices) as well

as in thin film and nanotechnology applications (e.g., heterogeneous catalysts, solid-state sensors). The potential synergies between geosciences and the other disciplines in sulfide research are exciting. One such example is how kinetic barriers that influence the rate of oxidation of pyrite or arsenic sulfides, and the subsequent release of acid drainage, may be of similar mechanistic origin to the kinetic barriers that heterogeneous catalyst developers seek to overcome, and that presently hinder the widespread-adoption of fuel-cell technologies, for instance.

In the geosciences, utilizing the electronic and magnetic properties of sulfides has traditionally been the domain of the geomagnetism, paleomagnetism, and the mining and mineral-processing communities. Therefore, the literature in these fields is extensive. However, the emerging fields of environmental mineralogy/geochemistry and geomicrobiology are beginning to reveal the important role that sulfides (and sulfide nanoparticles) play in the geochemical cycling and mobility of the elements in the near-surface environment.

Whether it is a natural sulfide mineral, a synthetic mineral-like material in an environmental application, or a synthetic catalyst in a fuel cell device, redox interactions with gases and liquids occur strictly through the surface interface. The mobility of elements in the near-surface environment of the Earth depends mainly on reactions that occur at the surfaces of minerals. The mechanisms responsible for the transfer of electrons from anodic to cathodic sites on a surface are directly influenced by the arrangement of atoms on the surface, as well as the electronic and magnetic properties of the mineral surface. **Despite many decades of research, the key controls of mechanisms and, hence, the rates of some of the most environmentally important**

redox mechanisms are poorly understood. This is largely because these processes almost always involve a complex series of elementary reactions, each involving the transfer of one electron at a time. For example, the oxidation of monosulfides (e.g., galena, mackinawite, and realgar) and disulfides (e.g., pyrite and arsenian pyrite) to form sulfate ions requires as many as eight and seven one-electron transfer steps, respectively. Not only are the mechanisms themselves complicated, but also the semiconducting nature of the mineral surface allows for the possibility of unique behavior such as the coupling of spatially separated redox species by electron transfer through near surface layers (Becker *et al.,* 2001). An additional complication is that many sulfide mineral surfaces (especially those with more covalent bond character) can differ greatly from a model that assumes a simple truncation of the bulk crystal structure. Often, distortions or reconstructions in the near-surface layers produce defects in order to stabilize the surface. In these cases, the surface presents a significant perturbation of the electronic structure of the bulk in the near-surface layers. Surface electronic states that result from surface reconstruction, defects, vacancies, adsorbates, and discrete surface phases dominate the initial stages of surface chemical behavior. For example, step edges on galena (PbS) and monoclinic pyrrhotite (Fe_7S_8) have been shown to be highly reactive redox sites, as compared with flat terraces (Becker and Rosso, 2001; Becker *et al.*, 1997). Studies have shown that deviations in the stoichiometry of surfaces (relative to the bulk), with concomitant deviations in electronic and magnetic properties, often influence surface reactivity (Vaughan *et al,.* 1997). For example, it is known that the rate of oxidation of the pyrrhotite surface is 20-100 times faster than the rate of oxidation of pyrite despite the fact that ferrous iron, Fe^{2+}, is only exposed at step edges, corners, and vacancies on the

surface of pyrrhotite. In contrast, Fe^{2+} is exposed all over the growth terraces of pyrite (Belzile *et al.*, 2004; Rimstidt and Vaughan, 2003). The difference in reactivity has been attributed to high spin Fe^{2+} in pyrrhotite being more reactive to paramagnetic O_2 than the low spin Fe^{2+} on pyrite terraces (Rosso *et al.*, 1999; Becker and Hochella, 1996). However, the fundamental reaction mechanisms responsible for these differences in reaction rates have not been described.

This dissertation is an investigation of molecular-scale processes underlying redox chemistry on iron and arsenic monosulfide nanoparticles (Chapters 2 and 3, respectively), and coupled substitution mechanisms within bulk galena (Chapter 4). Thus, two of the main questions to be addressed in this thesis are:

- How do the semiconducting properties of the surface or the bulk mediate interactions between adsorbates (or impurities within the bulk)?
- How do these interactions (*i.e.,* structural, electronic, and magnetic) influence the adsorption mechanism, thermodynamics, and kinetics of important geochemical processes?

The strength of my approach in describing atomic-level redox processes is the combination of experimental nanoscale-characterization and surface-sensitive techniques (*i.e.,* microbeam and spectroscopic techniques) and quantum-mechanical simulations to understand the observed processes. At the theory level, it is extremely important to treat the interface properties at the quantum-mechanical level. Only quantum mechanics, in contrast to empirical force-field methods, allows one to capture the unique semiconducting properties of these minerals. Empirical force fields provide some insight

into structural properties; however, information about the electronic and magnetic properties of these systems can only be deduced from *ab-initio* calculations. An explosion of parallel computing technology and development of faster and more efficient computer algorithms have lead to development of specialized *ab-initio* modeling tools for computational chemistry that are, within the last decade, starting to make headway in the geosciences. An excellent review of quantum-mechanical calculations of mineral surfaces as it applies specifically to the topic of this dissertation can be found in Rosso (2001).

We have applied a nanoscience approach to investigate redox mechanisms specific to three different sulfide systems:

Chapter 2 is an investigation into the uptake of dissolved As(III) by nanoparticles of a tetragonal iron (II) monosulfide, *i.e.,* mackinawite (designated FeS_m). **The impetus for investigating this system was to describe the changes in surface properties of mackinawite nanoparticles under different pH conditions and to determine how these changes affect the uptake mechanism of dissolved As(III).** When characterizing nanoparticles, it is crucial to apply appropriate experimental techniques that capture the structure, the chemistry, and, as a consequence, the reactivity that occur at these interfaces at the atomic level. As an example, a major challenge to the development of a fundamental understanding of transport and retardation mechanisms of trace metal contaminants (<10 ppm) is their identification and characterization at the nanoscale. Atomic-scale techniques, such as conventional transmission electron microscopy (TEM), although powerful, are limited by the extremely small amounts of material that can be examined. In this study, advanced electron microscopy and surface-specific probe

techniques were employed to describe the pH dependent uptake mechanism for As(III) by mackinawite nanoparticles. The data presented here show that, at pH 5, As(III) is reduced on the surface of FeS as discrete nanoparticles of amorphous arsenic sulfide. This mechanism is shown to change at higher pH values where uptake is primarily due to the adsorption of As(III)-oxyanion surface complexes to the nanoparticles.

Chapter 3 builds on the results of Chapter 2 by investigating the oxidation of arsenic sulfide nanoparticles, specifically, a quantum-mechanical cluster approach is used to investigate proximity effects between co-adsorbates on As_4S_4 clusters (*i.e.,* the fundamental unit in the realgar molecular crystal as well as numerous other molecular arsenic sulfides). Proximity effects, whereby a chemical reaction at one surface site modifies the reactivity of a remote site several Angstroms or even nanometers away, have been shown in the literature to affect the oxidation thermodynamics of galena and pyrite surfaces (Rosso and Becker *et al.*, 2003). **The impetus for Chapter 3 was to extend the proximity-effect theory one step further to determine if interactions between co-adsorbates on a semiconductor surface could affect reaction mechanisms and oxidation kinetics.** The results of Chapter 3 provide new insights regarding the molecular-scale processes responsible for the oxidation of sulfide minerals. Two activated processes are shown to dominate the kinetics of As_4S_4 oxidation by molecular oxygen: 1) a triplet to singlet spin state transition, and 2) O_2 dissociation on the surface. Activation energy barriers due to spin transitions are rarely discussed in the literature as key factors controlling oxidation rates, even though the magnitude of these barriers is enough to alter the kinetics significantly. The results in this study will provide a new framework for evaluating the processes that underpin empirically-derived rate

expressions and may be an excellent tool for deriving macroscopic rate laws that are based on an atomistic understanding of reaction mechanisms and kinetic bottlenecks.

While chapter 3 investigates long-range co-adsorbate interactions on surfaces, Chapter 4 is a quantum-mechanical investigation of coupled substitution, and thus, electronic interactions in bulk galena. **The impetus for Chapter 4 was to determine if charge transfer between substituting cations in bulk galena can be responsible for clustering or "ordering" in solid solutions between Pb_2S_2 and end members with miargyrite ($AgSbS_2$) composition, matildite composition ($AgBiS_2$), or trechmannite ($AgAsS_2$) composition.** Total energies for different substitution configurations were used in Monte-Carlo calculations to derive the enthalpy of mixing (ΔH_{mix}), entropy of mixing (ΔS_{mix}), and free energy of mixing (ΔG_{mix}) at temperatures ranging from 200˚C to 700 ˚C. ΔG_{mix} was used to calculate phase diagrams that can be compared with experiment. Chapter 4 describes the first investigation of coupled substitution in a sulfide that is based on quantum-mechanical and subsequent Monte-Carlo methods. Therefore, it can be considered a new tool for investigating coupled substitution mechanisms in other economically-important sulfide and sulfosalt minerals.

References

Becker, U. and Hochella, M.F. (1996) The calculation of STM images, STS spectra, and XPS peak shifts for galena: New tools for understanding mineral surface chemistry. Geochimica et Cosmochimica Acta, 60, 2413-2426.

Becker, U., Munz, A.W., Lennie, A.R., Thornton, G., and Vaughan, D.J. (1997) The atomic and electronic structure of the (001) surface of monoclinic pyrrhotite (Fe_7S_8) as studied using STM, LEED and quantum mechanical calculations. Surface Science, 389, 66-87.

Becker, U. and Rosso, K.M. (2001) Step edges on galena (100): Probing the basis for defect driven surface reactivity at the atomic scale. American Mineralogist, 86, 862-870.

Becker, U., Rosso, K.M., and Hochella, M.F. (2001) The proximity effect on semiconducting mineral surfaces: A new aspect of mineral surface reactivity and surface complexation theory? Geochimica et Cosmochimica Acta, 65, 2641-2649.

Belzile, N., Chen, Y.W., Cai, M.F., and Li, Y.R. (2004) A review on pyrrhotite oxidation. Journal of Geochemical Exploration, 84, 65-76.

Cook, N.J. and Chryssoulis, S.L. (1990) Concentrations of invisible gold in the common sulfides. Canadian Mineralogist, 28, 1-16.

Fleet, M.E. and Mumin, A.H. (1997) Gold-bearing arsenian pyrite and marcasite and arsenopyrite from Carlin Trend gold deposits and laboratory synthesis. American Mineralogist, 82, 182-193.

Palenik, C.S., Utsunomiya, S., Reich, M., Kesler, S.E., Wang, L.M., and Ewing, R.C. (2004) "Invisible" gold revealed: Direct imaging of gold nanoparticles in a Carlin-type deposit. American Mineralogist, 89, 1359-1366.

Reich, M., Kesler, S.E., Utsunomiya, S., Palenik, C.S., Chryssoulis, S.L., and Ewing, R.C. (2005) Solubility of gold in arsenian pyrite. Geochimica et Cosmochimica Acta, 69, 2781-2796.

Rimstidt, J.D., and Vaughan, D.J. (2003) Pyrite oxidation: A state-of-the-art assessment of the reaction mechanism. Geochimica et Cosmochimica Acta, 67, 873-880.

Rosso, K.M., and Becker, U. (2003) Proximity effects on semiconducting mineral surfaces II: Distance dependence of indirect interactions. Geochimica et Cosmochimica Acta, 67, 941-953.

Rosso, K.M. (2001) Structure and Reactivity of Semiconducting Mineral Surfaces: Convergence of Molecular Modeling and Experiment. In: Reviews in Mineralogy and Geochemistry 42 (Editors: R.T. Cygan and J.D. Kubicki), Mineralogical Society of America, Washington, DC, pp. 1999-262.

Rosso, K.M., Becker, U., and Hochella, M.F. (1999) Atomically resolved electronic structure of pyrite {100} surfaces: An experimental and theoretical investigation with implications for reactivity. American Mineralogist, 84, 1535-1548.

Vaughan, D.J., Becker, U., and Wright, K. (1997) Sulphide mineral surfaces: theory and experiment. International Journal of Mineral Processing, 51, 1-14.

Publications and Abstracts resulting from this Dissertation

Publications

Renock, D., Gallegos, T., Utsunomiya, S., Hayes, K.F., Ewing, R.C., and Becker, U. (2009) Chemical and structural characterization of As immobilization by nanoparticles of mackinawite (FeS_m). Chemical Geology, 268, 116-125. **Chapter 2**

Renock D. and Becker U. (2010) A first principles study of the oxidation energetics and kinetics of realgar. Geochimica et Cosmochimica Acta (in press) **Chapter 3**

Renock D. and Becker U. (2010) First principles investigation of coupled substitution in galena. Economic Geology (in preparation) **Chapter 4**

Conferences

Renock D., and Becker U. (2010) First principles investigation of coupled substitution in galena. Abstracts of the 20th Annual Goldschmidt Conference, Knoxville, Tennessee, A3408.

Renock D., Utsunomiya S., Gallegos T.J., Hayes K.F., Ewing R.C., and Becker U. (2007) Arsenic Uptake and Release on Sulfide Nanoparticles. Geochimica et Cosmochimica Acta, 71(15), Abstracts of the 17th Annual V.M. Goldschmidt Conference, Cologne, Germany, A833.

Renock D., Utsunomiya S., Gallegos T.J., Hayes K.F., Ewing R.C., and Becker U. (2007) Arsenic Uptake and Release on Sulfide Nanoparticles. 9th Annual European Mineralogical Society School: Nanoscopic Approaches in Earth and Planetary Sciences, Munich, Germany.

Renock D., Breitbach T., Utsunomiya S., Ewing R.C., and Becker U. (2007) Gold Deposition onto Pyrite and Arsenopyrite. 4th Annual Michigan Geophysical Union, Ann Arbor, MI.

Renock D., Becker U., Utsunomiya S., and Ewing R.C. (2006) STEM and Electrochemical SFM Characterization of As-containing Nanoscale Phases on Iron Sulfides. Abstracts of the 231st American Chemical Society National Meeting, Atlanta, Georgia, 60-GEOC.

Renock D., Utsunomiya S., Becker U., Gallegos T.J., Hayes K.F., and Ewing R.C. (2006) Arsenic Uptake on Synthetic Mackinawite. Slovenia and U.S. Workshop on Environmental Science and Engineering, Ljubljana, Slovenia.

Renock D., Utsunomiya S., Becker U., Gallegos T.J., Hayes K.F., and Ewing R.C. (2006) Arsenic Uptake on Synthetic Mackinawite. 3rd Annual Michigan Geophysical Union, Ann Arbor, MI.

Publications and abstracts resulting from side-projects (not included in this thesis)

Publications

Pointeau V., Deditius A.P., Miserque F., Renock D., Becker U., Zhang J., Clavier N., Dacheux N., Poinssot C., and Ewing R.C. (2009) Synthesis and characterization of coffinite. Journal of Nuclear Materials, 393, 449-458.

Deditius A. P., Utsunomiya S., Renock D., Ewing R. C., Ramana C. V., Becker U., and Kesler S. E. (2008) A proposed new type of arsenian pyrite: composition, nanostructure and geological significance. Geochimica et Cosmochimica Acta, 72, 2919-2933.

Conference Abstracts

Renock D., Deditius A., Reich M., Kesler S.E., Ewing R.C., and Becker U. (2008) Gold deposition onto arsenian pyrite. Geochimica et Cosmochimica Acta, 72(12), Abstracts of the 18th Annual Goldschmidt Conference, Vancouver, Canada, A788.

Chapter 2

Chemical and structural characterization of As immobilization by nanoparticles of mackinawite (FeS_m)

Abstract

The mobility and availability of arsenite, As(III), in anoxic environments is largely controlled by adsorption onto iron sulfides and/or precipitation of arsenic in solid phases. The interaction of As(III) with synthetic mackinawite (FeS_m) in pH 5 and 9 suspensions was investigated using high-angle annular dark field (HAADF) scanning transmission electron microscopy (STEM), STEM elemental mapping, high resolution TEM, and X-ray photoelectron spectroscopy (XPS). At pH 5, arsenic sulfide phases precipitate among the FeS_m particles as discrete particles that are an amorphous hydrous phase of arsenic sulfide. The oxidation state of As in the surface layers of the arsenic sulfide precipitates is 'realgar-like' based on XPS results showing that >75% of the As 3d peak area is due to As with oxidation states between 0 and 2+. Discrete, arsenic sulfide precipitates are absent at pH 9, but elemental mapping in STEM-EDX mode shows that arsenic is uniformly distributed on the FeS_m, suggesting that uptake is caused by the sorption of

As(III) oxyanions and/or the precipitation of highly dispersed arsenic sulfides on FeS_m. XPS also revealed that the FeS_m that equilibrated without As(III) has a more oxidized surface composition than the sample at pH 9, as indicated by the higher concentration of O (~three times greater than that at pH 9) and the larger fraction of Fe(III) species making up the total Fe (2p3/2) peak. These findings provide a better understanding of redox processes and phase transitions upon As(III) adsorption on iron sulfide substrates.

Introduction

Arsenic, a toxic metalloid, can be introduced into the environment by anthropogenic sources, as in the case of acid mine drainage, or by natural sources, such as from volcanic activity. Most As enters the hydrosphere through natural weathering of arsenopyrite or arsenian pyrite. The World Health Organization has described the problem of arsenic contamination of drinking water and irrigation supplies as "the greatest mass poisoning in human history" (Vaughan, 2006). The most widely contaminated areas are in Bangladesh and West Bengal where over 40 million people are at risk of arsenicosis and other arsenic–related health problems (Smedley and Kinniburgh, 2002). The solubility of arsenic; and hence, its bioavailability and toxicity depend on its speciation, which is controlled by the Eh and pH of ground and surface waters (Cullen and Reimer, 1989). The two main arsenic oxidation states found in water are arsenite, As(III), and arsenate, As(V), with both being in the form of pH-dependent oxyanion species, H_3AsO_3 and H_3AsO_4, respectively. As(III) is more mobile and toxic than As(V) (Penrose, 1974). The concentration and transport of arsenic oxyanions in water is significantly affected by adsorption onto the surfaces of oxide, clay, and sulfide minerals.

The adsorption of dissolved As(III,V) to insulating oxide and clay minerals has been described extensively by means of surface complexation theory (Pierce and Moore, 1982; Waychunas *et al.*, 1996; Fendorf *et al.*, 1997; Swedlund and Webster, 1999; Nickson *et al.*, 2000; Li *et al.*, 2007). However, there are relatively few studies detailing arsenic uptake mechanisms by sulfides, despite their clear importance in the cycling of arsenic in anoxic environments (Farquhar *et al.*, 2002; Bostick and Fendorf, 2003; Wolthers *et al.*, 2005; Gallegos *et al.*, 2007). This is, in part, due to the lack of understanding of how the semiconducting and magnetic properties, inherent to this class of minerals, affect chemical bonding on surfaces. For metal sulfide semiconductors, the surface presents a significant perturbation of the electronic structure of the bulk in the near-surface layers. Surface electronic states that result from surface reconstruction, defects, vacancies, adsorbates, and discrete surface phases dominate the initial stages of surface chemical behavior. For example, step edges on galena (PbS) and monoclinic pyrrhotite (Fe_7S_8) have been shown to be highly reactive redox sites, as compared with flat terraces (Becker and Rosso, 2001; Becker *et al.*, 1997). Oxidation and disproportionation reactions on sulfides can result in surface oxidation products, such as polysulfides and elemental sulfur that can participate in surface reactions (Schaufuss *et al.*, 1998). Unique behavior, such as the coupling of spatially separated redox processes by electronic perturbations in the near surface layers, can influence the energetics and rates of surface reactions (Becker *et al.*, 2001).

This study investigates the uptake of As(III) on tetragonal iron (II) monosulfide, mackinawite, which has a composition of FeS_{1-x} (designated FeS_m in this study) with $0 < x < 0.07$ (Vaughan and Lennie, 1991). FeS_m is significant because it is the first iron

sulfide to precipitate in most anoxic environments. The black color commonly associated with anoxic mud is generally attributed to the presence of black FeS_m precipitate formed by sulfate-reducing bacteria. Other relevant environments include deep sea-floor hydrothermal systems. Recently, there has been an interest in using mackinawite in permeable reactive barriers (PRBs) in order to remediate arsenic-contaminated groundwater (Henderson and Demond, 2007).

At low temperatures, FeS_m precipitates first as nanoparticles of an amorphous phase (*i.e.,* finely-dispersed precipitates or coatings on other minerals), which transforms over time into crystalline FeS_m, as described by Wolthers *et al.*, (2003), and eventually to sedimentary iron sulfide phases, such as greigite (Fe_3S_4), pyrrhotite (Fe_7S_8), and eventually marcasite (orthorhombic FeS_2) and pyrite (isometric FeS_2). Pyrite does not tend to spontaneously nucleate in solution under conditions typical of sedimentary environments. However, in these environments, the FeS_m surface can provide an initial nucleation site for pyrite growth (Schoonen and Barnes, 1991; Wilkin and Barnes, 1996; Rickard, 1997).

During iron-sulfide transformations, arsenic may be taken up via reaction mechanisms that depend on the solution conditions and the iron sulfide phase that is present. Bostick and Fendorf (2003) have suggested that the mechanism for arsenite uptake by pyrite and troilite (FeS) is by an arsenopyrite-like surface precipitate that forms at approximately neutral pH. Arsenite uptake by FeS_m is suggested to occur by different mechanisms. Farquhar *et al.* (2002) show As(III) uptake by sorption complexes and coprecipitation of poorly crystalline arsenic sulfides with FeS_m. Wolthers *et al.* (2005) study of disordered FeS_m showed arsenite uptake by the formation of outer-sphere

complexes, while Gallegos *et al.* (2007) suggest a mechanism that involves sorption of As oxyanions, as well as the formation of a 'realgar-like' precipitate, depending on the solution pH and concentration of dissolved arsenic.

This is the first investigation of the reaction of As(III) with synthetic FeS_m in pH 5 and pH 9 solutions using advanced electron microscopy techniques, including high-angle annular dark field (HAADF) scanning transmission electron microscopy (STEM), STEM elemental mapping, and high resolution TEM. HAADF-STEM is a relatively new technique based on image contrast being proportional to Z^2: heavier elements contribute to brighter contrast. This technique can be very effectively used to identify and characterize nanophases when elements of sufficiently different atomic mass are investigated (Utsunomiya and Ewing, 2003). In addition, changes in the oxidation state and speciation of the FeS_m surface after reacting with As(III) were investigated using X-ray photoelectron spectroscopy (XPS). This study is designed to provide insight into the composition, structure, and distribution of arsenic after reaction with FeS_m, as well as the changes in the surface composition of FeS_m that accompany these reactions.

Methods

Mackinawite synthesis

The procedure used to synthesize FeS_m is described in Gallegos *et al.* (2007). Briefly, synthesis was in a 5 % H_2/ 95% N_2 glovebox (Coy Inc.) with a Pd catalyst in order to limit FeS_m exposure to atmospheric O_2; however, samples were briefly exposed to air during transfer steps. De-oxygenated water used in all reaction solutions was prepared by bubbling deionized water (18 MΩ) obtained from a Millipore Milli-Q system with

99.99% N_2 gas for 2 hours. Ferrous and sulfide stock solutions were prepared using $FeCl_2 \cdot 4H_2O$ and $Na_2S \cdot 9H_2O$ (Sigma Aldrich), respectively.

Synthetic FeS_m was precipitated by mixing solutions of 0.34 M $FeCl_2 \cdot 4H_2O$ with 0.35 M $Na_2S \cdot 9H_2O$. The resulting black solid was aged in solution inside the anoxic chamber for four days prior to centrifugation, and finally rinsed to remove excess dissolved salt ions (Wang and Morse, 1996). The solid was stored as a paste within the anoxic chamber for up to 4 months. The paste was re-suspended in de-oxygenated, deionized water in order to produce a FeS_m stock suspension for all experiments. The external specific surface area (SSA_{ext}) for FeS_m prepared by this method is expected to range from 276 to 424 ± 130 m^2/g (Jeong *et al.*, 2008).

Sample preparation

All sample preparation was completed inside the 5% H_2/ 95 % N_2 glovebox. Solids for TEM analysis were prepared by spiking pH 5 and pH 9 FeS_m suspensions (5 g FeS/L) with a 0.015 M $NaAsO_2$ stock solution to achieve total concentrations of 5×10^{-5} M As(III). In each case, 0.1 N HCl was added to maintain the desired pH. The samples were equilibrated for 72 hours on a rotating mixer. At the end of the reaction period, the final pH was recorded. Surface coverage for TEM samples were 1.0×10^{-5} and 3.5×10^{-6} mol As/g FeS at pH 5 and pH 9, respectively. Samples were prepared one day in advance of TEM analysis by diluting the solid suspensions with DI water (at pH 5 and 9) in order to achieve final solid concentrations of 0.5 g/L.

XPS samples were prepared three days prior to analysis by lowering the pH of two 5.0 g/L suspensions of FeS_m to pH 5 and 9 by adding 1 N HCl and equilibrating until the

pH stabilized in a 0.10 M NaCl solution. After the initial equilibration time, the two suspensions were further divided into two equal portions. One of the portions was spiked with a 0.15 or 0.015 M $NaAsO_2$ stock solution to achieve total concentrations of 2.5×10^{-4}M As(III) (pH 9) or 1.0×10^{-2} M As(III) (pH 5) which represent maximum loading conditions as a function of pH (Gallegos, 2007), while the second was left untreated as a control. HCl (0.1 N) was added, as necessary, to maintain the desired pH. At the end of the reaction period of 48 hours, the final pH was recorded, and samples were centrifuged at 10,000 rpm for 20 minutes. The As loading for the XPS samples were 5.0×10^{-5} M As/g FeS at pH 9 and 2.0×10^{-3} M As/gFeS (pH 5). The solutions were decanted leaving behind pastes that were vacuum freeze dried for 48-72 hours.

Transmission electron microscopy (TEM)

TEM samples were prepared one day in advance of analysis. All sample preparation was completed inside the 5% H_2/N_2 glovebox. Carbon-coated copper mesh grids (~3cm dia.) were placed atop a paper filter to wick off excess moisture. A 6 μL aliquot of each solution containing 0.5g/L (FeS_m) was placed on a carbon-coated copper grid and rinsed with 4 μL of deoxygenated, deionized water. The samples were dried inside the glovebox for 24 hours before transferring them into the TEM analysis chamber. Sample grids were rapidly transferred from N_2-filled bags to the high-vacuum TEM chamber to minimize sample exposure to oxygen.

HAADF-STEM was utilized to evaluate the distribution of arsenic phases in the samples. High-resolution TEM (HRTEM), AEM (analytical electron microscopy), and HAADF-STEM were conducted using a JEOL-JEM 2010F field emission gun

microscope with an EDAX energy-dispersive X-ray spectrometer. The microscope was operated at 200 keV. Nanoscale elemental mapping of arsenic, iron, and sulfur was completed with HAADF-STEM coupled with Emispec ES Vision version 4.0 for samples reacted at pH 5 and EDAX Genesis for pH 9 samples (instrument software was converted during the timeframe of the study). Image processing, including the generation of diffraction patterns from the fast Fourier transformation (FFT), was completed using Gatan Digital Micrograph 3.6.4.

X-ray photoelectron spectroscopy (XPS)

X-ray photoelectron spectra were obtained with a Kratos Axis Ultra XPS using a monochromatized Al Kα (1486 eV) X-ray source. The base pressure in the analysis chamber was on the order of 10^{-9} Torr. FeS_m samples were prepared by mounting the powder on double-sided Cu tape. Air exposure was minimized during transfer to the XPS chamber. The charge-neutralizer filament was used for all samples to control charging of particles that were in poor contact with the stage. Peak shifts due to surface charging were taken into account by normalizing energies based on the adventitious carbon peak at 284.5 eV. Survey and narrow-scan XPS spectra were obtained using pass energies of 160 and 20 eV, respectively. Survey scans were used to determine the average composition of the surface. The semiquantitative composition of the near-surface layers was calculated from the peak areas of the Fe(2p), S(2p), O(1s), and As(3d) peaks and normalized by their respective sensitivity factor (Wagner *et al.*, 1981). Narrow-scan spectra were obtained in order to determine oxidation states of Fe, S, O, and As surface species.

Raw spectra were fitted using a least-squares procedure with peaks of convoluted Gaussian (80%) and Lorentzian (20%) peak shape after subtraction of a Shirley baseline. All spectra were fitted with the least number of components that would give reasonable agreement with the measured spectra. Binding energies for the component peaks, e.g., for the different oxidation states and bonding environments of each element (*i.e.,* Fe, S, O, As) were identified by comparison with literature values. The full-width at half-maximum (FWHM) of the fitted peaks were also constrained within ranges reported in the literature.

Fe($2p_{3/2}$) spectra were fit with peaks corresponding to four primary species that have been widely characterized in the literature for iron sulfides: Fe(II)-S, Fe(II)-O, Fe(III)-S, and Fe(III)-O. The ferrous sulfide, Fe(II)-S, of bulk FeS_m is modeled by a single peak at 707.3±0.1 eV. A multiplet structure was not used in the fit due to the low spin configuration of Fe in FeS_m as shown by Vaughan and Ridout (1971) and Mullet *et al.* (2002). Ferrous oxide, Fe(II)-O, was modeled using peaks in the range of 708.5-709.5 eV. Both ferric iron species, Fe(III)-S and Fe(III)-O, were modeled using a quartet of peaks that is due to multiplet splitting predicted by crystal field theory for high-spin Fe(III) (Gupta and Sen, 1974). Fe(III)-S peaks were fit to peak positions centered at 708.9±0.1 eV, 709.9±0.1 eV, 710.8±0.1 eV, and 711.0±0.1 eV with peak ratios of 1, 0.66, 0.35, and 0.1, respectively. Fe(III)-O peaks were also fit by a quartet of peaks, but at slightly higher binding energies than Fe(III)-S. Fe(III)-O peak positions were centered at 710.9±0.1 eV, 712.1±0.1 eV, 713.1±0.1 eV, and 714.1±0.1 eV, and with the same peak area ratios as Fe(III)-S.

The S(2p) spectra were modeled as doublets ($2p_{1/2}$ and $2p_{3/2}$) separated by a spin-orbit splitting of 1.2 eV with the higher binding energy $2p_{1/2}$ peak constrained to be half the area of the $2p_{3/2}$ peak. The experimental S(2p) spectra were modeled by S(2p) XPS peaks obtained from bulk structures. The S($2p_{3/2}$) peak positions were as follows: sulfate (S^{6+}) at 168.2±0.3 eV, elemental sulfur (S_8^0) at 165.3±0.2 eV, polysulfide (S_n^{2-}) at 163.4± 0.1 eV, disulfide (S_2^{2-}) at 162.3± 0.2 eV, sulfide (S^{2-}) at 161.2± 0.2 eV), and realgar-like sulfide (S^{2-}) at 163.1 eV.

The As(3d) spectra was modeled by five doublet peaks ($3d_{3/2}$ and $3d_{5/2}$) separated by a spin-orbit splitting of 0.70 eV. The As($3d_{3/2}$) peak was constrained to be 2/3 the area of the As($3d_{5/2}$) peak. The As($3d_{5/2}$) peak positions were as follows: As^{5+} at 46.0 eV, As^{3+} at 44.4 eV, As^{2+} at 42.8 eV, elemental As^0 at 42.0 eV, and As^{-1} at 40.9 eV.

The O(1s) spectra were modeled using three principal components: lattice oxygen (O^{2-}) at 529.9±0.3 eV, hydroxide $(OH)^-$ at 531.3±0.3, and adsorbed H_2O at 532.7±0.2 eV.

A Monte-Carlo method (CasaXPS software) was used to estimate the standard deviation of the component peak areas used in the fitting procedure. The program applies artificial noise to each spectrum and calculated an error matrix to give the variance of each fitting parameter based on the fitting constraints used.

Note, the component peaks used to model the experimental peaks were used as proxies for certain bonding environments and may not accurately represent specific surface species. XPS peaks are typically interpreted in terms of known bulk structures for which standards can be run. The diversity of intermediate oxidation products that occur on sulfide surfaces is difficult to resolve, and, because of the number of resulting peaks, either hard to distinguish from the background or the peaks of surface species may

contribute to the peaks that were fit (Becker and Hochella, 1996). In this context, fitting the Fe($2p_{3/2}$), S(2p), As(3d), and O(1s) with component peaks is a useful tool to evaluate the general character of the oxidation state of species on the surface, but should not be interpreted as taking into account all possible surface species that might be present.

Results and Discussion

Previous studies (Gallegos, 2007; Gallegos *et al.*, 2007) have indicated that the synthetic FeS_m (5g/L suspension) was effective in lowering the aqueous As(III) concentration at pH values of 5 and 9 from the initial As(III) concentrations used in this study. Solution analysis of samples characterized by TEM show that 100% (at pH 5) and 32% (at pH 9) of the initial 5×10^{-5} M As(III) is removed from solution by the 5g/L FeS_m suspension. These loadings indicate that As uptake at pH 9 is substantially less than at pH 5.

TEM analysis

In general, FeS_m forms micrometer-sized aggregates composed of needle-like nanoparticles that are elongated perpendicular to the c-axis. The individual needles are approximately 5 nm thick (the direction parallel to the c-axis) and up to 0.2 μm long (perpendicular to c-axis). The HRTEM image in Figure 3.1 shows a synthetic FeS_m particle oriented along a zone axis. The inset in Figure 3.1 shows the fast Fourier transform image of the area outlined in the HRTEM image. The diffraction maxima of the FFT transformation were indexed as mackinawite, FeS_m[010]. The d_{001} of FeS_m was determined to be 5.14 Å from the indexed diffraction pattern, which is in close agreement with *d*-spacing of (001) planes

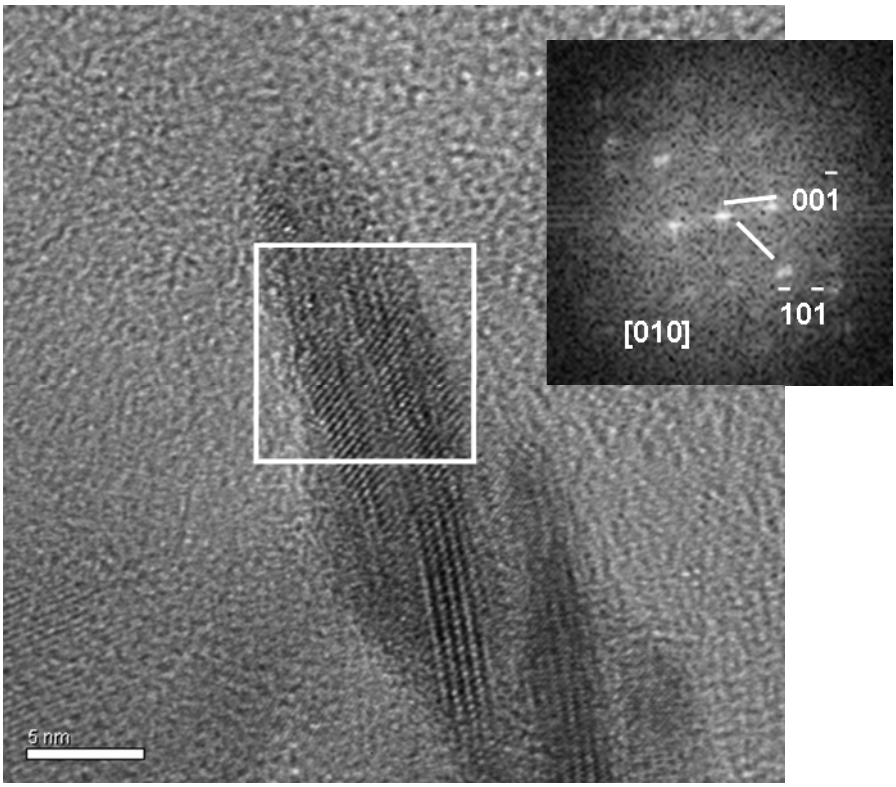

Figure 3.1. HRTEM image of representative FeS_m particles reacted with 5×10^{-5} M As(III) at pH 5. The FeS_m particle is oriented along [010]. The inset shows the FFT image of the area boxed in the image. The diffraction maxima of the FFT transformation were indexed to be those of mackinawite, FeS_m. The d_{001} of mackinawite was determined to be 5.14 Å.

of 5.19 Å for a synthetically precipitated FeS_m (Ohfuji *et al.*, 2006; Jeong *et al.,* 2008). No obvious differences in the morphology of FeS_m particles before and after the reaction with As(III) were observed, nor were there any differences between FeS_m particles reacted in either pH 5 or 9 solutions (not shown).

HAADF-STEM: FeS / As(III) at pH 5

Figure 3.2 is an HAADF-STEM image of FeS_m reacted in a pH 5 solution with an initial As(III) concentration of 5×10^{-5} M. Elongated particles up to several μm in length are shown in the STEM image. These particles are brighter than the ~0.1-0.2 μm FeS_m particles identified in the bottom left of the micrograph suggesting a phase with a higher average atomic mass than FeS_m. The bottom right inset of Figure 3.2 shows a higher magnification HRTEM image of one of the brighter, elongated particles in the HAADF-STEM image. The particle appears to be semi-amorphous and/or hydrous as evidenced by a general lack of lattice fringes in the inset and its susceptibility to sublimation induced by the high-energy electron beam. Some minor domains showing lattice fringes are evident, but it is unclear whether they are regions of crystallinity within the larger particle or FeS_m particles overlapping the larger particle. EDS point analysis (not shown) of several of the bright particles revealed a chemical composition consisting of 90 % As and 10 % S (in atomic %), though a large error is expected in these values due to the rapid destruction of the particles when exposed to the electron beam. The relative amount of iron present in the bright particles is negligible, suggesting that these particles may be an isolated arsenic sulfide phase or a mixture of phases with a semi-amorphous structure and range of compositions between orpiment (As_2S_3) and duranusite (As_4S). Diffraction

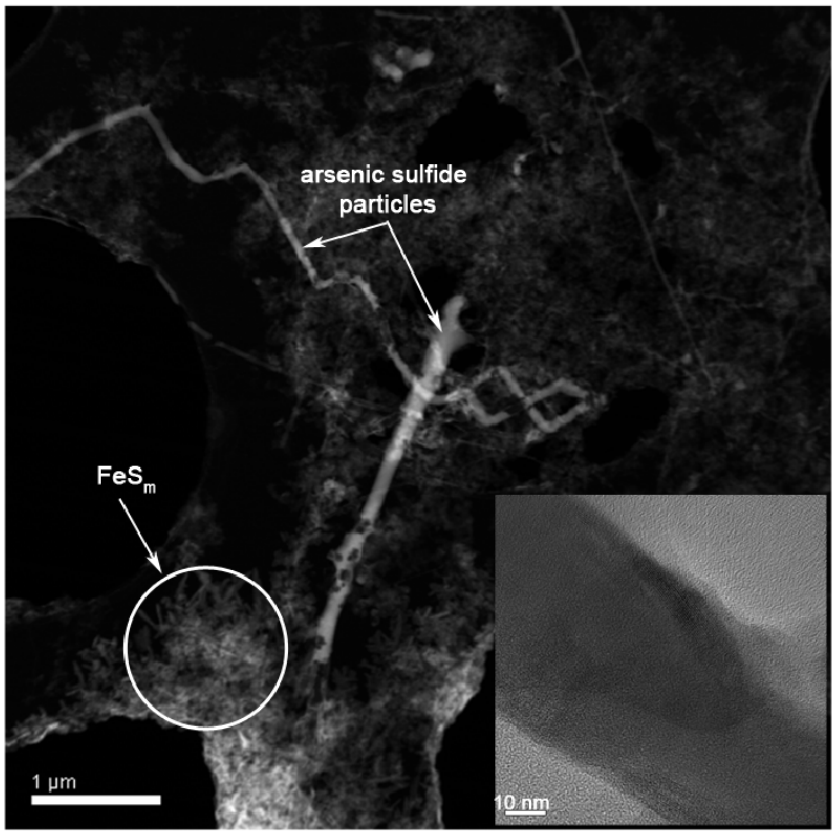

Figure 3.2. HAADF-STEM image of FeS_m reacted with 5×10^{-5} M As(III) at pH 5. Elongated arsenic sulfide particles up to several µm in length are shown in the image (particles are brighter in the image due to their higher average atomic mass relative to the FeS_m particles in the background). Inset in lower right corner is a HRTEM image of a section of one of the elongated particles in the HAADF-STEM image. The lack of lattice fringes indicates that the arsenic sulfide precipitates are primarily amorphous.

patterns of the As-S-rich particles could not be acquired because of the lack of crystallinity (Figure 3.2 inset).

HAADF-STEM with EDX mapping confirmed the distribution of isolated arsenic sulfide-rich phases and their structural relation to the FeS_m nanocrystals. Figure 3.3 shows the HAADF-STEM image with a box indicating the region of EDS elemental maps. EDS maps specific to As, Fe, and S are shown to the right of the image and confirm the high concentration of As in the bright particles as compared with Fe. Elemental analysis shows that the As (coincidental with high concentrations of S) is isolated in discrete particles rather than homogeneously distributed throughout the sample or as a coating on the FeS_m particles. These observations support the findings from the previous X-ray absorption spectroscopy (XAS) and X-ray diffraction (XRD) analyses indicating the presence of discrete arsenic sulfide solids precipitating in solution at pH 5 (Gallegos *et al.*, 2007).

HAADF-STEM: FeS-As(III) at pH 9

Figure 3.4 shows a HAADF-STEM image of FeS_m reacted with 5×10^{-5} M As(III) at pH 9. The suspension of FeS_m particles in the solution at pH 9 was well dispersed and more so than the pH 5 suspension, and therefore only small, isolated clusters of FeS_m could be affixed onto the TEM grid. Discrete As-S-rich particles, which were ubiquitous at pH 5, were absent at pH 9. The HAADF-STEM image with As, Fe, and S elemental maps reveals a more homogeneous distribution of As (signal above the level of noise) than the pH 5 sample (Figure 3.4). The As signal is uniformly associated with areas containing Fe and S. The differences in the distribution of As in the pH 5 and 9 samples

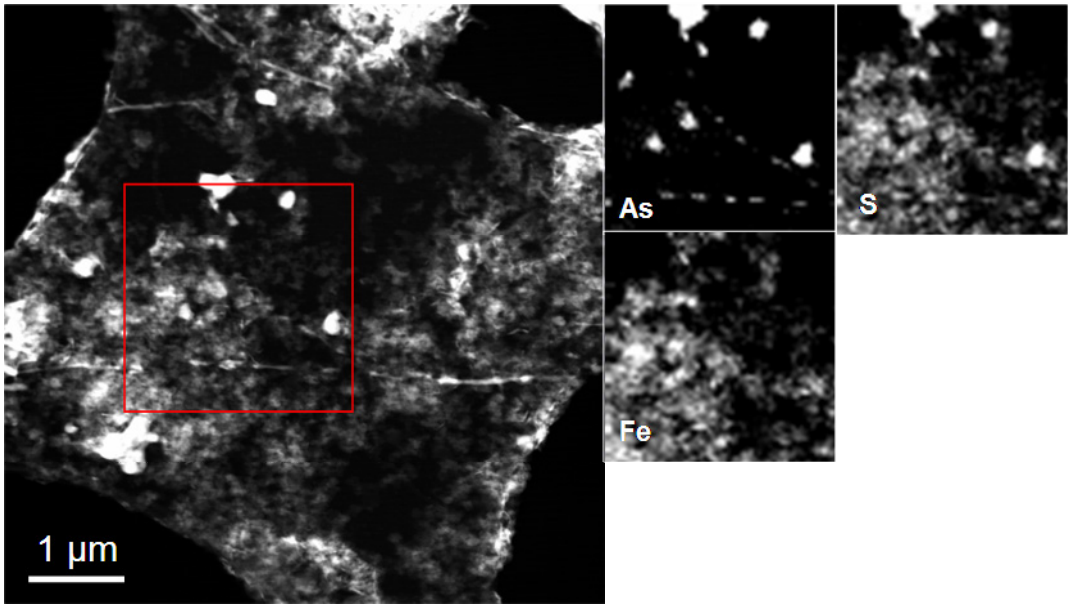

Figure 3.3. HAADF-STEM with EDX mapping of FeS_m equilibrated with 5×10^{-5} M As(III) at pH 5. The box in the image shows the region of EDS elemental mapping. EDS maps specific to As, S, and Fe are shown to the right of the image and confirm the presence of discrete arsenic sulfide phases. EDS maps collected using Emispec ES Vision ver. 4.0.

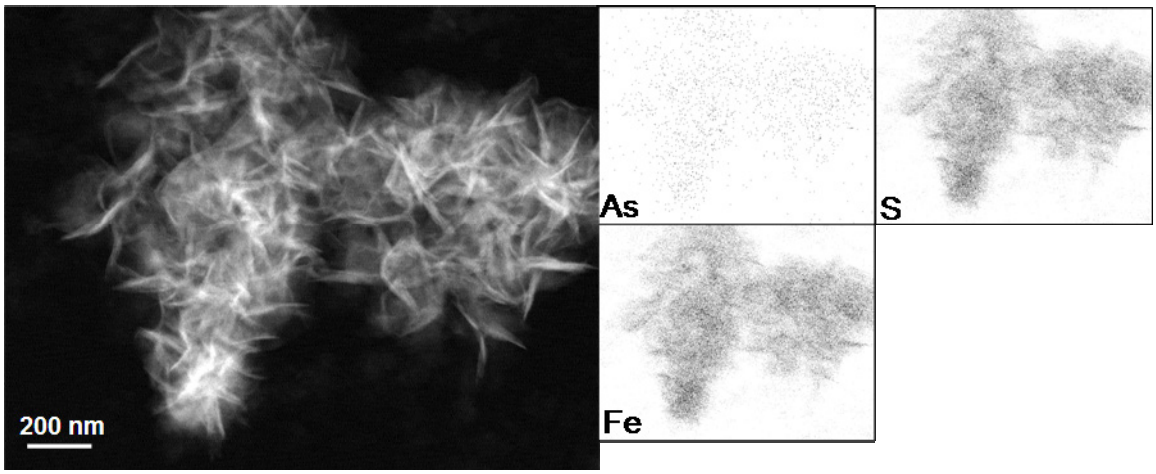

Figure 3.4. HAADF-STEM with EDX mapping of FeS_m equilibrated with 5×10^{-5} M As(III) at pH 9. EDS maps specific to As, S, and Fe are shown to the right of the image and show a homogeneous distribution of As among the FeS_m aggregates. EDS maps collected using EDAX genesis software.

may indicate a finer dispersion of arsenic sulfides on the surface of FeS_m at pH 9 or the sorption of As(III) oxyanions that are characteristic of As-uptake under these solution conditions (Gallegos *et al.*, 2007).

X-ray photoelectron spectroscopy (XPS)

XPS is sensitive to the composition and chemical oxidation state of the uppermost ~10 nm of the sample surface, depending on the instrument, the angle between sample surface and detector, and the kinetic energy of the electrons of a specific peak. Higher As loadings were used for samples analyzed by XPS analysis so that reasonable signal-to-noise ratios could be obtained. It is important to note that the mechanism of As-uptake can change depending on the initial As concentration; however, Gallegos *et al.* (2008) have shown that, at similar loadings and under similar solution conditions, As(III) removal may occur by the formation of arsenic sulfide precipitates at pH 5 and 9. The XPS survey scan of the synthetic FeS_m indicates the presence of Fe, S, C, O, Na, and Cl on the surface. Adventitious carbon is found in all samples. Residual Na and Cl are from the incomplete removal of the background electrolytes prior to drying. Oxygen is present on all samples despite efforts to limit oxygen exposure during synthesis and sample preparation. This is not surprising given that reactive iron sulfide phases have a tendency to partially oxidize within a fraction of a second (e.g., Becker *et al.*, 1997).

Table 3.1 shows a comparison of surface compositions (in atomic %) for FeS_m treated in pH 5 and pH 9 solutions without As(III), and after reaction with As(III). In general, the oxygen concentration fluctuates the most among the four analyzed samples due to the high reactivity of FeS_m to oxygen. FeS_m equilibrated in the pH 5 solution (no As)

Table 3.1. Total atomic % on FeS_m surface using peak areas from Fe(2p), S(2p), O(1s), and As(3d). Peaks areas are normalized vs. sensitivity factors taken from Wagner *et al.*, 1981.

Element	**pH 5 (no As added)**	**pH 5 (1×10^{-2}M As(III))**	**pH 9 (no As added)**	**pH 9 (2.5×10^{-4}M As(III))**
Fe	23%	23%	32%	21%
S	30%	46%	53%	15%
O	47%	17%	15%	64%
As	0%	14%	0%	Below detection limits
S:Fe atomic ratio	1.3	2.0	1.7	0.7

shows an oxygen surface coverage of 47% as compared with 15% for the sample at pH 9 (no As). The higher oxygen concentration at pH 5 may be due to the oxidation of dissolved Fe(II) species sorbed to the surface of FeS_m. The release of dissolved Fe(II) from the non-oxidative dissolution has been described by Rickard and Luther, (2007) showing that Fe(II) solubility is relatively low at neutral to high pH but dramatically increases below pH 6. A fraction of the residual dissolved Fe(II) that sorbs onto the FeS_m surface is susceptible to oxidation with brief exposure to air, as suggested by Herbert *et al.* (1998) and Mullet *et al.* (2002). At pH 9, since the amount of dissolved Fe(II) is substantially less than at pH 5, surface oxidation products are correspondingly less.

The FeS_m samples that were equilibrated with As(III) at pH 5 and pH 9 have oxygen concentrations of 17% (as compared with 47% without As) and 64% (as compared with 15% without As), respectively. The >2.8× difference in oxygen concentrations between pH 5 and 9 samples treated with and without As suggest that the uptake of As(III) by FeS_m proceeds by a different reaction mechanisms at these two pH values.

Table 3.1 also shows the S:Fe atomic ratios of the surface layers. Samples that were not reacted with As show S:Fe ratios of 1.3 (pH 5) and 1.7 (pH 9) and indicate an S-enriched surface. These values are slightly lower than the S:Fe ratios of 2.1 and 1.9 reported by Mullet *et al.* (2002) and Herbert *et al.* (1998), respectively, for synthetic FeS_m. The variability in the S:Fe ratio may be due to the different FeS_m synthesis conditions employed in each of the studies and/or the fact that the samples in this study were equilibrated in pH 5 and pH 9 solutions prior to XPS analysis, while the samples in the previous studies were not. In addition, similar S:Fe ratios were reported for vacuum fractured Fe_7S_8, including values of 2.1 (Pratt *et al.*, 1994) and 1.7 (McIntyre *et al.*,

1996). Herbert *et al.* (1998) suggested that disulfide and polysulfide species could contribute to S:Fe ratios >1 for FeS_m, and Pratt *et al.* (1994) suggested that an iron loss mechanism, which leaves polysulfides on the surface, is responsible for S:Fe ratios >1.1 for Fe_7S_8.

The sample equilibrated with As(III) at pH 5 has a S:Fe ratio of 2.0 as compared with 1.3 without As. The pH 5 result may be explained by the non-oxidative and/or oxidative dissolution of FeS_m and subsequent precipitation of amorphous arsenic sulfide phases, as is shown in the HRTEM micrographs for these samples (Figs. 2.2-2.3).

As species are only present in XPS spectra for FeS_m equilibrated with As(III) at pH 5, presumably due to the higher uptake capacity of As(III) at this pH. The surface concentration of As for the pH 9 sample was determined to be below the detection limits of the instrument.

Fe($2p_{3/2}$) components

The Fe($2p_{3/2}$) spectra for FeS_m at pH 5 and 9, before and after the sample was reacted with As(III), are presented in Figure 3.5 and 2.6. All spectra are decomposed into contributions from four major peaks. The first peak is centered at 707.3±0.1 eV and corresponds approximately to the binding energy of low-spin Fe(II)-S on the surface of FeS_m (Mullet *et al.*, 2002), and pyrite, FeS_2 (Mycroft et. al. 1990). The second, a multiplet of four peaks within the energy range, 709-712 eV, is attributed to high-spin Fe(III)-S for FeS_m (Mullet *et al.*, 2002; Herbert *et al.*, 1998;) and pyrrhotite, Fe_7S_8 (Pratt *et al.*, 1994). The third is Fe(III)-O, which is also modeled as a multiplet of four peaks, but shifted to slightly higher binding energies (711-714 eV) than Fe(III)-S

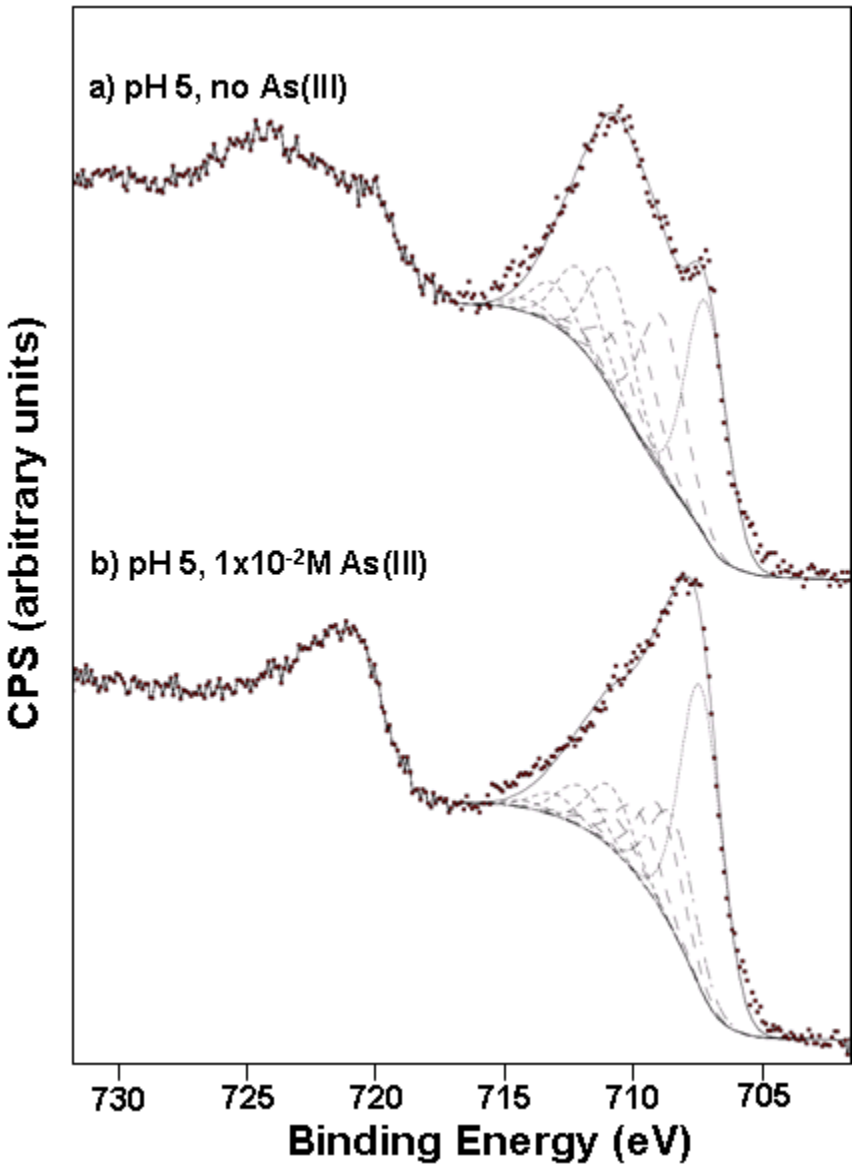

Figure 3.5. XPS spectra of Fe($2p_{3/2}$) peak for FeS_m equilibrated at pH 5. The experimental spectra were fitted with peaks for species: Fe(II)-S (-----), Fe(II)-O (— -), Fe(III)-S (— —), and Fe(III)-S (– – –). Circles are experimental data. Solid line represents the sum of the component peaks and background.

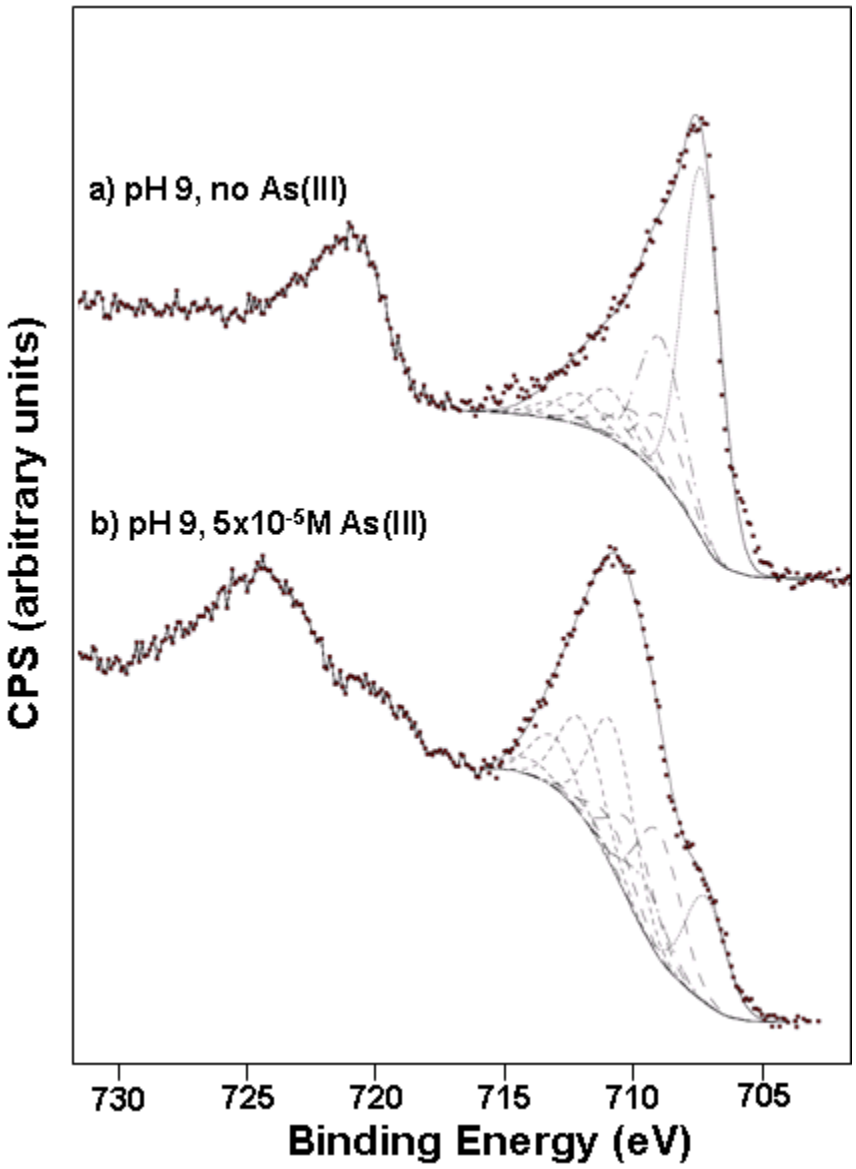

Figure 3.6. XPS spectra of Fe $2p_{3/2}$ peak for FeS_m equilibrated at pH 9. The experimental spectra were fitted with peaks for species: Fe(II)-S (-----), Fe(II)-O (— -), Fe(III)-S (— —), and Fe(III)-S (– – –). Circles are experimental data. Solid line represents the sum of the component peaks and background.

(Mullet *et al.*, 2002; Pratt *et al.*, 1994). The fourth peak falls within the energy range of 708.5-709.5 eV and corresponds to binding energies for Fe(II)-O species that have electronic states that are a result of partial coordination by oxygen (Mullet *et al.*, 2002; Thomas *et al.*, 1998). The integrated areas for each of the fitted peaks are listed in Table 3.2. In the case of multiplet peaks Fe(III)-O and Fe(III)-S, the total sum of the areas of the four peaks have been included for comparison.

The XPS results show the presence of both Fe(II)-S and Fe(III)-S species on the FeS_m surface (regardless of pH) consistent with the observations of Herbert *et al.* (1998) and Rickard (1969) that suggest the FeS_m surface acquires a composition similar to greigite, an iron-sulfide thiospinel Fe_3S_4 ($Fe_2^{(3+)}Fe^{(2+)}S_4^{(2-)}$). Transmission Mossbauer Analysis (TMA) results (Mullet *et al.*, 2002) also suggest the presence of both Fe(II) and Fe(III) in the FeS_m structure. The transformation of FeS_m to greigite has been directly observed using synchrotron techniques under dry conditions (Lennie *et al.*, 1997) and under hydrothermal conditions as an intermediate step in the formation of pyrite (Hunger and Benning, 2007). Because greigite is easily formed by oxidation of FeS_m, it is plausible that the surface of FeS_m may begin to acquire a 'greigite-like' composition at low temperature in an aqueous environment. In addition, it is well known that disproportionation reactions may result in a wide variety of surface species, including Fe(III)-S, even on pristine surfaces (Nesbitt and Muir, 1994; Herbert *et al.*, 1998; Nesbitt *et al.*, 1998).

A comparison of the spectra for the samples equilibrated in water before reaction with As(III) shows that at pH 5, the fraction of near-surface Fe(III)-S that contributes to the total Fe($2p_{3/2}$) signal is 2.2 times greater than the fraction of Fe(III)-S at pH 9.

Table 3.2. Peak areas for component peaks used in fitting the Fe($2p_{3/2}$) peak for FeS_m. Error values determined from Monte-Carlo routine.

Species	**Peak Areas (%)**			
	pH 5 (no As added)	**pH 5 1×10^{-2} M As(III)**	**pH 9 (no As added)**	**pH 9 2.5×10^{-4} M As(III)**
Fe(II)-S	27.0±2.2	38.4±2.3	46.1±2.2	13.6±1.4
Fe(II)-O	0.6±2.4	15.3±2.3	20.3±2.3	7.2±3.0
Fe(III)-S*	41.4±3.2	28.8±3.2	19.0±2.9	42.4±4.1
Fe(III)-O*	31.0±3.6	17.5±3.6	14.6±3.2	36.8±3.4

* includes all multiplet peak areas

The principal Fe component on the pH 9 sample is Fe(II)-S, characteristic of bulk FeS_m (~46%). The higher ratio of Fe(III)-S:Fe(II)-S for the pH 5 over the pH 9 sample is consistent with the observations of Yamaguchi and Wada (1972) who suggested that acidic pH values (as low as pH 3) promote the formation of greigite from FeS_m. Rickard and Luther (2007) have also noted that greigite is more commonly found in freshwater sediments than in marine sediments, and this may be due to freshwater systems typically being more acidic than marine systems. They go on to note that mechanistic studies of greigite formation from FeS_m and the oxidative dissolution of FeS_m are required to better understand the pH dependence of this reaction.

The pH 5 sample before As(III) addition was determined to have a Fe($2p_{3/2}$) peak composed of 31.0 % Fe(III)-O as compared with only 14.6% for the pH 9 sample. The larger contribution of Fe(III)-O to the total peak may be due, in part, to residual dissolved iron, Fe(II), that remains sorbed to FeS_m and/or reactive Fe(II) surface species that are subsequently oxidized during brief exposures to air. Since the solubility of FeS_m at pH 5 is higher than at pH 9 (Rickard and Luther, 2007), a larger contribution of Fe(III)-O to the Fe($2p_{3/2}$) peak is expected under acidic conditions, and this result is consistent with the higher oxygen concentration for the pH 5 sample versus the pH 9 (Table 3.1). The pH 9 sample before As(III) addition was determined to have a 20.3±2.3% contribution from Fe(II)-O that may be caused by hydroxylation and/or the formation of mixed-valence iron oxide phases, green rusts such as $Fe^{2+}Fe^{3+}(OH)_5$, expected under alkaline conditions.

The relative distribution of Fe($2p_{3/2}$) components changes after reaction with As(III) at both pH 5 and 9 as shown in Table 3.2. After As(III) reaction at pH 5, the peak areas for the Fe(II)-S and Fe(II)-O species increase from 27.0±2.2% to 38.4±2.3% and

0.6±2.4% to 15.3±2.3%, respectively, at the expense of the peak areas for Fe(III)-S and Fe(III)-O. These changes in Fe speciation are consistent with the decrease in total O concentration (Table 3.1) that accompanies As(III) equilibration at pH 5 and are most likely due to the surface reactions involving the reduction of As(III) and the subsequent precipitation of an amorphous arsenic sulfide phase (as shown from HAADF-STEM images in Figs. 2.2-2.3) with FeS_m. The appearance of a Fe(II)-O peak may be the result of the oxidation of Fe(II) by As(III) to form mixed-valence green rusts.

After equilibration with As(III) at pH 9, the peak areas for Fe(III)-S and Fe(III)-O species increase from 19.0±2.9% to 42.4±4.1% and 14.6±3.2 to 38.6±3.4%, respectively, at the expense of the peak areas for Fe(II)-S and Fe(II)-O. This change in peak areas is consistent with the increase in total O content (Table 3.1) that accompanies As(III) equilibration at pH 9. A possible explanation for the increase in the concentration of Fe(III) species is that dissolved As(III) may be promoting the oxidation of FeS_m at pH 9. The oxidation of Fe(II) to Fe(III) in disordered FeS_m by As(V) was reported by Wolthers *et al.* (2007), and a similar oxidation reaction by As(III) may be responsible for the observations in this study. Recently, Gallegos *et al.* (2008) reported the thermodynamic favorability of As(III) reduction to AsS and oxidation of the FeS to a mixed valent iron hydroxide green rust. The presence of Fe(II)-O (7.2±3.0%) and Fe(III)-O (38.6±3.4%) may indicate the presence of mixed-valence green rust phases, as well as ferric oxy-hydroxides, which have been reported by Bostick and Fendorf (2003) to be a product of As(III) reacting with pyrite (FeS_2) and troilite (FeS_t) under basic conditions.

$S(2p_{3/2})$ and $S(2p_{1/2})$ components

The S(2p) spectrum for FeS_m equilibrated in solution at pH 5 is shown in Figure 3.7. The spectra for pH 5 (As(III)) and pH 9 samples (no As(III), As(III)) are not shown due to the minor differences in the component peak areas (modeled as doublets) between the four spectra as indicated in Table 3.3. The dominant peak in all S(2p) spectra is located at 161.2±0.2 eV and corresponds to the $S(2p_{3/2})$ peak for monosulfide (S^{2-}) in FeS_m as reported by Mullet *et al.* (2002). Pratt *et al.* (1994) also report an S^{2-} peak at 161.3 eV for pyrrhotite. The origin of the peaks at higher binding energies is less certain due to the large number of sulfur oxidation products on the surface and the overlap of their respective peaks. Peaks at 162.3±0.2 eV and 163.4±0.1 eV correspond to the approximate peak position for disulfide (S_2^{2-}) or surface species with an approximate oxidation state of -1 on pyrrhotite (Thomas *et al.*, 1998), and polysulfide (S_n^{2-}, corresponding to a slightly negative oxidation state) on FeS_m (Mullet *et al.*, 2002), respectively. For simplicity, the peak area for S_2^{2-} is included in the peak area for S_n^{2-} (*i.e.,* no distinction is made for species with different oxidation states between -0.1 and -1) for each experimental condition in Table 3.3. A fourth doublet ($S(2p_{3/2})$-$S(2p_{1/2})$) with an $S(2p_{3/2})$ peak at 165.3±0.2 eV is attributed to elemental S_8^0, and constitutes <10% of the area of each of the spectra. The spectrum of the sample at pH 5 (no As(III)) is the only one with a broad shoulder at the high binding energy side of the S(2p) peak (Figure 3.7). A doublet with an $S(2p_{3/2})$ peak at 168.3 eV is used to accommodate the area of this shoulder, and corresponds approximately to the peak position of sulfate (S^{6+}) on the pyrrhotite surface (Thomas *et al.*, 1998).

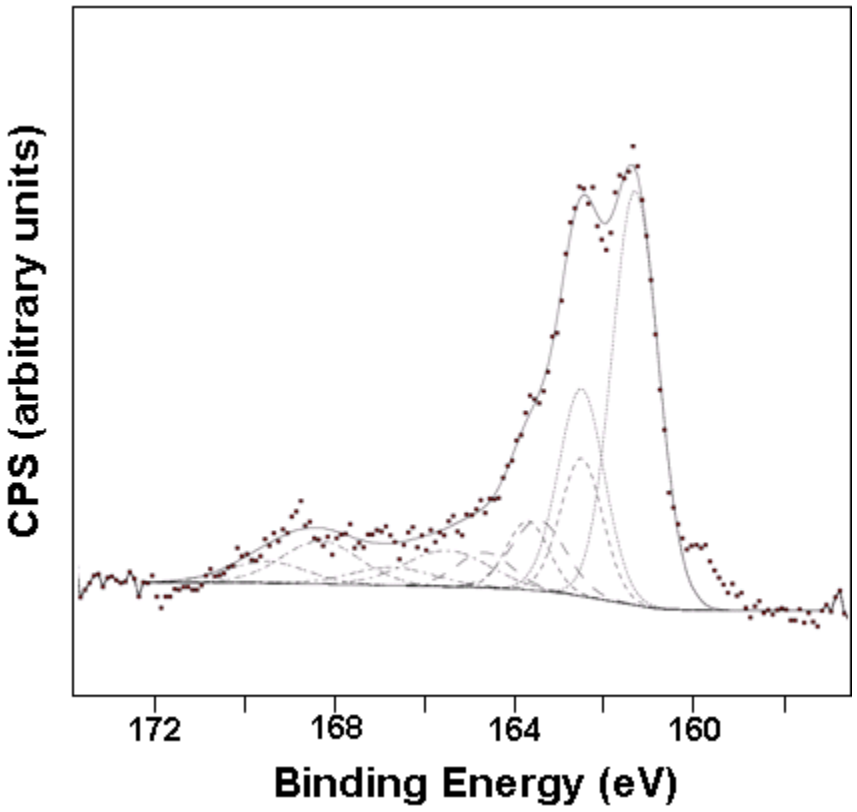

Figure 3.7. XPS spectra of S(2p) peak for FeS_m (pH 5, no As). The experimental spectra were fitted with peaks for species: S^{2-} (-----), S_2^{2-} (– – –), S_n^{2-} (— —), S_8^0 (— -), and S^{6+} (__ __). Circles are experimental data. Solid line represents the sum of the component peaks and background.

Table 3.3. Peak areas for component peaks used in fitting the S(2p) peak for FeS_m. Error values determined from Monte-Carlo routine.

Species	**Peak Areas (%)**			
	pH 5 (no As added)	**pH 5 1×10^{-2} M As(III)**	**pH 9 (no As added)**	**pH 9 2.5×10^{-4} M As(III)**
S^{2-}	54.4±2.6	63.0±1.2	59.7±2.2	54.6±3.7
S^{2-}(realgar)	N.A.	5.1±0.4	N.A.	N.A.
S_n^{2-}	27.5±4.8	29.4±2.0	35.1±3.1	35.9±5.7
S_8^0	8.6±2.1	2.6±1.1	5.0±2.1	9.5±3.9
S^{6+}	9.6±2.5	0	0	0

The major difference between the S(2p) spectra of the four samples is with regard to the elemental composition as shown in Table 3.1. The peak areas for S^{2-}, S_n^{2-}, and S_8^0 vary slightly over the four experimental conditions (Table 3.3). However, two slight changes in S speciation are apparent from the peak areas listed in Table 3.3 for the pH 5 sample. First, as previously mentioned, a ~10% contribution from a S^{6+} species is shown for the pH 5 sample (no As). The presence of sulfates may be due to reactive S species being oxidized during synthesis and processing as described by Mullet *et al.* (2002) and Herbert *et al.* (1998). This is consistent with the higher concentration of O (~47%) determined to be present on the FeS_m surface under these conditions. Second, the spectra for the pH 5 sample after reaction with As(III) is fit with one additional $S(2p_{3/2})$ peak at 163.1 eV that corresponds to the S^{2-} species in pure realgar, As_4S_4 (Pratt and Nesbitt, 2000). Inclusion of this doublet improves the fit parameters and is consistent with the formation of arsenic sulfide precipitates that have been identified in the TEM micrographs of these samples.

There are no significant changes in S speciation between the pH 9 samples before and after reaction with As(III), indicating that either S may be not participating in redox processes initiated by As(III) occurring on the surface or oxidized S species are being lost to solution.

As($3d_{5/2}$) and As($3d_{3/2}$) components

An As(3d) peak could not be resolved for the pH 9 sample presumably because the uptake at pH 9 is essentially 2 orders of magnitude lower than the uptake at pH 5 (5.0×10^{-5} M As/g FeS at pH 9 and 2.0×10^{-3} M As/gFeS at pH 5) and the concentration of As is below the detection limit of the instrument. However, an As(3d) peak is present in

XPS spectra for FeS_m equilibrated in a solution containing 1×10^{-2}M As(III) at pH 5, as shown in Figure 3.8. The binding energy of the As($3d_{5/2}$) peak spans a range from 39.0-48.0 eV, and the experimental peak is fit with five As components (As^{5+}, As^{3+}, As^{2+}, As^{0}, and As^{1-}), as shown in Table 3.4. The major contributor to the area of the experimental peak (~45%) is a peak at 42.8 eV, which corresponds to the As($3d_{5/2}$) peak position for As^{2+} in realgar (As_4S_4) (Bahl *et al.*, 1976). Approximately 34±1.8% of the experimental peak consists of a peak whose binding energy is consistent with elemental As^0 (Bahl *et al.*, 1976). The more oxidized As species (As^{3+} and As^{5+}) have a combined peak area that constitutes ~15% of the total As(3d) peak, which suggests that most of the detectable As exists in a reduced phase on the surface. The major reduced phases contain As with oxidation states ranging from 0 to +2 with a minor contribution from an As^{1-} species. The distribution of charge suggests the presence of As phases with multiple oxidation states, and/or semiconducting phases for which the charge is smeared out over multiple electronic states, as would be expected from the semi-amorphous arsenic sulfide-rich particles shown in Figure 3.2. The results further support previous X-ray absorption spectroscopy (XAS) results showing the presence of phases that closely match oxidation states consistent with realgar (As_4S_4) under similar conditions (Gallegos *et al.*, 2007).

O 1s components

The three major components used to fit the O spectra of the FeS_m samples (not shown) and their integrated areas are given in Table 3.5. The components used in the fit correspond to lattice oxygen (O^{2-}), hydroxyl groups $(OH)^-$, and adsorbed H_2O (Nesbitt *et al.*, 1995; Pratt *et al.*, 1994). The spectrum for the pH 5 sample (no As) shows

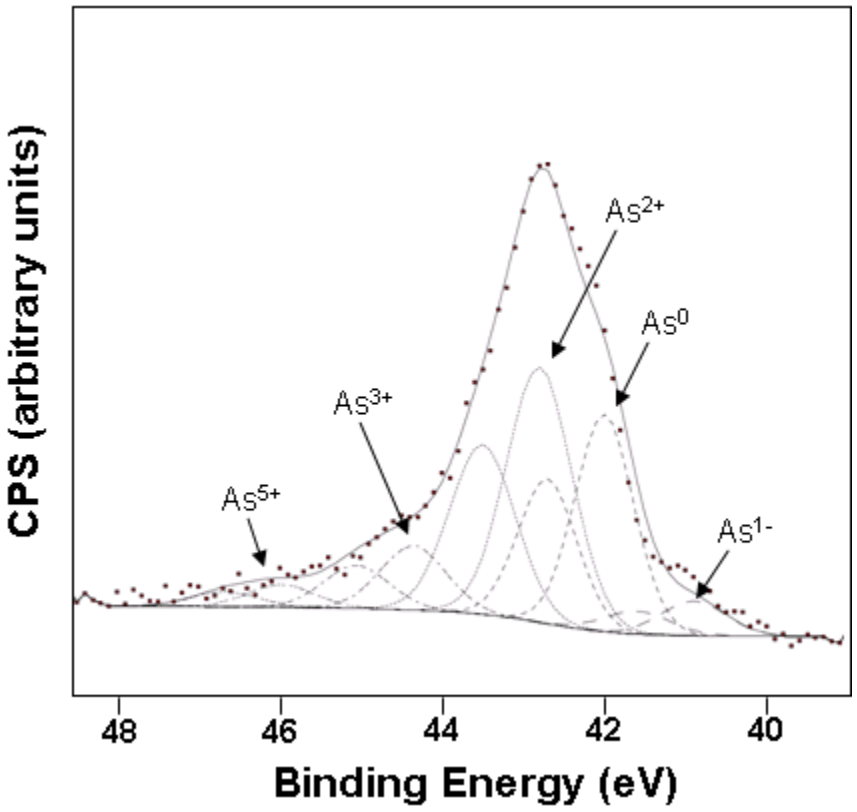

Figure 3.8. XPS spectra of As($3d_{5/2}$) and As($3d_{3/2}$) peaks for FeS_m equilibrated in solution containing 1×10^{-2} M As(III) at pH 5. As(3d) experimental peak fitted with peaks corresponding to As species shown in the figure (dashed lines). Circles are experimental data. Solid line represents the sum of the component peaks and background.

Table 3.4. Peak areas for component peaks used in fitting the As(3d) peak for FeSm. Error values determined from Monte-Carlo routine.

Species	**Peak areas (%)** **pH 5** **1×10^{-2} M As(III)**
As^{5+}	3.9±1.6
As^{3+}	11.2±1.5
As^{2+}	44.7±1.9
As^{0}	34.1±1.8
As^{1-}	6.1±1.3

Table 3.5. Peak areas for component peaks used in fitting the O(1s) peak for FeS_m. Error values determined from Monte Carlo routine.

Species	**Peak Areas (%)**			
	pH 5 (no As added)	**pH 5 1×10^{-2} M As(III)**	**pH 9 (no As added)**	**pH 9 2.5×10^{-4} M As(III)**
O^{2-}	67.3±2.8	44.6±7.3	14.5±9.4	49.9±2.3
$(OH)^-$	23.7±2.9	40.6±3.4	34.2±4.2	32.9±1.6
H_2O_{ads}	9.2±3.3	14.8±6.0	51.3±11.6	17.2±2.1

a surface that is dominated by O^{2-} species (67.3±2.8%), whereas the O(1s) spectrum for the pH 9 sample (no As) shows a much lower O^{2-} contribution (14.5±9.4%). The dominant species on the pH 9 sample is adsorbed H_2O (51.3±11.6%), which is consistent with previous results indicating a near-surface environment that is less oxidized than the pH 5 sample. The presence of 34.2±4.2% $(OH)^-$, along with Fe(II)-O, suggests the possible formation of Fe(II)-Fe(III)-(oxy)hydroxides.

In addition to the overall loss of the O(1s) peak area that is shown after reaction with As(III) at pH 5 (see Table 3.1), there is also a shift in oxygen speciation from surface oxides (O^{2-}) being the primary component at pH 5 (no As) to O^{2-} and $(OH)^-$ contributing equal parts to the total signal after the addition of As. The oxygen speciation of the pH 9 sample also changes after equilibration with As(III), shifting its distribution from primarily H_2O_{ads} and $(OH)^-$ to a surface that is primarily composed of O^{2-} and $(OH)^-$. This shift suggests that ferric hydroxyoxides and/or oxyhydroxides may be forming as oxidation products in the reaction that reduces As(III).

Conclusions

Nanoparticles of FeS_m were synthesized and reacted with As(III) in anoxic solutions at pH 5 and 9. FeS_m was also equilibrated in pH 5 and 9 solutions without As(III) for comparison. Electron diffraction patterns obtained by HRTEM confirm the presence of FeS_m in all of the samples and show no difference in the structure of FeS_m nanoparticles before and after reaction with As. However, XPS surface analysis of the samples equilibrated without As(III) revealed that the pH 5 sample had a more oxidized surface composition than the pH 9 sample, as indicated by the higher concentration of O (~three

times the pH 9 sample) and the larger percentage of Fe(III) species making up the total Fe ($2p_{3/2}$) peak. The pH dependence of surface oxides may reflect enhanced dissolution of FeS_m in more acidic environments and the formation of sorbed Fe(II) and/or reactive surface sites that can be easily oxidized during brief exposure to air. These observations may help to elucidate the mechanisms involved in the oxidation of FeS_m to greigite, a process that has been shown to be important in the formation of pyrite. Understanding how the composition of FeS_m changes under different environmental conditions is also essential for modeling the removal of As(III) or other toxic elements from groundwater in permeable reactive barriers (PRBs) that utilize iron sulfide-based materials.

In addition, HAADF-STEM and EDX were used to identify and characterize the distribution of arsenic phases that result from FeS_m reacting with As(III) at pH 5 and 9. At pH 5, arsenic sulfide phases are shown to precipitate among the FeS_m particles as discrete phases that are often elongated and several microns in length. The particles are most likely an amorphous hydrous phase of arsenic sulfide. The oxidation state of As in the arsenic sulfide precipitates at higher loadings was determined to be 'realgar-like' from XPS results showing that >75% of the As 3d peak area was due to As with oxidation states between 0 and +2. Discrete, arsenic sulfide precipitates are absent at pH 9, but arsenic is uniformly distributed on the FeS_m, suggesting that uptake may be due to the sorption of As(III) oxyanions and/or the precipitation of highly dispersed arsenic sulfides on FeS_m. The concentration of As at pH 9 was too low to be detected by XPS, but the more than two-fold increase in the concentration of Fe(III) species after the reaction with As(III) suggests that As may be oxidizing the surface and leaving reduced As phases sorbed to FeS_m.

These results support the XAS results of Gallegos *et al.* (2007) which indicate an As uptake mechanism involving reduction from the original +III valence and formation of a realgar-like solid at both pH 5 and 9. Determination of the amorphous nature of the arsenic sulfide particles by HRTEM in this study is significant. For instance, transient changes in the pH/Eh conditions within PRBs may re-release As to ground water by the oxidative dissolution of arsenic sulfide. Lengke and Tempel (2003) have shown that the rate of oxidative dissolution of amorphous As_4S_4 is greater by a factor of 2 than that of crystalline realgar (As_4S_4).

Arsenic sulfides, such as realgar and orpiment (As_2S_3), are generally associated with sulfide ores formed under high-temperature conditions in the Earth's crust, but several investigators have speculated that the formation of arsenic sulfides in sedimentary environments occurs either as a by-product of microbial metabolism (Demergasso *et al.*, 2007) or by abiotic processes (Sadiq, 1997). Most of these studies have used indirect methods, such as chemical extraction and thermodynamic modeling, in order to predict arsenic sulfide mineralogy. Synchrotron-based spectroscopic methods have also shown arsenic-bearing phases with the local structure of realgar or orpiment forming in low temperature environments (O'Day *et al.*, 2004). However, the composition and structure of these phases is still poorly known due to their nanoscale dimensions and low concentrations. Identification of arsenic sulfide precipitates by HAADF-STEM techniques along with determination of As oxidation states characteristic of realgar and orpiment lend further support to the formation of arsenic sulfide phases in sedimentary environments.

In summary, the results indicate that As(III) uptake from solution by FeS_m is strongly dependent on pH and redox conditions. An amorphous arsenic sulfide precipitate accounts for the removal of As(III) from solution under acidic conditions, and the formation of As(III)-oxyanion surface complexes and/or precipitation of reduced As phases under alkaline conditions. The identification of the composition, structure, and distribution of these particles can be used to refine quantitative, biogeochemical models that explain and predict As concentrations in natural waters. These data are equally important in developing strategies for the use of FeS_m in PRBs.

Acknowledgments

This research was supported by a National Science Foundation NIRT Grant EAR-0403732. Partial support for this work was provided by funds from the Strategic Environmental Research and Development Program (SERDP) Grant CU 1375 from the Department of Defense, and the Department of Army, Contract W912HQ-04-C-0035. This paper has not been subject to agency review; it therefore does not necessarily reflect the sponsors' views.

References

Bahl, M.K. and Watson, R.L. (1976) Evidence for shakeup satellites due to surface contamination in arsenic metal and its compounds. Surface Science, 54, 540-546.

Becker, U. and Hochella, M.F.(1996) The calculation of STM images, STS spectra, and XPS peak shifts for galena: New tools for understanding mineral surface chemistry. Geochimica et Cosmochimica Acta, 60, 2413-2426.

Becker, U., Munz, A.W., Lennie, A.R., Thornton, G. and Vaughan, D.J. (1997) The atomic and electronic structure of the (001) surface of monoclinic pyrrhotite (Fe7S8) as studied using STM, LEED and quantum mechanical calculations. Surface Science, 389, 66-87.

Becker, U. and Rosso, K.M. (2001) Step edges on galena (100): Probing the basis for defect driven surface reactivity at the atomic scale. American Mineralogist, 86, 862-870.

Becker, U., Rosso, K.M. and Hochella, M.F. (2001) The proximity effect on semiconducting mineral surfaces: A new aspect of mineral surface reactivity and surface complexation theory? Geochimica et Cosmochimica Acta, 65, 2641-2649.

Bostick, B.C. and Fendorf, S. (2003) Arsenite sorption on troilite (FeS) and pyrite (FeS_2). Geochimica et Cosmochimica Acta, 67, 909-921.

Boursiquot, S., Mullet, M. and Ehrhardt, J.J. (2002) XPS study of the reaction of chromium (VI) with mackinawite (FeS). Surface and Interface Analysis, 34, 293-297.

Cullen, W.R. and Reimer, K.J. (1989) Arsenic speciation in the environment. Chemical Reviews, 89, 713-764.

Demergasso, C.S., Chong, G., Escudero, L., Mur, J.J.P. and Pedros-Alio, C. (2007) Microbial precipitation of arsenic sulfides in Andean salt flats. Geomicrobiology Journal, 24, 111-123.

Farquhar, M.L., Charnock, J.M., Livens, F.R. and Vaughan, D.J. (2002) Mechanisms of arsenic uptake from aqueous solution by interaction with goethite, lepidocrocite, mackinawite, and pyrite: An X-ray absorption spectroscopy study. Environmental Science & Technology, 36, 1757-1762.

Fendorf, S., Eick, M.J., Grossl, P. and Sparks, D.L. (1997) Arsenate and chromate retention mechanisms on goethite .1. Surface structure. Environmental Science & Technology, 31, 315-320.

Gallegos, T.J., Hyun, S.P. and Hayes, K.F. (2007) Spectroscopic investigation of the uptake of arsenite from solution by synthetic mackinawite. Environmental Science & Technology, 41, 7781-7786.

Gallegos, T.J., Hyun, S.P. and Hayes, K.F. (2008) Model predictions of realgar precipitation by reaction of As(III) with synthetic mackinawite under anoxic conditions. Environmental Science & Technology, 42, 9338-9343.

Gupta, R.P. and Sen, S.K. (1974) Calculation of multiplet structure of core para-vacancy levels. Physical Review B, 10, 71-77.

Henderson, A.D. and Demond, A.H. (2007) Long-term performance of zero-valent iron permeable reactive barriers: A critical review. Environmental Engineering Science, 24, 401-423.

Herbert, R.B., Benner, S.G., Pratt, A.R. and Blowes, D.W. (1998) Surface chemistry and morphology of poorly crystalline iron sulfides precipitated in media containing sulfate-reducing bacteria. Chemical Geology, 144, 87-97.

Hunger, S. and Benning, L.G. (2007) Greigite: a true intermediate on the polysulfide pathway to pyrite. Geochemical Transactions, 8.

Jeong, H.Y., Lee, J.H. and Hayes, K.F. (2008) Characterization of synthetic nanocrystalline mackinawite: Crystal structure, particle size, and specific surface area. Geochimica Et Cosmochimica Acta, 72, 493-505.

McIntyre, N.S., Davidson, R.D. and Mycroft, J.R. (1996) Quantitative XPS measurements of some oxides, sulphides and complex minerals. Surface and Interface Analysis, 24, 591-596.

Mullet, M., Boursiquot, S., Abdelmoula, M., Genin, J.M. and Ehrhardt, J.J. (2002) Surface chemistry and structural properties of mackinawite prepared by reaction of sulfide ions with metallic iron. Geochimica et Cosmochimica Acta, 66, 829-836.

Mycroft, J.R., Bancroft, G.M., McIntyre, N.S., Lorimer, J.W. and Hill, I.R. (1990) Detection of sulfur and polysulfides on electrochemically oxidized pyrite surfaces by X-ray photoelectron-spectroscopy and raman-spectroscopy. Journal of Electroanalytical Chemistry, 292, 139-152.

Nesbitt, H.W., Bancroft, G.M., Pratt, A.R. and Scaini, M.J. (1998) Sulfur and iron surface states on fractured pyrite surfaces. American Mineralogist, 83, 1067-1076.

Nesbitt, H.W. and Muir, I.J. (1994) X-ray photoelectron spectroscopic study of a pristine pyrite surface reacted with water-vapor and air. Geochimica et Cosmochimica Acta, 58, 4667-4679.

Nesbitt, H.W., Muir, L.J. and Pratt, A.R. (1995) Oxidation of arsenopyrite by air and air-saturated, distilled water, and implications for mechanism of oxidation. Geochimica et Cosmochimica Acta, 59, 1773-1786.

Nickson, R.T., McArthur, J.M., Ravenscroft, P., Burgess, W.G. and Ahmed, K.M. (2000) Mechanism of arsenic release to groundwater, Bangladesh and West Bengal. Applied Geochemistry, 15, 403-413.

O'Day, P.A., Vlassopoulos, D., Root, R. and Rivera, N. (2004) The influence of sulfur and iron on dissolved arsenic concentrations in the shallow subsurface under changing redox conditions. Proceedings of the National Academy of Sciences of the United States of America, 101, 13703-13708.

Ohfuji, H. and Rickard, D. (2006) High resolution transmission electron microscopic study of synthetic nanocrystalline mackinawite. Earth and Planetary Science Letters, 241, 227-233.

Penrose, W.R. (1974) Arsenic in marine and aquatic environments: analysis, occurrence, and significance. CRC Critical Reviews in Environmental Control, 4, 465-482.

Pierce, M.L. and Moore, C.B. (1982) Adsorption of arsenite and arsenate on amorphous iron hydroxide. Water Research, 16, 1247-1253.

Pratt, A.R., Muir, I.J. and Nesbitt, H.W. (1994) X-ray photoelectron and auger-electron spectroscopic studies of pyrrhotite and mechanism of air oxidation. Geochimica et Cosmochimica Acta, 58, 827-841.

Pratt, A.R. and Nesbitt, H.W. (2000) Core level electron binding energies of realgar (As_4S_4). American Mineralogist, 85, 619-622.

Rickard, D. (1997) Kinetics of pyrite formation by the H_2S oxidation of iron (II) monosulfide in aqueous solutions between 25 and 125 degrees C: The rate equation. Geochimica et Cosmochimica Acta, 61, 115-134.

Rickard, D. and Luther, G.W. (2007) Chemistry of iron sulfides. Chemical Reviews, 107, 514-562.

Rickard, D.T. (1969) The chemistry of iron sulphide formation at low temperatures. Stockholm Contributions in Geology, 20, 67-95.

Sadiq, M. (1997) Arsenic chemistry in soils: An overview of thermodynamic predictions and field observations. Water Air and Soil Pollution, 93, 117-136.

Schaufuss, A.G., Nesbitt, H.W., Kartio, I., Laajalehto, K., Bancroft, G.M., and Szargan, R. (1998) Incipient oxidation of fractured pyrite surfaces in air. Journal of Electron Spectroscopy and Related Phenomena, 96, 69-82.

Schoonen, M.A.A. and Barnes, H.L. (1991) Reactions forming pyrite and marcasite from solution: II. via FeS precursors below 100°C. Geochimica et Cosmochimica Acta, 55, 1505-1514.

Smedley, P.L. and Kinniburgh, D.G. (2002) A review of the source, behaviour and distribution of arsenic in natural waters. Applied Geochemistry, 17, 517-568.

Swedlund, P.J. and Webster, J.G. (1999) Adsorption and polymerisation of silicic acid on ferrihydrite, and its effect on arsenic adsorption. Water Research, 33, 3413-3422.

Thomas, J.E., Jones, C.F., Skinner, W.M. and Smart, R.S. (1998) The role of surface sulfur species in the inhibition of pyrrhotite dissolution in acid conditions. Geochimica et Cosmochimica Acta, 62, 1555-1565.

Utsunomiya, S. and Ewing, R.C. (2003) Application of high-angle annular dark field scanning transmission electron microscopy, scanning transmission electron microscopy-energy dispersive X-ray spectrometry, and energy-filtered transmission electron microscopy to the characterization of nanoparticles in the environment. Environmental Science & Technology, 37, 786-791.

Vaughan, D.J. (2006) Arsenic. Elements, 2, 71-75.

Vaughan, D.J. and Lennie, A.R. (1991) The iron sulfide minerals – their chemistry and role in nature. Science Progress, 75, 371-388.

Vaughan, D.J. and Ridout, M.S. (1971) Mossbauer studies of some sulphide minerals. Journal of Inorganic & Nuclear Chemistry, 33, 741-746.

Wagner, C.D., Davis, L.E., Zeller, M.V., Taylor, J.A., Raymond, R.H., and Gale, L.H. (1981) Empirical atomic sensitivity factors for quantitative-analysis by electron-spectroscopy for chemical analysis. Surface and Interface Analysis, 3, 211-225.

Waychunas, G.A., Fuller, C.C., Rea, B.A. and Davis, J.A. (1996) Wide angle X-ray scattering (WAXS) study of "two-line" ferrihydrite structure: Effect of arsenate sorption and counterion variation and comparison with EXAFS results. Geochimica et Cosmochimica Acta, 60, 1765-1781.

Wilkin, R.T. and Barnes, H.L. (1996) Pyrite formation by reactions of iron monosulfides with dissolved inorganic and organic sulfur species. Geochimica et Cosmochimica Acta, 60, 4167-4179.

Wolthers, M., Charlet, L., Van der Weijden, C.H., Van der Linde, P.R. and Rickard, D. (2005) Arsenic mobility in the ambient sulfidic environment: Sorption of arsenic(V) and arsenic(III) onto disordered mackinawite. Geochimica et Cosmochimica Acta, 69, 3483-3492.

Wolthers, M., Van der Gaast, S.J. and Rickard, D. (2003) The structure of disordered mackinawite. American Mineralogist, 88, 2007-2015.

Yamaguch, S. and Wada, H. (1972) Greigite as seed for crystal growth of pyrrhotite. Journal of Crystal Growth, 15, 153-154.

Chapter 3

A first principles study of the oxidation energetics and kinetics of realgar

Abstract

Quantum-mechanical calculations allow resolving and quantifying in detail important aspects of reaction mechanisms such as spin transitions and oxygen dissociation that can be the major rate-limiting steps in redox processes on sulfide and oxide surfaces. In addition, this knowledge can help experimentalists in setting up the framework of rate equations that can be used to describe the kinetics of, e.g., oxidation processes. The unique molecular crystal structure of realgar, As_4S_4 clusters held together by van der Waals bonds, allows for a convenient quantum-mechanical (q.m.) cluster approach to investigate the thermodynamics and kinetic pathways of oxidation. The interaction of As_4S_4 clusters with oxygen and co-adsorbed ions provides a model system for understanding the molecular-scale processes that underpin empirically-derived rate expressions, and provides clues to the oxidation mechanisms of other sulfides and oxides. Two activated processes are shown to dominate the kinetics of oxidation by molecular oxygen: i) a paramagnetic ($^3O_2$) to diamagnetic ($^1O_2$) spin transition and ii) oxygen

dissociation on the surface, in that order. The activation energies for the spin transition and O_2 dissociation step were determined to be 1.1 eV (106 kJ/mol) and 0.9 eV (87 kJ/mol), respectively, if molecular oxygen is the only reactant on the surface. In the case of As_4S_4, q.m. calculations reveal that $^3O_2$ transfers its spin to the cluster and forms a low-spin, peroxo intermediate on the surface before dissociating. The adsorption of a hydroxide ion on the surface proximate to the $^3O_2$ adsorption site changes the adsorption mechanism by lowering the activation energy barriers for both the spin transition (0.30 eV / 29 kJ/mol) and the O_2 dissociation step (0.72 eV / 69 kJ/mol). Thus, while spin transition is rate limiting for oxidation with O_2 alone, dissociation becomes the rate-limiting step for oxidation with co-adsorption of OH^-. First-principles, periodic calculations of the realgar $(\bar{1}20)$ surface show that the energetics and structural changes that accompany oxidation of As_4S_4 clusters on the surface are similar to those involving individual As_4S_4 clusters. Thus, assuming that an As_4S_4 cluster with an adsorbed hydroxyl group is a reasonable approximation of the surface of As_4S_4 at high pH, the theoretically calculated oxidation rate ($\sim 10^{-10}$ $mol \cdot m^{-2} \cdot s^{-1}$) is of the same order as empirically-derived rates from experiments at T = 298 K, pH = 8, and similar dissolved oxygen concentrations. In addition, the co-adsorption of other anions found in alkaline waters (*i.e.,* carbonate, bicarbonate, sulfate, and sulfite) were shown to energetically promote the oxidation of As_4S_4 (on the order of 5-40 kJ/mol depending on the co-adsorbed anion, OH^-, CO_3^{2-}, HCO_3^-, SO_4^{2-}, or SO_3^{2-}, and accounting for changes in the hydration of products and reactants). The effect of the co-adsorbate on the kinetics and thermodynamics of oxidation is due to each adsorbate modifying the electronic and structural environment of the other adsorption site.

Activation-energy barriers due to spin transitions are rarely discussed in the literature as key factors for controlling oxidation rates of mineral surfaces, even though the magnitude of these barriers is enough to alter the kinetics significantly. The attenuation of the activation energy by co-adsorbed anions suggests the possibility of pH- or p(co-adsorbate)-dependent activation energies that can be used to refine oxidation rate laws for sulfide minerals and other, especially semiconducting minerals, such as oxides.

Introduction

The oxidation of sulfide minerals (abiotic and microbially-mediated) is a key process of electron cycling and the driving force behind the mobilization and geochemical cycling of many elements at the Earth's surface. It is also a significant human-health and environmental concern because the oxidative dissolution of these minerals can increase the concentration of toxic elements and decrease pH values in natural waters. Sulfide oxidation kinetics is based on the development of empirically-derived rate laws, but the actual reaction mechanisms are far from being completely understood. Detailed studies of the atomic and electronic structure of the most common sulfide surfaces such as pyrite (Eggleston *et al.*, 1996; Guevremont *et al.*, 1997, 1998a-d; Rosso *et al.*, 1999) and galena (Eggleston and Hochella, 1990, 1991, 1993, 1994; Becker and Hochella, 1996; De Giudici and Zuddas, 2001) are beginning to reveal these mechanisms and provide insight as to what pathways contribute to the overall reaction rate. The two most important oxidants of sulfides are molecular oxygen, O_2, and Fe^{3+}. The mechanisms involving these oxidants are complex, being made up of multiple steps with multiple intermediates. However, what is common to the rate law of minerals such as pyrite, galena, and arsenic

sulfides such as realgar and orpiment, are activation energies >40 kJ/mol (FeS_2: McKibben and Barnes, 1986; PbS: De Giudici *et al.*, 2005; As_4S_4 and As_2S_3: Lengke and Tempel, 2003). Activation energies of this magnitude typically indicate that the reaction is controlled by a surface reaction and not by diffusion of reactants to or products from the reaction site (e.g., through the Stern layer at the mineral water interface) (Lasaga, 1981). Another consistency in the rate laws for the oxidation of these sulfides by O_2 is an O_2 reaction order close to 0.5. Square-root dependencies of the rate on the concentration of O_2 suggest that O_2 dissociation is one of the rate-determining steps in the reaction mechanism.

It is instructive to consider what is known about the dissociation of oxygen in other disciplines in order to better understand the constraints of reaction mechanisms on natural surfaces. It is well known to industrial catalyst developers that the sluggish kinetics of oxygen dissociation/reduction is often assumed the rate-limiting step in electro-chemical/-catalyst systems. Activation energies for a wide variety of electrocatalysts at zero overpotential generally fall within the range of 40-100 kJ/mol (Kinoshita, 1992). In bio-organic systems, the kinetic bottleneck to O_2 dissociation is attributed to the paramagnetic quality of molecular oxygen (*i.e.,* two unpaired electrons each having a spin state of 1/2 for a total resultant spin, S, of 1, making ground state oxygen a triplet $(2S+1) = 3$ or $^3O_2$). The reaction of $^3O_2$ with low-spin (*i.e.,* a total S of 0, making a ground state singlet $(2S+1) = 1$) organic molecules or surfaces is a spin-prohibited process due to the law of conservation of angular spin momentum (Minaev, 1982). The activation energy required to overcome the spin-prohibited process is about 100 kJ/mol, and the production of radicals is typically the lowest energy path for the reaction to

proceed (Sawyer, 1991). Thus, most oxidation processes that use $^3O_2$ as an oxidant will be rate-limited by the activation of paramagnetic $^3O_2$ on the surface.

However, despite the significant effect that activation of $^3O_2$ has on catalysis and corrosion rates, there is still much to be understood about this fundamental reaction. Evidence of this is based on the fact that catalyst developers have only made modest progress in reducing the activation energy barrier. Behler *et al.* (2005) have claimed that despite decades of research in surface science, the initial step in the interaction between oxygen and the Al(111) surface (*i.e.,* often called the "most simple" metal surface) remains poorly understood. Activation energy barriers due to spin transition are rarely discussed in terms of the oxidation of mineral surfaces even though the magnitude of these barriers will significantly affect kinetics and can be the major rate-controlling step. Some organisms have found a way around these barriers, using oxygenase enzymes to activate triplet dioxygen and lower the activation energy for the spin transition via multiple electron and proton transfers and multiple biradical intermediates (Prabhakar *et al.*, 2004). Catalyst developers often utilize co-adsorbates (*i.e.,* "promoters" or adatoms) to enhance a catalyst's reactivity towards forming a desired product.

For many adsorption/desorption reactions taking place on semiconducting mineral surfaces, the electronic properties of the surface introduce the possibility for unique behavior, such as the coupling of spatially separated redox species by electron transfer through near surface layers. This indirect interaction is described as a "proximity effect" whereby a chemical reaction at one surface site modifies the reactivity of a remote surface site several Angstroms or even nanometers away (Becker *et al.*, 2001). The attenuation of the reactivity is due to the co-adsorbate modifying the electron density

and/or the structure of the surface in the nearby vicinity; however, the extent, to which electronic or structural changes play a role in proximity effects, is often difficult to discern. Previous ab-initio modeling studies have identified indirect interactions between co-adsorbed oxygen atoms and between adsorbed oxygen atoms and point defects on vacuum-terminated galena (100) (Rosso and Becker, 2003). In their study, both the co-adsorbed O and the point defect can energetically promote the adsorption of an O adsorbate upwards of 1 nm away on the surface. These observations help to describe, for instance, the progressive oxidation of certain sulfide minerals by patchwork or island growth on flat terraces.

Realgar, As_4S_4, is an ideal candidate to investigate surface proximity effects and $^3O_2$ spin transitions as they relate to oxidation because of: i) its importance to the biogeochemical cycling of As in low-temperature environments, ii) its well-defined oxidation kinetics that indicate the mechanism is rate-limited by the dissociation of O_2 on the surface (Lengke and Tempel, 2003, 2005), and iii) its unique molecular crystal structure that allows for a convenient quantum-mechanical cluster approach used in this study.

The unit cell of realgar, $As_{16}S_{16}$, is composed of four distinct covalently-bonded As_4S_4 molecular units. These As_4S_4 molecules interact via relatively weak van der Waals forces as shown in Figure 4.1, thus making it one of a host of arsenic sulfides with similar compositions and structures that are true molecular crystals (Makovicky, 2006). Planes of weak van der Waals forces within the structure are found parallel to the cleavage and crystal growth faces, thus, adsorption and oxidation events can be uncoupled from the rest of the surface by treating each individual As_4S_4 molecular unit independently.

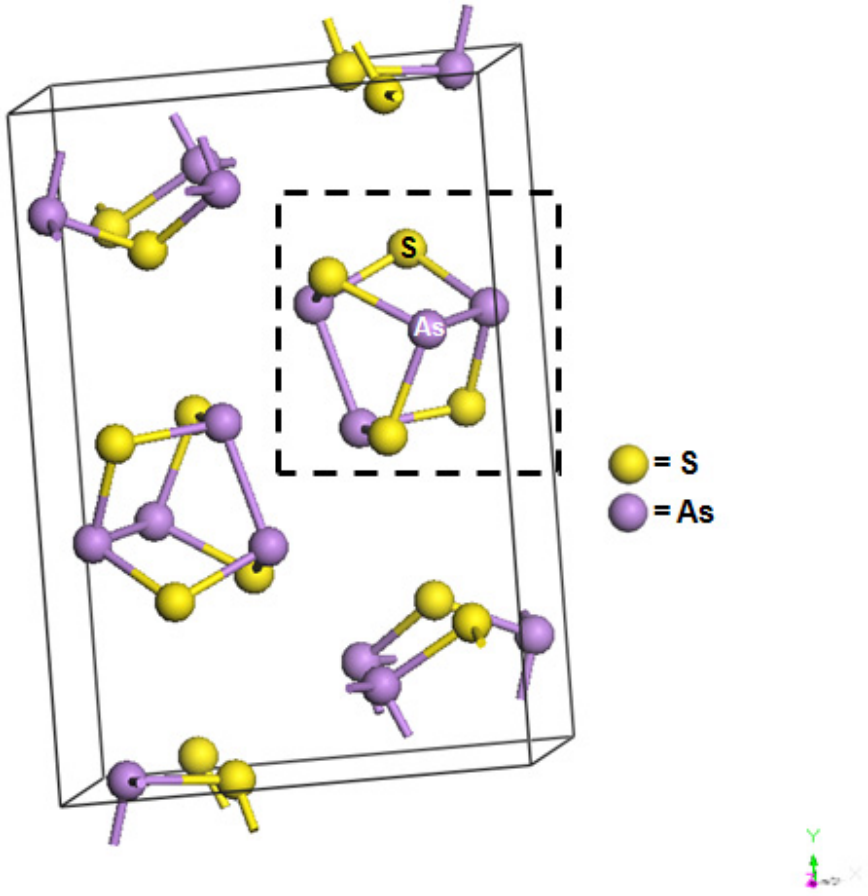

Figure 4.1. Unit cell of realgar, $As_{16}S_{16}$, showing individual As_4S_4 molecular units or "clusters" held together by van der Waals forces to form a true molecular crystal. The dashed box contains an individual As_4S_4 used in cluster calculations.

Realgar is typically associated with hydrothermal sulfide ore bodies, and therefore often implicated, along with arsenian pyrite, as a source of As in acid mine drainage. Realgar is difficult to identify in reduced sediments because of its fine-grained nature (*i.e.,* micro- to nano-dimensions), its low abundance, and instability in air at these dimensions. However, surface-probe and synchrotron techniques reveal the presence of arsenic sulfides in low-temperature, anoxic sediments (Soma *et al.*, 1994), and O'Day *et al.* (2004) identify realgar as the primary arsenic-bearing phase in sulfate-reducing conditions in sediments. Recent studies, including O'Day *et al.* (2004), suggest that insoluble arsenic sulfides like realgar and orpiment play a role, along with arsenian pyrite, in controlling the levels of arsenic in groundwater at the oxic-anoxic redox boundary (Kim *et al.*, 2000). The magnitude of the role depends on the rate of microbially-mediated sulfate reduction (Inskeep *et al.*, 2002) as well as microbes that directly precipitate realgar (Huber *et al.*, 2000). However, abiotic formation of realgar must also be considered in light of studies by Renock *et al.* (2009) and Gallegos *et al.* (2007) that show discrete realgar-like precipitates forming as a result of As(III) reacting with synthetic mackinawite, FeS. Lengke and Tempel (2003, 2005) have determined the rate of oxidative dissolution of realgar and shown that rates increase with increasing pH values. Kim *et al.* (2000) suggest that the release of As into groundwater is positively correlated to bicarbonate concentration.

The focus of this investigation is to use a quantum-mechanical modeling approach to: i) describe the kinetic bottlenecks for oxidation of realgar, As_4S_4, by determining the activation energy barriers for the paramagnetic ($^3O_2$) to diamagnetic ($^1O_2$) spin transition and the dissociation of O_2 on the surface, and ii) quantify the effect of adsorbate-

adsorbate interactions on the thermodynamics and kinetics of the oxidation of As_4S_4. The adsorbate species chosen for this study (*i.e.,* hydroxide, carbonate, bicarbonate, sulfite, and sulfate) are based on their presence in neutral to alkaline waters and their ability to act as polarizing agents on surfaces. The results of this study will provide a molecular basis for interpreting and refining experimentally-derived rate laws for the oxidation of realgar.

Theoretical methods

Computational methods and parameters

Ab-initio cluster calculations were performed using a Becke, three parameter, Lee-Yang-Parr (B3LYP) functional, which hybridizes the exchange-correlation in density functional theory (DFT) with the exact exchange integral using a Hartree-Fock (HF) approach (Becke, 1993) as implemented by the program package Gaussian 03 (Frisch *et al.*, 2003). The basis set used to describe the valence electrons was a Los Alamos National Laboratory 2-double-zeta LANL2DZ basis set with core basis functions replaced by a small-core pseudopotential or effective core potential (ECP) (Wadt and Hay, 1985). A split-valence 3-21g basis set was used for calculations involving Na^+ (Pietro *et al.*, 1982). Polarization functions were added to provide flexibility within the basis set to account for bonding of adsorbates to As_4S_4 surfaces. All geometry optimizations were run with atoms fully relaxed unless otherwise stated. A Polarizable Continuum Model (PCM) developed by Cossi *et al.* (1996) was used to approximate hydration energies of all adsorbate configurations. In this approach, the solvent is treated as a dielectric fluid (dielectric constant, $\varepsilon = 78$) instead of explicit solvent molecules, and

a generalized Born approximation is used to estimate the radius of the cavity around each atom in the dielectric fluid.

Calculations of adsorption energies on periodic slabs were performed using a density functional theory-based (DFT) quantum mechanical code, CASTEP (CAmbridge Serial Total Energy Package) which is part of the Materials Studio Modeling package (version 4.0) (Segall *et al.*, 2002). In this periodic approach, a generalized gradient approximation (GGA) with exchange correlation approximated by the Perdew-Burke-Ernzerhof (PBE) functional (Perdew *et al.*, 1996) was used with planewaves as basis functions to model the wavefunctions that describe the distribution of electrons in the system. A k-point spacing of 0.05 $Å^{-1}$ and a planewave cutoff energy of 320 eV were chosen in the slab calculations. A vacuum gap of 12 Å between periodic slabs was found to result in negligible slab-slab interactions.

Calculation of adsorbate-adsorbate interactions

In order to determine how the energetics and kinetics of oxidation are affected by co-adsorbates on the surface, the adsorption energies of each single adsorption and co-adsorption case are determined. In terms of kinetics, determining the energy of activated states on the surface, and thus, the activation energy barriers associated with these states (*i.e.,* spin transition or O_2 dissociation) requires that the energy of the system is determined for each step along a reaction path (e.g., by approaching a reactant in steps of 0.1 Å and allowing relaxation $\perp$ to the reaction path). In our model, temperature-dependent vibrations and rotations of the adsorbate and the surface are neglected. The total energy from the calculation is related to the ground-state electron density of the

system in the gas phase. Adsorption energies, ΔE_{ads}, are computed as the difference of the sum of the total energy (*i.e.,* surface + adsorbate(s)) and the sum of the total energies of the reactants.

A generalized method for calculating the energetics and kinetics of co-adsorption is shown in the schematic in Figure 4.2 and based on the balanced equation (1):

$$\Delta E_{ads}(\text{surface-A}) + \Delta E_{ads}(\text{surface-B}) \leftrightarrow \Delta E_{ads}(\text{A-surface-B}) + \Delta E_{ads}(\text{surface}) \quad (1)$$

where A is an oxidant (*i.e.,* dissociated O or O_2 in this study), B is a co-adsorbate, and "surface" is the surface where adsorption takes place (*i.e.,* As_4S_4 clusters, periodic realgar slabs, or a $2\times As_4S_4$ dimer in this study). The ΔE_{coads} value is defined using the following equation:

$$\Delta E_{coads} = \Delta E_{ads}(\text{A-surface-B}) + \Delta E_{ads}(\text{surface}) - \Delta E_{ads}(\text{surface-A}) - \Delta E_{ads}(\text{surface-B}) \quad (2)$$

Equation (2) is convenient because it shows that if [ΔE_{ads}(A-surface-B) + ΔE_{ads}(surface)] is more negative than the sum of the ΔE_{ads} of each individual adsorption case [ΔE_{ads}(surface-A) + ΔE_{ads}(surface-B)] (*i.e.,* ΔE_{coads} is negative), then the oxidation is more energetically favorable when a co-adsorbate is present on the surface (*i.e.,* the co-adsorbate promotes oxidation). The ΔE_{coads} gives the magnitude of the energy modification to the adsorption energy of A (or B) due to direct electrostatic ($E_{direct(A-B)}$) interaction between A and B and indirect interaction between A and B through the near-surface layers ($E_{indirect(A-B)}$) by the equation:

$$\Delta E_{coads} = E_{direct(A-B)} + E_{indirect(A-B)} \quad (3)$$

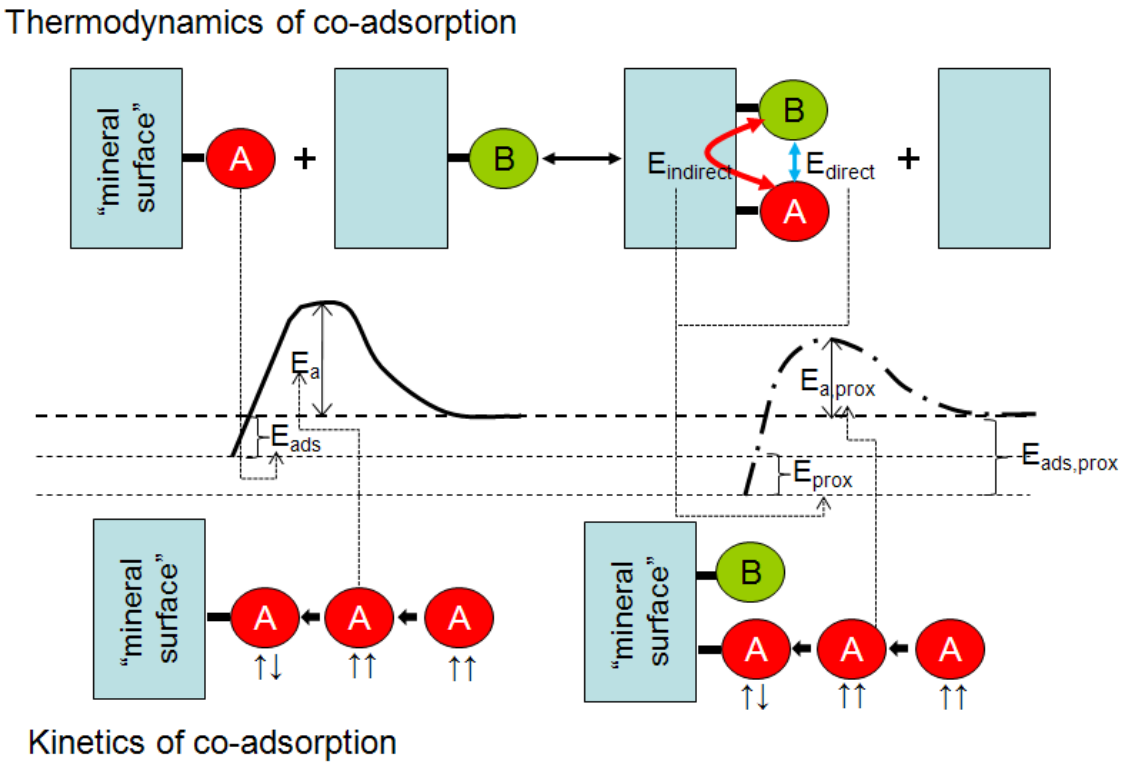

Figure 4.2. Schematic model showing the reaction that is used to calculate the thermodynamics of the interaction energy (top) and kinetic effects (bottom) between co-adsorbed species on a semiconducting surface. The gray box represents a semiconducting surface through which electron transfer is possible. A and B represent two different species adsorbed to the surface that can directly interact (E_{direct}) via Coulomb forces and indirectly ($E_{indirect}$) via the electronic structure of the mineral. E_{ads} is the energy associated with the adsorption of either A or B on the surface. $E_{ads+prox}$ is the synergistic energy associated with the simultaneous adsorption of A and B on the surface. In this case, the result of the proximity effect is to lower the total energy involved in adsorption of A and B to the surface (*i.e.,* co-adsorption results in a net energy gain as shown in the reaction energy profile). The kinetic effect is shown (bottom) for species A approaching the surface. E_a is the activation energy that must be overcome for a high spin A to interact with a low spin surface (*i.e.,* spin transition). $E_{a,prox}$ is the activation energy associated with high spin A approaching a surface proximate to an adsorbed species B. In this case, the effect of B is to lower the activation energy of the spin transition.

A positive $E_{direct(A-B)}$ indicates a net repulsive coulombic force between like-charged adsorbates A and B (*i.e.,* A and B carry the same sign of charge), whereas a negative $E_{direct(A-B)}$ indicates a net energy decrease associated with an attractive interaction. $E_{direct(A-B)}$ values are obtained by removing the surface from the optimized structure and determining the energy of the Coulomb interaction between A and B from their respective charges and the distance between adsorbates. The actual charges of the adsorbates are approximated by using the Mulliken charges from the optimized structure. These charges are then used to calculate $E_{direct(A-B)}$ in order to maintain consistency between each adsorption case. Once $E_{direct(A-B)}$ is determined, the indirect electronic interaction through the near-surface region, $E_{indirect(A-B)}$, can be obtained from equation (3).

In summary, negative values of ΔE_{coads} indicate the synergistic effect of favorable co-adsorption with respect to individual adsorption of two species. Combinations of negative values of $\Delta E_{indirect}$ with positive values of ΔE_{direct} indicate that the repulsive direct electrostatic interaction between two adsorbates (e.g., two negatively charged ones or one negative one, such as $(OH)^-$, and one that becomes negative during adsorption due to electron transfer, such as O_2) is, to a certain degree, compensated by a favorable long-range electron transfer through the near-surface region of the mineral.

Results and discussion

Energetics of adsorption and co-adsorption to As_4S_4

The first step in evaluating the initial oxidation event on the As_4S_4 surface is to determine how water, oxygen, and ionic species commonly found in neutral to alkaline

solutions interact with As_4S_4. The emphasis on neutral to alkaline conditions is based on studies that show an increase in the rate of oxidative dissolution of realgar with increasing pH (Lengke and Tempel, 2003, 2005). Other studies suggest that the leaching of As into groundwater is driven by direct interaction of carbonates and bicarbonates with realgar and other As-sulfide minerals in aquifer rocks (Kim *et al.*, 2000).

A ball-and-stick model showing the atomic arrangement of the As_4S_4 molecular unit is shown in the dashed inset in Figure 4.1 (point group symmetry: -42m). This structure, designated As_4S_4 (or the "cluster") for the remainder of the text, serves as the substrate for all subsequent adsorption calculations. As_4S_4 by itself has a net neutral charge, and the most energetically favorable spin configuration is 0 unpaired spins according to the B3LYP approach. For an isolated cluster, the calculated As-As and As-S bond length is 2.65 Å and 2.27 Å, respectively. These values are slightly larger than the experimental values for the As-As bond (2.57 Å) and As-S (2.23-2.25 Å) determined by Mullen and Nowacki (1972) for a realgar crystal. It is difficult to determine if this difference stems from the cluster versus periodic approach or from the quantum-mechanical parameters used (*i.e.,* HF-DFT hybrid approach, basis set, pseudopotential). Part of this difficulty is based on the fact that it is difficult to calculate realgar correctly using a periodic approach because the van-der-Waals interactions between the clusters are underestimated using a classical quantum-mechanical approach that solves the ground state of the Schrödinger equation. In this case, it is reasonable to assume a lengthening of the As_4S_4 bonds due to the relaxation of the molecular unit in a vacuum versus one that is held together by van der Waals forces in bulk realgar. The calculated bond lengths also agree with bond

lengths obtained by Banerjee *et al.* (2003) (As-As: 2.64 Å; and As-S: 2.27 Å) using B3LYP with a standard 6-311G* basis.

The adsorption energies and optimized geometries for the interaction of a single As_4S_4 cluster with water (H_2O), monatomic oxygen (O), hydroxide ion $(OH)^-$, carbonate ion $(CO_3)^{2-}$, bicarbonate ion $(HCO_3)^-$, sulfate ion $(SO_4)^{2-}$, and sulfite ion $(SO_3)^{2-}$ were determined. H_2O was added to assess the hydration energy of As_4S_4 for the dissociated, $H^+ + (OH)^-$, and undissociated case. Monatomic oxygen, O, was added as a neutral atom with no unpaired spins (S = 0) to mimic an initial product of dissociatively adsorbed O_2, a species involved in the oxidative dissolution of realgar. In addition to adsorption of single adsorbates, co-adsorption of $O + (OH)^-$, $O + (CO_3)^{2-}$, $O + (HCO_3)^-$, $O + (SO_4)^{2-}$, $O + (SO_3)^{2-}$ and $O + H_2O$ were also investigated to assess synergistic interactions between adsorbed oxygen, O_{ads}, and the co-adsorbate on the surface. Lewis bases, $(OH)^-$, $(CO_3)^{2-}$, $(HCO_3)^-$, $(SO_4)^{2-}$, and $(SO_3)^{2-}$ were considered in order to determine if the anion acts, as a polarizing agent, to transfer electron density through the cluster to the oxidant and energetically promote the reduction of O_{ads}.

As_4S_4 hydration

The hydration of As_4S_4 and the various adsorbates must be considered first in order to assess the overall energetics of oxidation and adsorption. In the case of a single H_2O molecule adsorbing to the cluster, the H_2O molecule pushes away from the cluster independent of its starting orientation. In each case, the H_2O molecule orients itself so that its negative dipole is ~3 Å above the As-As bond (not shown). Both the relatively weak adsorption energy (ΔE_{ads}, = -0.11 eV) and the large cluster-water separation

indicate a weak interaction with the surface. Co-adsorption of $(OH)^-$ and H^+ to As_4S_4 was also investigated to rule out the possibility that dissociated H_2O is stabilized on the surface. In this case, $(OH)^-$ bonds to an As atom and H^+ to either an adjacent S atom or one that is on the opposite end of the cluster. In each case of dissociated water adsorption, the cluster pulls apart by breaking an As-S bond and expands to maximize the distance between the H_{ads} and the hydroxyl hydrogen (not shown). However, the final energy for dissociated H_2O + As_4S_4 is ~0.5 eV higher in energy than molecular H_2O adsorption and was, therefore, not considered relevant to this study.

The relatively weak interaction between As_4S_4 and H_2O is due to the significant covalent bonding within the As_4S_4 molecule, and this property has experimental basis in mineral processing studies that classify realgar, along with minerals like talc, sulfur, graphite, molybdenite, and orpiment as naturally hydrophobic from their low critical surface tension of wetting values (Ozcan, 1992). This property allows realgar to be floated easily during mineral processing.

Hydration energies were determined using a polarizable continuum model (PCM) and were used to correct gas-phase adsorption energies for adsorbate- and co-adsorbate-cluster configurations. The hydration energy for each individual adsorbate is shown in Table 4.1 along with the experimental values and/or values derived from a thermodynamic model put forth by Rashin and Honig (1985) and Marcus (1994), respectively. Other than for Na^+, the PCM values are consistently less negative than literature values, and deviate by as much as 30% from the literature values for each adsorbate. Therefore, hydration energy values taken from the literature are used for ions in solution (*i.e.,* ions removed from the cluster). The hydration energy of an adsorbed

Table 4.1. Hydration energies for single ions calculated using B3LYP/PCM approach. A 3-21G* Gaussian-type basis set was used for Na^+, $(OH)^-$ and $(CO_3)^{2-}$ for comparison.

Species	**B3LYP/PCM hydration energies (eV)**	**ΔH_{hyd} (eV)**
Na^+	-4.82 eV (3-21G*)	-4.27 Rashin and Honig (1985); -4.30 Marcus (1994)
$(OH)^-$	-3.72 -3.87 (3-21G*)	-4.72 Rashin and Honig (1985); -5.39 Marcus(1994)
$(CO_3)^{2-}$	-10.92 -11.53 (3-21G*)	-14.46 Marcus (1994)
$(HCO_3)^-$	-3.10	-3.94 Marcus (1994)
$(SO_4)^{2-}$	-9.94	-10.73 Marcus (1994)
$(SO_3)^{2-}$	-9.74	-14.25 Marcus (1994)

ion on the surface of the cluster was determined by estimating the contribution to the total hydration energy (*i.e.,* E_{hyd} (total) = E_{hyd} (adsorbed ion) + E_{hyd} (cluster)) of the adsorbed ion alone, and then adjusting this value based on the known literature value for the adsorbate. This adjustment is required to account for the energy to remove part of the hydration shell of the adsorbing ion and the energy for the removal of some water molecules from the surface (which depends on the local structure of water at the interface). The true adsorption energy reflects whether the binding energy of the adsorbate compensates for the loss of part of the hydration shells. All subsequent adsorption energies are corrected to account for changes in the hydration energies of the ion(s) and the cluster after adsorption.

Adsorption to a single As_4S_4 cluster

The lowest energy atomic arrangement of O + As_4S_4 was determined by placing O at different starting positions around As_4S_4 and optimizing the geometry. The O atom finds several local energy minima around As_4S_4 depending on its starting position. However, the lowest-energy atomic configuration for As_4S_4 + O is one in which the O atom takes on a bridging configuration between two As atoms as shown in Figure 4.3a. As_4S_4 expands to accommodate the O atom, and in doing so, the four As-S bonds (closest to the O) increase from 2.27 Å to 2.30 Å. In order to accommodate the expansion, the As-As

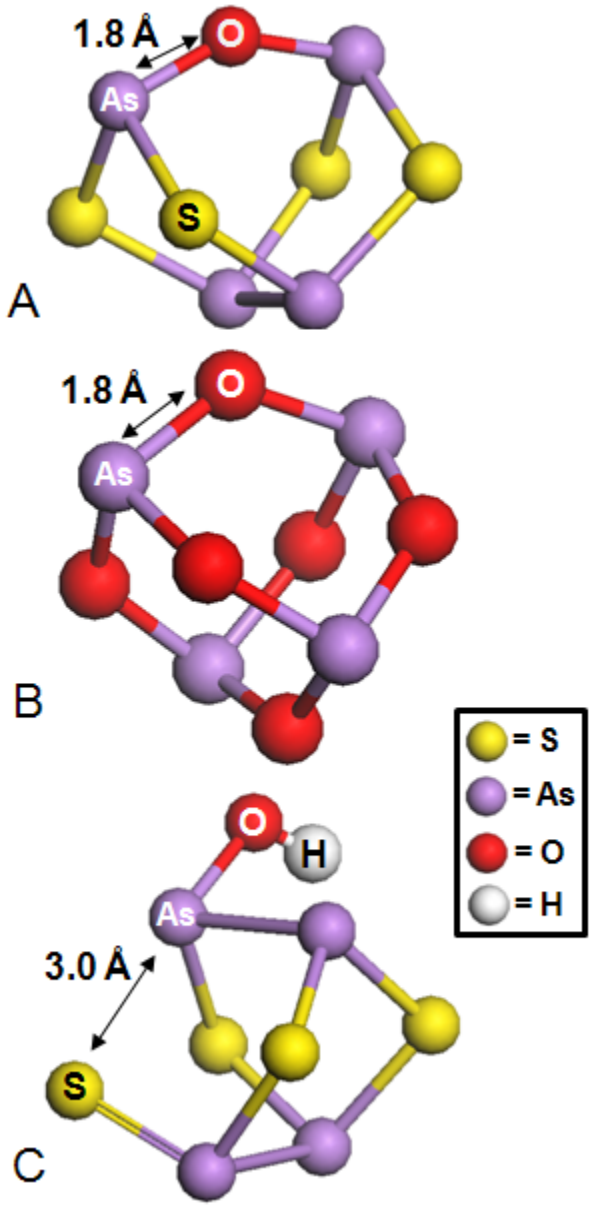

Figure 4.3. Ball-and-stick models of: A) As_4S_4 + O; B) As_4O_6 molecular unit in arsenolite; C) As_4S_4 + $(OH)^-$ showing the breaking of the As-S bond opposite the adsorption site.

bond distance on the opposite side of the cluster shrinks from 2.65 Å to 2.61 Å. The As-O bond length is 1.80 Å, which is similar to the As-O bond length (1.79 Å) found in the mineral arsenolite (As_2O_3). It is interesting to note that the As_4S_4-O configuration is an intermediate structure between As_4S_4 to As_4O_6, the molecular unit found in arsenolite (Figure 4.3b). The As_4O_6 molecule is similar to As_4S_4 except that all the S atoms are replaced by O, and two additional O's bridge the As atoms on each end of the As tetrahedron. The adsorption energy, ΔE_{ads}, for the oxidation of As_4S_4 by monatomic low-spin O is -1.72 eV, assuming that the O originates from paramagnetic $^3O_2$.

The reactions between As_4S_4 and either $(OH)^-$, $(CO_3)^{2-}$, $(HCO_3)^-$, $(SO_4)^{2-}$, and $(SO_3)^{2-}$ were determined in the same way as for O. Each adsorbate binds to different sites and takes on different orientations according to local energy minima on the reactive surface of As_4S_4. However, the most energetically favorable adsorption site for $(OH)^-$ is bonding directly to As in the cluster (all As atoms being equivalent). Hydroxide bonding to As is more favorable than bonding to S in the cluster by 1.7 eV. The formation of a As-OH bond (As-OH bond length = 1.86 Å) is accompanied by either a lengthening (or breaking) of either the As-S or As-As bond in line with As-OH in order to maintain a pyramidal bonding configuration as shown in Figure 4.3c. Breaking an As-S bond from the original cluster (ΔE_{ads} = -0.46 eV) is more favorable to breaking an As-As bond by ~0.3 eV. This observation is consistent with the conclusions of Babic and Rabii (1989) who suggest that the As-As bond is ~0.5 eV stronger than the As-S bond in As_4S_4. Interestingly, when two $(OH)^-$ ions adsorb simultaneously to two adjacent As atoms, the cluster completely unravels and forms a perfectly linear molecule with $(OH)^-$ ions at each end. The unraveling of the cluster in this way suggests that a non-oxidative process may be another

mechanism responsible for dissolution, particularly at high pH values where there is higher surface coverage of hydroxyl groups.

The $(CO_3)^{2-}$, $(HCO_3)^{-}$, $(SO_4)^{2-}$, and $(SO_3)^{2-}$ adsorbates act in a similar fashion to $(OH)^{-}$ in that one of the O atoms bond with As in the cluster, accompanied by a breaking (or lengthening in the case of $(HCO_3)^{-}$) of the As-S bond that is in line with the As-O bond (not shown). ΔE_{ads} values for $(CO_3)^{2-}$ of -0.07 eV (shown in Table 4.2) suggest that the initial adsorption of the carbonate ion to realgar is energetically favorable. This has experimental basis in that stable arseno-carbonate complexes (for example: $As(CO_3)^{2-}$, $As(CO_3)^{+}$, and $As(CO_3)(OH)_2^{-}$) have been suggested to take part in the leaching of arsenic in anaerobic systems (Kim et al., 2000), and that $(CO_3)^{2-}$ was more efficient than $(HCO_3)^{-}$ in arsenic leaching. The positive adsorption energies for $(HCO_3)^{-}$, $(SO_4)^{2-}$, and $(SO_3)^{2-}$ (Table 4.2) suggest that the adsorption of these ions (without the presence of a co-adsorbate) is energetically unfavorable.

Co-adsorption of O_2 and different anions to a single As_4S_4 cluster

The adsorption energy and optimized geometry for O + $(OH)^{-}$, O + $(CO_3)^{2-}$, O + $(HCO_3)^{-}$, O + $(SO_4)^{2-}$, and O + $(SO_3)^{2-}$ were determined in order to evaluate if co-adsorption of a second species energetically promotes or hinders oxidation of As_4S_4. For each co-adsorption case involving an anion, the lowest energy configuration involves O bridging two As atoms and the anion bonding to an As atom (Figure 4.4a-e). Collectively, the negative ΔE_{ads} values (corrected for hydration) for each co-adsorption case (shown in Table 4.3, column 2) indicate that the initial oxidation event on the surface is thermodynamically favorable. The difference between the adsorption energies

Table 4.2. Adsorption energies for As_4S_4 + a single adsorbate corrected for hydration.

Adsorbate configuration	$\Delta E_{ads} + \Delta E_{hyd}$ **(eV)**
As_4S_4-O	-1.72
As_4S_4-$(OH)^-$	-0.46
As_4S_4-$(CO_3)^{2-}$	-0.07
As_4S_4-$(HCO_3)^-$	+0.39
As_4S_4-$(SO_4)^{2-}$	+0.41
As_4S_4-$(SO_3)^{2-}$	+0.33

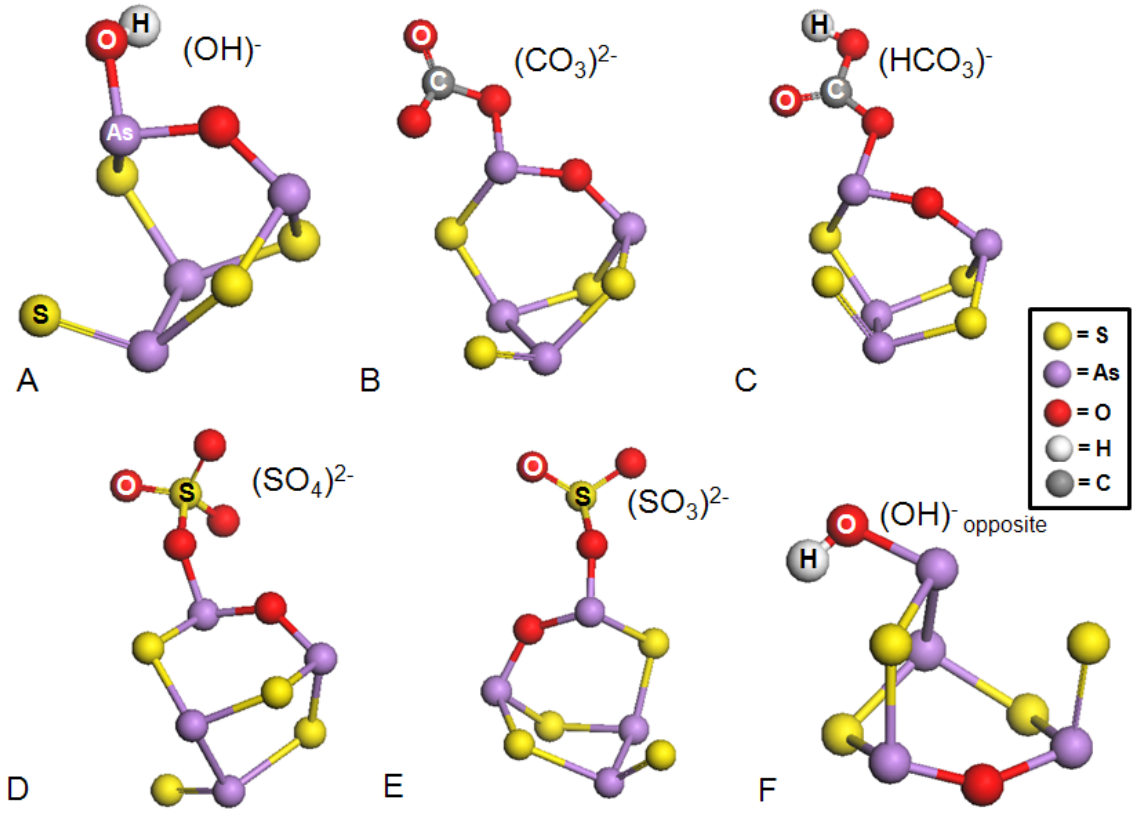

Figure 4.4. Ball and stick models of co-adsorption cases: A) $As_4S_4 + O + (OH)^-$; B) $As_4S_4 + O + (CO_3)^{2-}$; C) $As_4S_4 + O + (HCO_3)^-$; D) $As_4S_4 + O + (SO_4)^{2-}$; E) $As_4S_4 + O + (SO_3)^{2-}$; F) $As_4S_4 + O + (OH)^-$ showing $(OH)^-$ bonding to the opposite side of the cluster from O.

Table 4.3. Calculated energy-distance data for co-adsorption of O and either H_2O or a co-adsorbed ion on the surface of As_4S_4. The "opp" subscript denotes an atomic configuration where the co-adsorbed ion is on the opposite side of the cluster from the O.

Composition	**O-co-adsorbate seperation (Å)**	**ΔE_{ads} (eV)**	**ΔE_{coads} (E_{direct} + $E_{indirect}$) (eV)**	**E_{direct} (eV)**	**$E_{indirect}$ (eV)**	**$\Delta E_{coad\text{-}hydration}$ (eV)**	**ΔE_{total} (eV)**
Neutral species							
As_4S_4-O-H_2O	5.65	-1.71	0.00	-0.01	-0.01	-	-
Univalent anions							
As_4S_4-O-$(OH)^-$	2.67	-2.51	-0.21	0.74	-0.95	-0.25	-0.46
As_4S_4-O-$(OH)^-$ opp	5.41	-2.54	-0.10	0.36	-0.46	-0.13	-0.23
As_4S_4-O-NaOH	2.82	-2.26	-0.26	0.57	-0.83	0.19	-0.07
As_4S_4-O-NaOH opp	5.48	-2.51	-0.23	0.27	-0.5	-0.07	-0.3
As_4S_4-O-$(HCO_3)^-$	3.84	-1.44	-0.05	0.79	-0.74	-0.07	-0.12
As_4S_4-O-$(HCO_3)^-$ opp	6.41	-1.44	-0.11	0.52	-0.63	-0.01	-0.12
Divalent anions							
As_4S_4-O-$(CO_3)^{2-}$	3.8	-2.02	-0.31	1.65	-1.96	0.05	-0.26
As_4S_4-O-$(CO_3)^{2-}$ opp	6.73	-2.05	-0.28	0.49	-0.77	0.03	-0.25
As_4S_4-O-Na_2CO_3	4.3	-0.94	-0.40	2.44	-2.84	-0.06	-0.46
As_4S_4-O-$(SO_4)^{2-}$	3.84	-1.60	-0.23	1.76	-1.99	-0.06	-0.29
As_4S_4-O-$(SO_4)^{2-}$ opp	7.30	-1.54	-0.21	1.02	-1.23	-0.02	-0.23
As_4S_4-O-$(SO_3)^{2-}$	3.97	-1.69	-0.33	1.66	-1.99	0.02	-0.31
As_4S_4-O-$(SO_3)^{2-}$ opp	7.37	-1.65	-0.30	0.91	-1.21	0.04	-0.26

for $(OH)^-$ bonding directly to an O-bridged As atom and an As on the opposite side of the cluster (Figure 4.4f) is -0.03 eV (ΔE_{ads} = -2.51 eV *vs.* -2.54 eV) as shown in Table 4.3. Likewise, the difference in ΔE_{ads} for $(CO_3)^{2-}$, $(HCO_3)^-$, $(SO_4)^{2-}$, and $(SO_3)^{2-}$ bonded on the same or opposite side of the cluster from O (not shown) are all less than 0.1 eV.

The ΔE_{coads} values in Table 4.3 give the magnitude of the modification to the O adsorption energy that is due to direct electrostatic (E_{direct}) interaction between charged adsorbates and indirect interaction through the cluster ($E_{indirect}$). Thus, negative ΔE_{coads} values in Table 4.3 indicate a synergistic interaction between O_{ads} and the co-adsorbate that yields a net energy gain (*i.e.,* co-adsorption is more energetically favorable than the sum of each single adsorption case). The magnitude of the energy gain (~0.05-0.85 eV) depends on the type of co-adsorbing species with it generally being the case that divalent anions > univalent anions > neutral molecules (*i.e.,* H_2O). H_2O was the only co-adsorbate studied that showed no effect on the adsorption of O. The ΔE_{coads} values deviate only slightly when the co-adsorbate bonds to the opposite side of the cluster from O. Thus, the strength of the interaction between adsorbates persists over the range of possible distances separating adsorbates on a single As_4S_4 cluster, and these distances are shown in Table 4.3 to reach upwards of 7.0 Å. This is not surprising since adsorbates or surface defects have been shown to affect the reactivity of a remote surface site upwards of 1 nanometer away on other semiconducting mineral surfaces, such as galena and pyrite (Rosso and Becker, 2003). This indirect interaction has been termed the "proximity effect" and is described as the phenomenon whereby a chemical reaction at one surface site modifies the reactivity of a remote surface site several Angstroms or even nanometers away (Becker *et al.*, 2001).

In order to test electron transfer and synergistic co-adsorption in the presence of a counter-cation, Na^+ was chosen as a representative for such co-adsorption with $(OH)^-$. Two Na^+ cations were included in the co-adsorption of $(CO_3)^{2-}$. In both cases, the presence of $Na^+(s)$ allows more energy to be gained from co-adsorption (~ 0.1 eV).

For each of the co-adsorption cases, O_{ads} is reduced on the surface as indicated by negative Mulliken charges. Thus, the "direct" electrostatic force between the negatively polarized O_{ads} and the anion co-adsorbates is repulsive, and this results in a positive coulombic energy between them as shown in Table 4.3. However, the magnitude of $E_{indirect}$ is significant enough, in every case in this study (except H_2O), to overcome E_{direct} repulsion over distances that are limited, in this system, only by the size of As_4S_4 plus the bonding distance of the adsorbate (~ 7 Å). $E_{indirect}$ is a measure of the magnitude of the indirect interaction between adsorbates occurs as a result of either: 1) electronic interactions mediated by the near surface bands through the As_4S_4 cluster, and/or 2) interactions due to deformation or breaking of bonds within the cluster. To a certain extent, this division is arbitrary (e.g., because it is arbitrary to define what bond lengthening value is declared broken) and it is often difficult to distinguish between the different contributions.

A note about hydration: the change in the energy of hydration (ΔE_{hyd}) in going from the single adsorbate case to the co-adsorbate case was determined by equation 4:

$$\Delta E_{coad\text{-}hyd} = E_{hyd}\,(\text{co-ads. case}) + E_{hyd}\,(As_4S_4) - \Sigma E_{hyd}\ (\text{single-ads. case}) \qquad (4)$$

Negative values for $\Delta E_{coad\text{-}hyd}$ indicate that hydration energy is gained from having both adsorbates adsorb to the same cluster, and so the total energy gained is a sum of ΔE_{coads} and $\Delta E_{coad\text{-}hyd}$ (*i.e.,* $\Delta E_{total} = \Delta E_{coads} + \Delta E_{coad\text{-}hyd}$) as shown in Table 4.3. These

values are included in Table 4.3 to show that even in cases where the ΔE_{hyd} is slightly positive, the ΔE_{coads} is more than enough to compensate for the loss of hydration energy and make the overall adsorption energetically favorable.

The interaction of the co-adsorbate with the O_{ads} through As_4S_4 can be quantified/visualized in different ways: (i) by the synergistic energy of the co-adsorption (ΔE_{coads}) of a Lewis base and O on As_4S_4 (see Table 4.3), (ii) by the amount of electron transfer to the O_{ads}, and (iii) using the visualization of the charge distribution in different adsorbate configurations.

In the case of As_4S_4 + O, approximately 0.42 units of charge are transferred from As_4S_4 to O_{ads}. The two As atoms that form bonds with O show the greatest change in Mulliken charge (M.C.) after O adsorption (ΔM.C. = +0.27); however, charge is redistributed throughout the whole cluster in order to accommodate O_{ads}. Co-adsorption of an electron-donating Lewis base, either $(OH)^-$, $(CO_3)^{2-}$, $(HCO_3)^-$, $(SO_4)^{2-}$, or $(SO_3)^{2-}$, has the effect of polarizing the cluster and pushing electrons to the O_{ads} site. Table 4.4 shows the charge transferred from the co-adsorbate to the cluster (*i.e.,* ΔM.C. after adsorption) and the Mulliken charge of O_{ads} for each case. In general, the greater the charge density transferred from the co-adsorbate to the cluster, the more negative the ΔE_{coads}. Thus, the differences in the ΔE_{coads} for the different anions can be described by their ability to donate electrons to the surface (*i.e.,* their basicity or nucleophilicity). In the cases with Na^+(s), the presence of the cation(s) enables more charge to be transferred from the anion and increases the negative charge on O_{ads}. Thus, the most significant increases in the O_{ads} charge are with $(CO_3)^{2-}$ in the presence of two Na^+ counterions,

Table 4.4. Charge transferred from the co-adsorbate to the cluster (*i.e.,* ΔM.C. after adsorption) and the Mulliken charge of O_{ads} for each co-adsorption case.

Composition	**O_{ads} M.C.**	**Charge transferred from co-adsorbate**
As_4S_4-O-H_2O	-0.41	-0.05
As_4S_4-O-$(OH)^-$	-0.46	-0.70
As_4S_4-O-$(OH)^-$ opp	-0.46	-0.70
As_4S_4-O-NaOH	-0.55	-0.82
As_4S_4-O-NaOH opp	-0.51	-0.83
As_4S_4-O-$(HCO_3)^-$	-0.39	-0.53
As_4S_4-O-$(HCO_3)^-$ opp	-0.45	-0.51
As_4S_4-O-$(CO_3)^{2-}$	-0.42	-1.0
As_4S_4-O-$(CO_3)^{2-}$ opp	-0.45	-1.0
As_4S_4-O-$Na_2(CO_3)$	-0.71	-1.1
As_4S_4-O-$(SO_4)^{2-}$	-0.41	-0.87
As_4S_4-O-$(SO_4)^{2-}$ opp	-0.45	-0.87
As_4S_4-O-$(SO_3)^{2-}$	-0.45	-1.0
As_4S_4-O-$(SO_3)^{2-}$ opp	-0.45	-1.0

and consequently, this case is the most energetically favorable from the ΔE_{coads} value (see Table 4.3). The positions of the Na^+ ions between O_{ads} and $(CO_3)^{2-}$ in the final structure (not shown) enhances the indirect interaction (as shown in Table 4.3) and enables O_{ads} to become more reduced on the surface. This case highlights the ability of counter-cations (or, in more general terms, high background electrolyte concentrations) to modulate proximity effects on surfaces. Thus, the ionic-strength dependent electrostatic potential distribution at the liquid-surface interface (*i.e.,* changes to the structure of the double layer or Helmholtz layer) must be considered when assessing synergistic co-adsorption on a surface.

It should be noted that even though significant charge density is transferred from the co-adsorbate to As_4S_4 in each case, the ΔM.C. of O_{ads} in the presence of a co-adsorbate is negligible or only slightly more negative compared to the case without. This may be due, in part, to the significant sharing of electron density between S, O_{ads}, and the co-adsorbate as shown from Laplacian electron density surfaces (next section).

The interaction of the co-adsorbate with O_{ads} is revealed using a Laplacian visualization of the charge distribution for the adsorbate configurations. Laplacians of the charge density show zero value surfaces of $\nabla^2\rho$. The quantity, $\nabla^2\rho$, is the (scalar) derivative of the gradient vector field of the electron density ρ (*i.e.,* the second derivative of the electron density), and it reveals surfaces that enclose regions where electronic charge is maximally concentrated (*i.e.,* defines the reactive surface of the molecule) (Schaftenaar and Noordik, 2000). The Laplacians of the charge density for the As_4S_4 + O, As_4S_4 + O + $(OH)^-$, and As_4S_4 + O + $(CO_3)^{2-}$ are shown in Figure 4.5a-c. Charge transfer from As_4S_4 to O occurs in regions of shared electron density. In the case of O

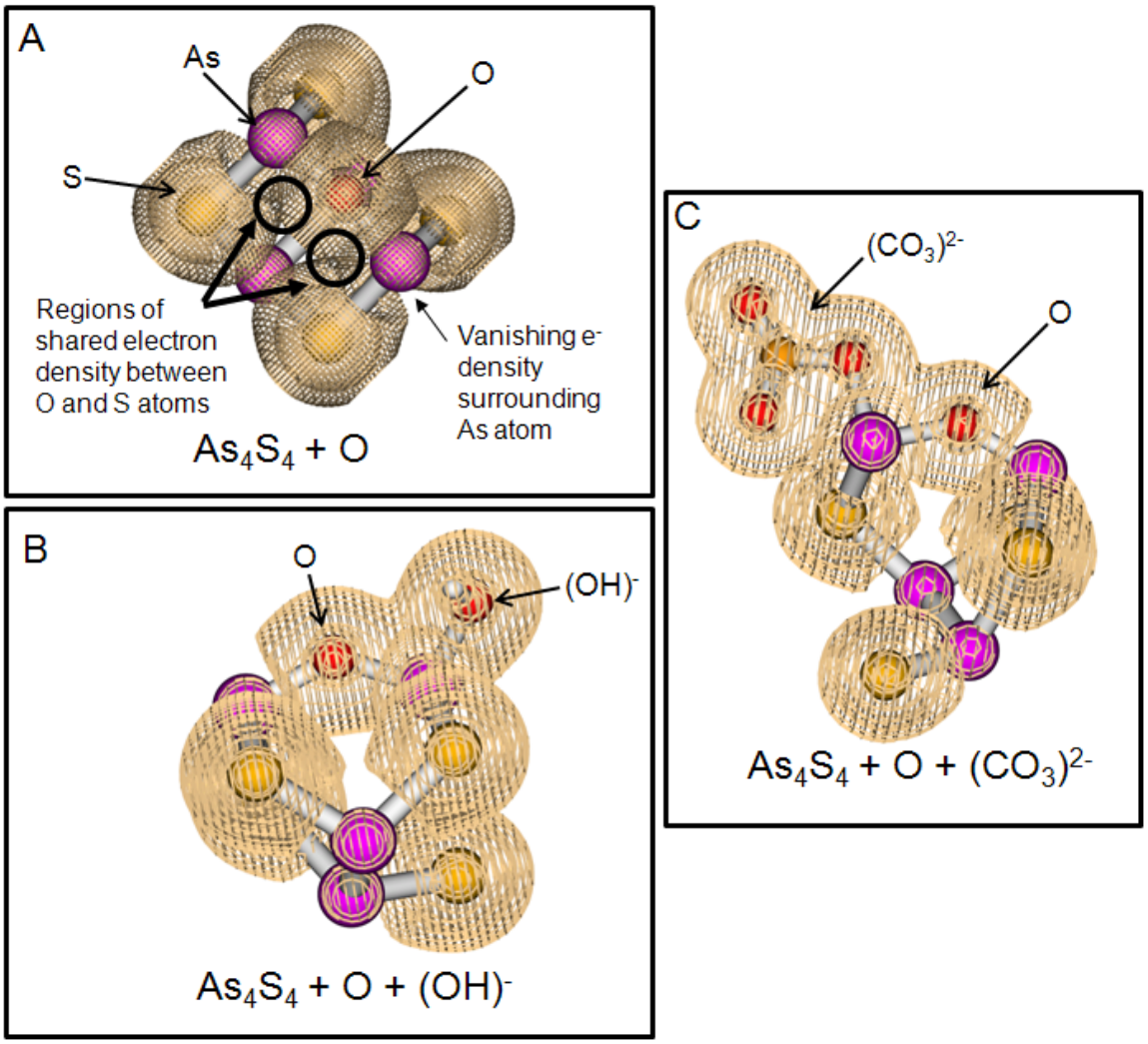

Figure 4.5. Ball and stick models of : A) As_4S_4 + O; B) As_4S_4 + O + $(OH)^-$; C) As_4S_4 + O + $(CO_3)^{2-}$. The mesh surface surrounding atoms indicates regions where electronic charge is maximally concentrated (*i.e.,* the Laplacian visualization of the reactive surface area). Regions of shared e^- density between O and each S atom in As_4S_4 (or saddle points in the reactive surface) are indicated by circles in Figure 4.5a (2 out of the 4 saddle points are indicated). Vanishing e^- density around As atoms in As_4S_4 indicate regions of diminished charge, and thus sites that are susceptible at attack by Lewis bases.

adsorption to As_4S_4 (Figure 4.5a), four areas of shared electron density (or "saddle points" in the reactive surface) are identified, between the electron density surface surrounding O and each S atom in the cluster. Vanishing electron density surrounding As show areas of diminished charge and also a degree of ionic bonding between As and S in the cluster. Most of the covalent character of As_4S_4 comes from shared electron density between the equatorial S atoms. This may explain why polar H_2O molecules cluster above the As-As bond in the models. These holes in the Laplacian surface also show sites where Lewis bases are likely to attack. The co-adsorption cases of $(OH)^-$ and $(CO_3)^{2-}$ with oxygen show the formation of significant regions of shared electron density between O_{ads} and the co-adsorbate. It is through these broad saddle points that electrons are transferred from the co-adsorbate to promote the reduction of O. The broad saddle points between adsorbates may also explain the negligible differences in Mulliken charge due to the difficulty in separating the integrated charge of O_{ads} from that of the co-adsorbate.

Co-adsorption on two adjacent As_4S_4 clusters

Adsorption on two adjacent As_4S_4 clusters, separated by a van-der-Waals gap, was evaluated to determine if oxidation of a As_4S_4 cluster is affected by adsorption of $(OH)^-$ or $(CO_3)^{2-}$ on the neighboring cluster (e.g., such as would be the case on a growth face or cleavage surface of realgar). This scenario would be more likely at pH values where there is low surface coverage of hydroxyl or carbonate groups. In this case, both As_4S_4 clusters were arranged to mimic their original symmetry and orientation in the 32-atom realgar unit cell. Both Hartree-Fock and B3LYP methods were used to calculate the

optimized geometry of the side-by-side clusters without adsorbates. The distance between adjacent clusters was best approximated by the B3LYP method perhaps due to the inclusion of electron correlation effects in this approach. However, the clusters still tend to pull apart from one another to distances that are larger than cluster-cluster distances in bulk realgar. The difference between the calculated and experimental value may arise from the lack of cluster neighbors in this approach versus the bulk or from the quantum-mechanical approach not precisely capturing the van-der-Waals (vdW) interaction between clusters. Though it is reasonable to assume some relaxation of the clusters on a realgar surface, the setup used in this study constrained the eight inner atoms (four S atoms and four As atoms closest to the vdW gap) so that the distances between the clusters are maintained. Figure 4.6 shows the optimized geometries of O adsorption to one cluster and $(OH)^-$ to the second (CO_3^{2-} not shown). There are no significant changes in the optimized geometries between the two-cluster and single-cluster cases, except that in the former, the clusters are less deformed due to the constrained atoms. The adsorption energies for the two-cluster cases are shown in Table 4.5 (hydration was not considered in this case). The ΔE_{coads} value for $(OH)^-$ and $(CO_3)^{2-}$ on a neighboring cluster are -0.03 eV and -0.08 eV, respectively. The negative ΔE_{coads} values are an order of magnitude less than co-adsorption on the same cluster, but indicate that adsorbates are interacting with one another from separate clusters. The $E_{indirect}$ for $(OH)^-$ is -0.22 eV, and for $(CO_3)^{2-}$ is -0.67 eV, indicating that indirect interactions between adsorbates over a distance of upwards of 10 Å (and across a van der Waals gap) are significant enough to overcome electrostatic forces between negatively charged O_{ads} and the co-adsorbing anion. The ΔE_{coads} value of -0.08 eV for the $(CO_3)^{2-}$ case is slightly more negative,

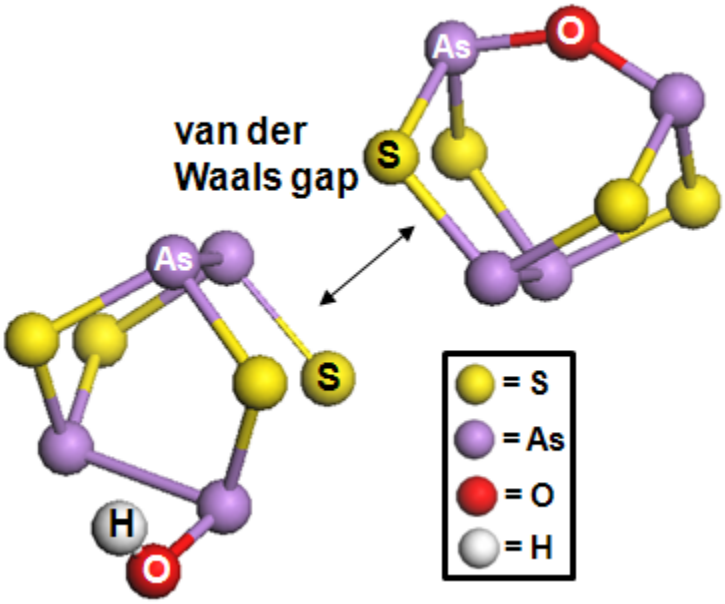

Figure 4.6. Ball and stick model of two adjacent As_4S_4 clusters separated by a van der Waals gap. An O atom is adsorbed to one As_4S_4 cluster and $(OH)^-$ to the other. $(OH)^-$ polarizes the cluster that it is adsorbed to as well as the neighboring As_4S_4 cluster across a van der Waals gap.

Table 4.5. Calculated energy-distance data for co-adsorption of O and $(OH)^-$ to adjacent As_4S_4 clusters.

Composition	**(O-co-adsorbate separation (Å)**	**ΔE_{coads} (E_{direct}+ $E_{indirect}$) (eV)**	**E_{direct} (eV)**	**$E_{indirect}$ (eV)**	**O_{ads} M.C.**	**Charge transferred from co-adsorbate**
As_4S_4-O— As_4S_4-OH^-	9.82	-0.03	0.19	-0.22	-0.43	-0.70
As_4S_4-O— As_4S_4-$(CO_3)^{2-}$	10.32	-0.08	0.59	-0.67	-0.45	-1.1

and suggests that $(CO_3)^{2-}$ is more effective in polarizing the first cluster and pushing electrons to the oxidized cluster. In both cases, the anion donates the same amount of charge as in the single cluster case (-0.7 u.c. for $(OH)^-$ and -1.1 M.C. for $(CO_3)^{2-}$); however, the ΔM.C. values of the oxidized cluster are -0.18 and -0.35 u.c. for the $(OH)^-$ and $(CO_3)^{2-}$ case, respectively. Although the energy gain is small for $(OH)^-$ or $(CO_3)^{2-}$ adsorbing to a separate cluster, it shows that some modification to the reactivity of the O_{ads} site is possible even across a van der Waals gap.

Periodic slab calculations

The cluster models reported up to this point allow the As_4S_4 molecule to freely break bonds and expand in any direction to accommodate changes in the structure due to adsorption. Therefore, the cluster calculations most accurately approximate adsorption processes occurring on step edges, kink sites, or at vacancies in a terrace. A periodic slab approach was used to determine whether an As_4S_4 cluster embedded in the $(\bar{1}20)$ realgar growth face would show similar synergistic interactions between adsorbates on a single cluster. The model used in the periodic calculation (shown in Figure 4.7) was a 2×1, two-layer deep slab with O and $(OH)^-$ adsorbing to both sides of the slab to minimize dipole effects (a dipole ⊥ to the slab would lead to unwanted slab-slab interaction in the 3D periodic setup). A Na^+ was added to both sides of the slab so that the net charge on each surface was zero. The lattice parameters and atomic positions of all atoms in the slab were constrained with the exception of the As_4S_4 cluster where adsorption is taking place. The oxidized As_4S_4 unit was free to relax, only constrained by the nearest neighbors laterally in the surface. All of the adsorbates were free to move anywhere

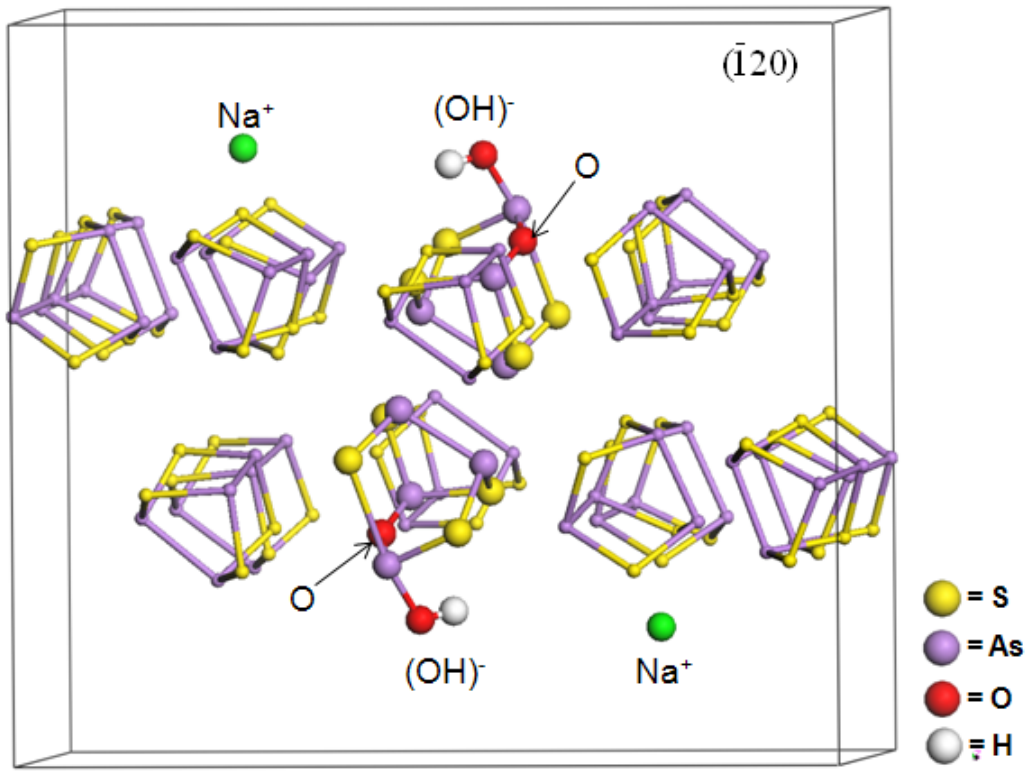

Figure 4.7. Periodic slab model showing co-adsorption of O and $(OH)^-$ to a single cluster on the $(\bar{1}20)$ surface of realgar. O and $(OH)^-$ is adsorbed to both sides of the two-layer deep slab to minimize dipole effects. A Na^+ was added to both sides of the slab so that the net charge on each surface was zero. The optimized geometry and co-adsorption energy for As_4S_{4slab}+ O + $Na^+(OH)^-$ is similar to the result from cluster calculations.

within the vacuum gap. The optimized geometry for As_4S_{4slab}+ O + $Na^+(OH)^-$ is similar to the result from cluster calculations (Figure 4.4a) except that the As_4S_4 slab does not break an As-S bond and expand to the same degree as in the cluster approach. Presumably, this is due to the oxidized cluster being constrained by its nearest neighbor clusters in the surface. The ΔE_{coads} value of -0.32 eV for the slab is similar to the value of its equivalent cluster calculation (-0.26 eV), and shows that the co-adsorbate promotes the oxidation of a realgar surface to a similar degree as the cluster case.

Kinetic study of molecular O_2 adsorption to As_4S_4

Up until now, only the energetics of the initial oxidation of As_4S_4 has been considered, *i.e.,* adsorption energies were calculated based on O already being dissociated before reacting with the cluster. Lengke *et al.* (2005) have suggested that the oxidation mechanism for realgar in near neutral to alkaline conditions involves the dissociation of adsorbed oxygen on the surface as indicated by the square-root dependency of their empirical rate law from the concentration of dissolved oxygen. We investigate this process by evaluating the energetics of paramagnetic $^3O_2$ and diamagnetic $^1O_2$ as a function of distance and finding that oxygen will only adsorb in an electronic state without unpaired spins. Therefore, in order for the oxidation of realgar to occur, $^3O_2$ must approach the surface, transfer its spin density, and dissociate. The same methodology used in the previous calculations was again applied to determine the reaction pathway for the oxidation of As_4S_4 by O_2. The effect of a co-adsorbing $(OH)^-$ was also considered in the calculations to determine if the co-adsorbate influences the kinetics of As_4S_4 oxidation as it does the thermodynamics.

Molecular O_2 adsorption to As_4S_4

The setup for these calculations has O_2 being moved in a step-by-step manner towards As_4S_4, and the adsorption energy for each intermediate configuration determined. Thus, an adsorption energy surface was determined for the reaction path. A minimum number of constraints were placed on the atoms so that the O_2 approach was controlled without affecting the reaction path. The distance, *z*, between the nearest oxygen atom in O_2 and an *x*-*y* plane containing one of the As-As bonds was fixed for each step. In this setup, the As-As bond was allowed to stretch and accept the bridging O. The O farthest from the cluster was free to move in all directions. The distance between the closer O atom and the *x*-*y* plane will be referred to as the O_2-As_4S_4 distance.

The total spin state was another constraint placed on each intermediate configuration. Thus, starting from oxygen being completely separated from the As_4S_4 cluster as O_2, to its adsorbed state as a dissociated O bridging two As atoms of the cluster, two different spin states were evaluated for each step. Because O_2 travels along the path of minimum energy, the reaction path was chosen based on the lowest energy spin state. It is known that the ground state for O_2 is the paramagnetic case, $^3O_2$, with two unpaired electrons generating a triplet (↑↑) "$^3\sum^-_g$" (*i.e.,* O_2 is a diradical). The low spin singlet case "$^1\sum^+_g$", $^1O_2$, (↑↓) was determined to be 1.67 eV above the ground state using the B3LYP approach.

Adsorption energy results for each spin configuration are shown in Figure 4.8 as a function of the O_2-As_4S_4 distance. The energy of each intermediate configuration was referenced to the total energy of As_4S_4 + $^3O_2$ at an infinite distance from one another,

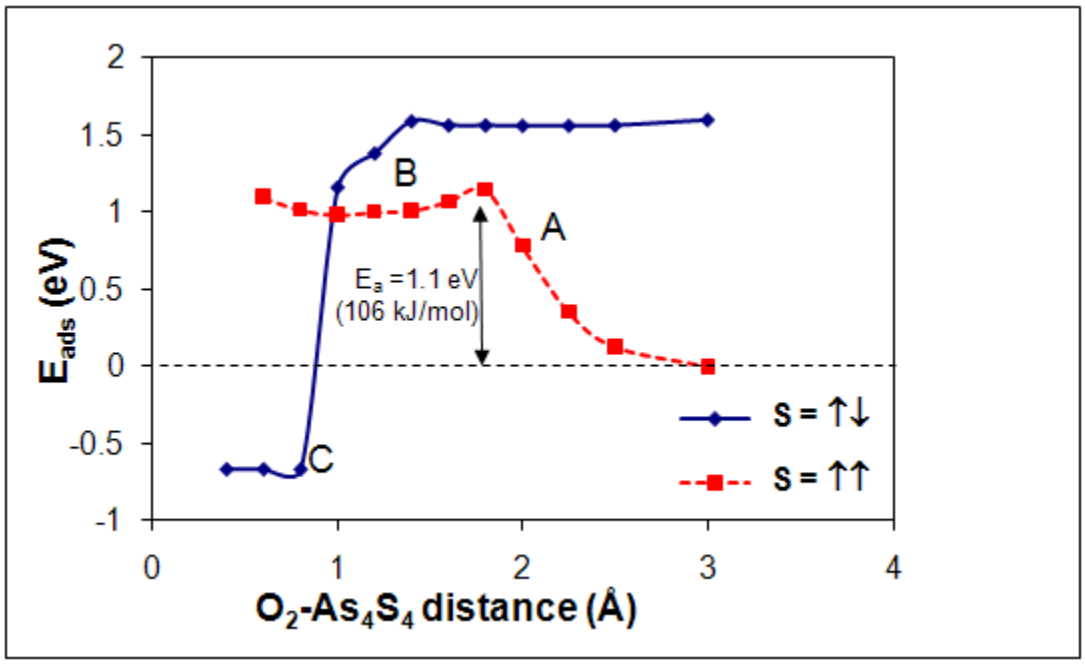

Figure 4.8. O_2 adsorption energy as a function of the O_2-As_4S_4 distance. Points A, B, and C correspond to O_2-As_4S_4 adsorption geometries shown in Figure 4.9a-c.n. The lowest energy state for an O_2 molecule approaching a As_4S_4 cluster (from infinite distance to 1 Å) is a triplet state (S = ↑↑). A singlet state (S = ↑↓) is lower in energy than the triplet state at O_2-As_4S_4 distances < 1 Å. An energy barrier of 1.1 eV (identified in the figure) must be overcome in order for $^3O_2$ to approach the As_4S_4 surface and react.

thus ensuring negligible interaction. Any value below $\Delta E_{ads} = 0$ is considered an energetically favorable adsorbate configuration. At the furthest distance from the cluster, $^3O_2$ is more stable than $^1O_2$ by 1.7 eV, as expected from the difference of the two O_2 molecules in different spin states by themselves. $^3O_2$ approaches the cluster in an "end-on" orientation, and at ~ 2 Å away, the wave functions of the molecule and the solid begin to overlap and ΔE_{ads} begins to increase (*i.e.,* force/energy would be needed to push $^3O_2$ closer to the surface, see Figure 4.9a). This behavior indicates that the reaction of $^3O_2$ and the low-spin As_4S_4 is energetically uphill and that an activation energy barrier must be overcome in order for them to approach any closer. The As-As bond distance increases significantly (>4 Å) when $^3O_2$ approaches within ~1.8 Å and the O nearest the cluster preferentially associates with one of the As atoms (Figure 4.9b). In the process, approximately 0.31 units of charge are transferred from As_4S_4 to O_2 and one unit of spin is transferred from O_2 to As_4S_4. The O atom closest to As_4S_4 assumes a nearly low-spin configuration (spin density = 0.3) and in doing so, the O-O bond length increases from 1.22 to 1.32 Å. Most of the spin density in As_4S_4 is accommodated by the As atom that is *not* directly bonded to O. At O_2-As_4S_4 distances of ~1 Å, the As_4S_4 + $^1O_2$ becomes the more energetically favorable spin state as shown by a crossing point between the triplet path and singlet path at ~ 1 Å (Figure 4.8). $^1O_2$ approaches in a "side-on" orientation roughly perpendicular to the As-As bond. The As-As distance decreases from the triplet state to accept $^1O_2$. At the smallest distances, O_2 bridges the As-As bond and forms a peroxo-adsorbate on the cluster (O-O bond distance = 1.44 Å) with each O bonding to one of the As atoms (Figure 4.9c). The ΔE_{ads} for the peroxo-adsorbate on the surface is ~-0.7 eV; however, this configuration is ~2.0 eV higher in energy than As_4S_4 +

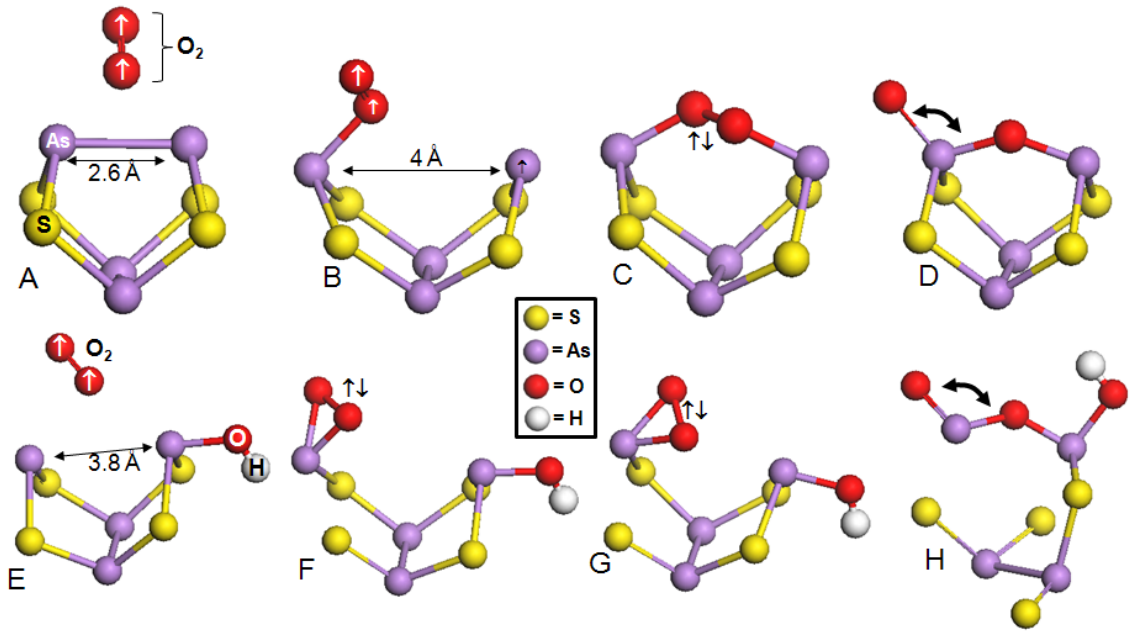

Figure 4.9. Ball-and-stick models showing intermediate adsorption geometries for O_2 approaching and dissociating on an As_4S_4 cluster (with and without a co-adsorbed OH^-): A) O_2 at 2.0 Å from As_4S_4 (S = ↑↑); B) O_2 at 1.4 Å from As_4S_4 (S = ↑↑); C) O-O peroxo-adsorbate adsorbed to As_4S_4 (S = ↑↓); D) dissociated O_2 adsorbed to As_4S_4 (S = ↑↓); E) O_2 at 2.0 Å from As_4S_4-OH (S = ↑↑); F) O_2 at 1.4 Å from As_4S_4-OH (S = ↑↓); G) O-O peroxo-adsorbate at 0.8 Å from As_4S_4-OH (S = ↑↓); H) dissociated O_2 adsorbed to As_4S_4-OH (S = ↑↓).

dissociated $^1O_2$ (Figure 4.9d). In the dissociated O_2 case, the distance between O atoms is 2.93 Å versus 1.44 Å for the peroxo-adsorbate. In order to determine the energy required to break the O-O bond, intermediate adsorbate configurations (*i.e.,* going from Figure 4.9c to 3.9d) were determined while varying the O-O distance between 1.5 and 2.75 Å. Figure 4.10 shows the ΔE_{ads} values increasing to a maximum value of +0.24 eV at ~2 Å, before dropping off to -2.8 eV for As_4S_4 + dissociated $^1O_2$. The energy barrier that must be overcome to break the O-O bond is 0.91 eV as shown in the Figure 4.10.

In summary, the As_4S_4 + O_2 calculations show two separate activation energies for oxidation: one associated with the $^3O_2$ to $^1O_2$ spin transition and the other for the breaking (or dissociation of O_2) on the cluster. The energy barrier for the $^3O_2$ to $^1O_2$ spin transition on the surface of As_4S_4 is approximately 1.1 eV (106.1 kJ/mol) as shown in Figure 4.8. One possible scenario is that $^3O_2$ approaches As_4S_4 in an end-on orientation, and when they are close enough to interact (1.5-2.0 Å), the O closest to the cluster transfers its spin density to the cluster while the O furthest away maintains a high-spin configuration. In the process, the O_2 bond length increases. At smaller distances from the cluster, the lowest energy configuration is one in which the O_2 molecule assumes side-on approach. The high-spin O then transfers its spin density to the cluster (or recombines with other high-spin O atoms to form $^3O_2$) and the $^1O_2$ molecule (or two low-spin O's) form(s) a peroxo-adsorbate between the two As atoms. The activation energy for the dissociation of the peroxo-adsorbate on the surface is 0.91 eV (87.8 kJ/mol).

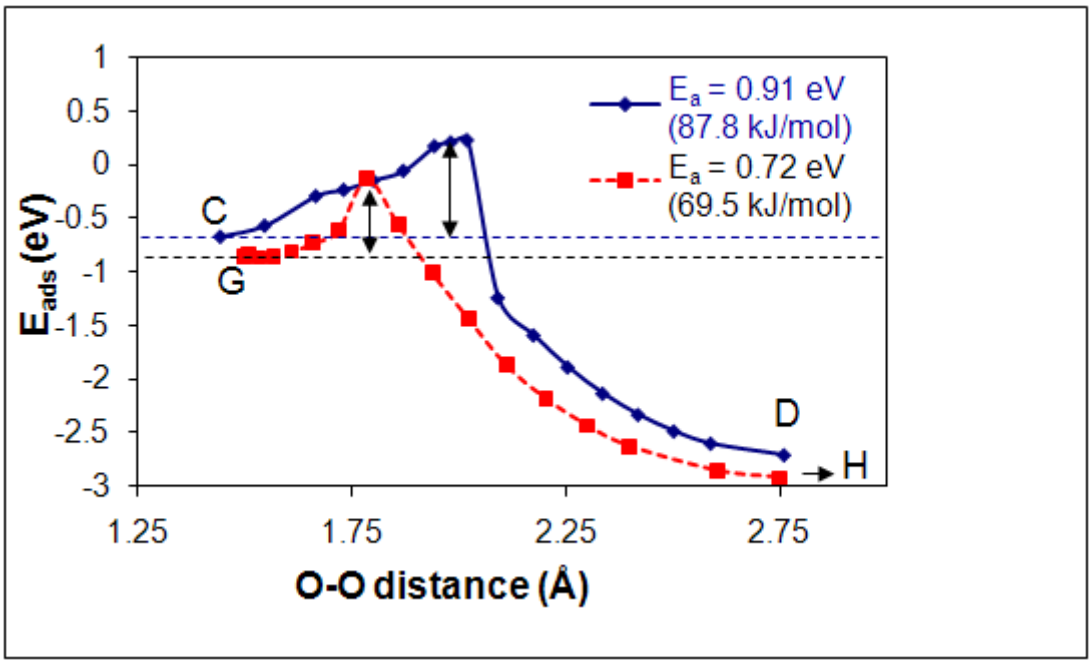

Figure 4.10. O_2 adsorption energy as a function of O-O distance. Points C and D correspond to O_2-As_4S_4 adsorption geometries shown in Figure 4.9c-d, and points G and H correspond to O_2-As_4S_4-$(OH)^-$geometries shown in Figure 4.9g-h. For diamonds, each point between points C and D represents an intermediate O_2-As_4S_4 geometry as the O-O distance increases. For squares, each point between points G and H represents an intermediate O_2-As_4S_4-$(OH)^-$ geometry. The energy barrier that must be overcome to break the O-O bond is 0.91 eV without co-adsorbed $(OH)^-$ and 0.72 eV with co-adsorbed $(OH)^-$.

Molecular O_2 + hydroxide ion adsorption

The same methodology that was used in the previous section was applied to the case for the co-adsorption of O_2 + $(OH)^-$ to As_4S_4. The ΔE_{ads} for each spin configuration is shown in Figure 4.11 as a function of the O_2 to As_4S_4-OH distance. At ~2.5 Å, $^3O_2$ begins to interact with As_4S_4, and at 2.0 Å, the difference between the configuration with $(OH)^-$ (Figure 4.9e) and without $(OH)^-$ (Figure 4.9a) is a significantly increased As-As distance in the former. At this O_2-As_4S_4 distance, $(OH)^-$ donates enough charge density to As that the As-As distance increases from 2.7 Å (w/o OH^-) to 3.8 Å (with OH^-). The increased distance between As-As allows $^3O_2$ to approach the cluster without having to overcome as high of an activation barrier as in the case without $(OH)^-$. Charge and spin are transferred back and forth from O_2 to As_4S_4 to an extent that at 1.8 Å, an approximate spin density of ~0.4 is transferred to the cluster and O_2 acquires a charge of -0.26 u.c. The low-spin configuration becomes the most favorable reaction path at a crossing point (~1.5 Å) which is further out from the cluster than is the case without $(OH)^-$. The low-spin peroxo-adsorbate configuration (Figure 4.9f-g) is different from the case without $(OH)^-$ in that both O atoms form bonds with the same As atom. In this case, the $(OH)^-$ pushes electron density through the cluster so that the two S atoms on the opposite side acquire ~0.4 u.c. more charge than the case without $(OH)^-$. The more negatively charged S atoms stabilize the O-O adsorbate on the single As. The sum of the Mulliken charge on the peroxo-adsorbate is -0.65 u.c. and the O-O bond length is 1.5 Å (versus -0.44 u.c. and 1.4 Å without $(OH)^-$).

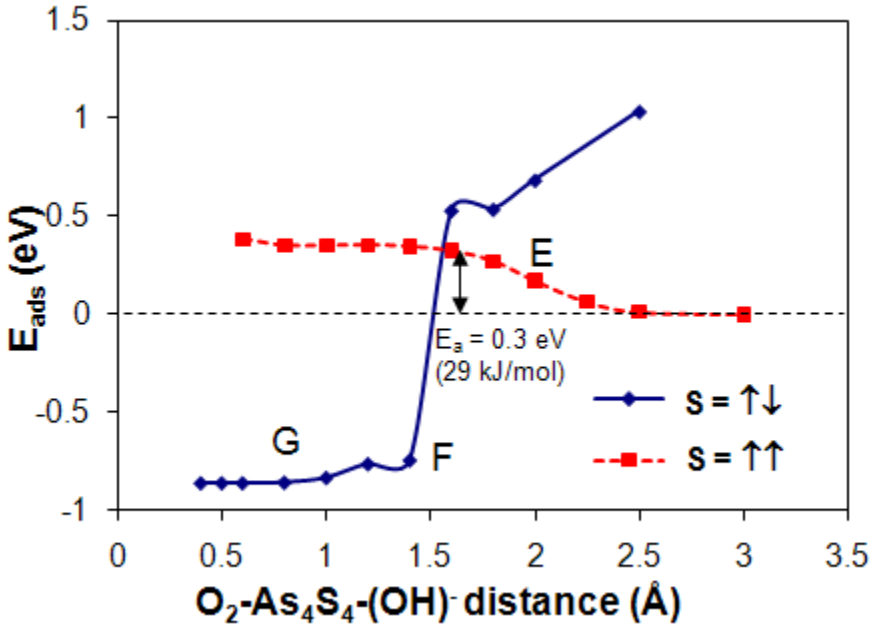

Figure 4.11. O_2 adsorption energy as a function of the O_2-[As_4S_4-$(OH)^-$] distance. Points E, F, and G correspond to O_2-As_4S_4-OH adsorption geometries shown in Figure 4.9e-g. The lowest energy state for an O_2 molecule approaching a As_4S_4 cluster (from infinite distance to 1.5 Å) is a triplet state (S = ↑↑). A singlet state (S = ↑↓) is lower in energy than the triplet state at O_2-[As_4S_4-$(OH)^-$] distances < 1.5 Å. An energy barrier of 0.3 eV (identified in the figure) must be overcome in order for $^3O_2$ to approach the surface and react.

The adsorbate configuration in Figure 4.9g is 2.1 eV higher in energy than the case with dissociated O_2 shown in Figure 4.9h and a step-by-step optimization of each intermediate configuration between the two reveals an activation energy barrier of 0.72 eV (69.5 kJ/mol) as shown in Figure 4.10.

The net result is that the initial oxidation of As_4S_4 by molecular $^3O_2$ involves two activation energy barriers, one associated with spin transfer from $^3O_2$ to the cluster and the other associated with the breaking of the O-O bond. Table 4.6 summarizes the activation energies for each activated process for both adsorption cases. It should be noted that the model for dissociative adsorption of O_2 on As_4S_4 does not take into account all of the degrees of freedom for both the molecule and the surface (including vibrational and rotational eigenstates). However, the ability for a co-adsorbate to modulate the activation energy barriers along a reaction path are shown for this case, and the activation energy barrier for oxidation with OH^- co-adsorption of 69.5 kJ/mol are within the error of the experimentally determined activation energy of ~64 ± 9.8 kJ/mol (25-40 °C, pH 8) for realgar oxidation (Lengke *et al.*, 2003). The empirical rate laws derived in their study indicate that the rates of both realgar and amorphous As_4S_4 increase with increasing pH. Our results indicate that surface hydroxyl groups have a catalytic effect on the activation energy for O_2 reduction on the surface of As_4S_4 as opposed to a simple exponential dependence on the concentration of $(OH)^-$ in solution.

Table 4.6. Activation energies for spin transfer and breaking of O-O bond for O_2 adsorption on As_4S_4 (with and without co-adsorbed OH^-).

	Spin transfer	**O-O bond dissociation**
$As_4S_4+O_2$	1.1 eV	0.91 eV
	(106.1 kJ/mol)	(87.8 kJ/mol)
$As_4S_4+O_2+(OH)^-$	0.3 eV	0.72 eV
	(29.0 kJ/mol)	(69.5 kJ/mol)

Implications

Energetics

Synergistic interactions between adsorbates on the As_4S_4 surface are shown to significantly affect the energetics and kinetics of the initial oxidation event on the surface. In terms of thermodynamics, quantum-mechanical calculations show that As_4S_4 is energetically more susceptible to oxidative attack when another anion is co-adsorbed with O on the surface. The adsorption energy gained by the synergistic interaction between O and the anion (*i.e.,* through the surface) is 5-40 kJ/mol, depending on the co-adsorbing anion. For every anion-O combination investigated in this study, the indirect interactions are significant enough to overcome direct electrostatic repulsive interactions between negatively charged co-adsorbates *and* energy losses due to changes in hydration that accompany co-adsorption. Highly-charged, highly-polarizable co-adsorbate anions, such as carbonate and sulfate, show the greatest influence on O adsorption as is expected based on their nucleophilicity. This description of the initial oxidation event on the surface sheds light on the molecular-scale processes that underlie the known pH- and pe-dependent solubility isotherm for realgar. For instance, consider the reaction for the oxidative dissolution of realgar in oxic-suboxic systems (Eqn. 5), and the resulting equation that describes the solubility isotherm (Eqn. 6) (from Sadiq, 1992):

$$AsS(realgar) + 8\ H_2O \leftrightarrow HAsO_4^{2-} + 11e^- + 15H^+ + SO_4^{2-} \quad logK^0 = -83.13 \qquad (5)$$

$$\log[HAsO_4^{2-}] = -83.12 + 11(pe + pH) + 4pH - \log[SO_4^{2-}] \qquad (6)$$

The reaction shown in (5) is an oversimplification of the multiple intermediate reactions and species involved in the transfer of 11 electrons; however, equation (6)

shows that realgar solubility increases as (pH + pe) increases. Despite the simulations in this study only describing the initial $2e^-$ oxidation event on the surface, the results are consistent with the known thermodynamics as shown in (Eqns. 5 and 6). In the most basic interpretation, the oxidative dissolution of realgar is described by evaluating the number of possible oxidation sites on terraces, steps, and kinks and multiplying each by its respective adsorption energy. As the pH increases, so does the surface concentration of hydroxyl groups [$(OH)^-$ concentration can be determined from surface charge vs. pH]. Thus, as pH goes up, there is an increased probability that an oxidation event will occur proximate to an adsorbed $(OH)^-$ where it is energetically enhanced by a proximity effect.

Oxidative dissolution is an important process in the weathering of realgar, but the formation of stable adsorbate-cluster configurations (*i.e.,* $(OH)^-$ and $(CO_3)^{-2}$) must also be considered as a possible non-oxidative dissolution mechanism under anaerobic conditions. Adsorbate-cluster configurations may acquire enough energy from hydration to overcome the lattice energy required to hold the cluster in place on the surface or, more likely, on a step or kink site where the cluster is undercoordinated. Indeed, aqueous clusters of other elements (e.g., FeS, ZnS, CuS) constitute a major fraction of the dissolved metal load in anoxic and oxic waters (Luther and Rickard, 2005). Kim *et al.* (2000) have shown that the release of As from groundwater was strongly related to the bicarbonate concentration in the leaching solution via the formation of stable arseno-carbonate complexes. The results suggest that the carbonization of arsenic sulfide minerals, including orpiment (As_2S_3) and realgar (As_4S_4) is an important process in leaching solid-bound arsenic into groundwater under anaerobic conditions. In the extreme case, it has been shown in this study that two $(OH)^-$ ions adsorbed to the same

cluster act to completely unravel the cluster, thus forming a linear molecule that is no longer structurally compatible with the realgar lattice. This behavior suggests that multiple dissolution mechanisms may be at work on the realgar surface depending on the pH, carbonate, and sulfate concentration.

Kinetics

Two energetic bottlenecks are identified that significantly affect the kinetics of the initial oxidation of As_4S_4 by O_2: i) the triplet (paramagnetic) to singlet (diamagnetic) spin transition, and ii) the dissociation of O_2. It is known that triplet oxygen, O_2, has sluggish kinetic reactivity based on fundamental spin selection rules. The triplet-to-singlet spin transition violates the law of conservation of angular spin momentum of the system. In biochemical systems, it is known that the formation of radicals is a result of spin selectivity rules (Minaev, 1982). In surface catalysis, the abstraction mechanism or spin catalysis is a process by which oxidation by $^3O_2$ can occur without violating spin selection rules (Binetti *et al.*, 2000; Komrowski *et al.*, 2001). For instance, the abstraction mechanism for an O_2 molecule involves O_2 approaching a surface end-on and the spin being shifted to the O that is further away from the surface. In this way, one O atom can adsorb in a singlet state, while the spin is efficiently carried away with the other O atom either being repelled back into the vacuum/aqueous solution or moved to a distant place at the surface where the spin can be accommodated. This has been shown with O_2 adsorbing to Al(111) surfaces (Behler *et al.*, 2005) and with O_2 adsorbing to UO_2 surfaces (Skomurski *et al.*, 2008). A second possibility is that spin is transferred to the surface. Becker *et al.* (2001) have shown that spin density can be accommodated, and in

effect, diluted on semiconducting surfaces by accommodation at corner and kink sites, vacancies or by adatoms nearby on the surface. The concept of spin being accommodated by an ad-atom on a surface is central to the developing field of spin catalysis (Buchachenko and Berdiinsky, 1996).

For As_4S_4, a significant activation energy barrier (1.1 eV, 106.1 kJ/mol) must be overcome in order for the $^3O_2$ orbitals to approach the surface, interact with the electronic surface states of the cluster, and transfer spin. Activation energy barriers due to spin transitions are rarely discussed in terms of the oxidation of mineral surfaces even though the magnitude of these barriers will significantly affect oxidation kinetics and may often be the rate-controlling step in oxidation reactions. A second activation energy barrier due to the breaking of the O-O bond and dissociation on the surface to form monatomic O is slightly lower in energy for realgar than the spin transition (0.91 eV; 87.8 kJ/mol). In a natural system, it would be nearly impossible to isolate the two activated processes considering thermal vibrations and the fact that the O-O bond begins lengthening as spin is partitioned between the O farthest from the cluster and the surface. In the case of As_4S_4, the spin transition would be the rate-limiting step (*i.e.,* the step with largest activation energy barrier).

Interestingly, the adsorption of $(OH)^-$ to a nearby surface site modulates each activated process by a different amount, and so it is necessary to treat each separately. The adsorption of $(OH)^-$ to surface As sites: i) stretches the As-As bond proximate to the O_2 adsorption site, and ii) modifies the surface charge potential of the As atoms that take part in bonding (*i.e.,* enhances the basicity of the neighboring As next to the $(OH)^-$ adsorption site). The elastic deformation and indirect interactions through the near

surface layers modifies the adsorption energy of molecular O_2 in that vicinity. In the process, it creates an alternative, low-energy reaction path for both the $^3O_2$ to $^1O_2$ spin transition and the dissociation of the O-O adsorbate that is based on the peroxo-adsorbate bonding to a single As atom instead of bridging two As atoms on the surface. The activation energy barrier for the spin transition and O_2 dissociation are 0.3 eV (29.0 kJ/mol) and 0.72 (69.5 kJ/mol), respectively. It is significant that in the case without a co-adsorbate the rate-limiting step is the paramagnetic to diamagnetic spin transition, but when $(OH)^-$ ion is present on the surface, the rate-limiting step becomes the dissociation of O_2 on the surface.

The energy barrier for both activated processes (with and without a co-adsorbed $(OH)^-$) are incorporated into the Boltzmann equation (probability $\propto \exp[-\Delta E_a/kT]$) to determine the probability that an impinging O_2 molecule will have enough energy to approach the surface, transfer its spin, and dissociate. ΔE_{act} is the activation energy barrier, k the Boltzmann constant, and T the temperature. This analysis yields a Boltzmann probability of 2.5×10^{-19} for the spin transition and 6.12×10^{-16} for the dissociation of the O-O adsorbate on the As_4S_4 surface at 298 K. When $(OH)^-$ is co-adsorbed proximate to the O_2 adsorption site the probabilities for the spin transition increase significantly to 8.5×10^{-6} (an increase of 13 orders of magnitude) and to 6.8×10^{-13} for the dissociation (an increase of three orders of magnitude).

A simple way of estimating rates involves determining the number of O_2 molecules colliding with the surface and multiplying this value by a Boltzmann factor (*i.e.*, the probability that the collision will result in an oxidation event). In this study, the rates for the spin transition and O_2 dissociation are treated individually for the cases with and

without a co-adsorbate. At 298 K, the root mean square speed of O_2 molecules is given by $c = (3RT/M)^{1/2}$ to be 483 m/s, where R is 8.314 $JK^{-1}mol^{-1}$ and M is the molar mass of O_2. The pressure (P) caused by N particles colliding with an area, A, at a velocity, v, is the force, F, or the total momentum transfer per second (Nmv). Thus $P = F/A = Nmv/A$. The partial pressure of O_2 above the As_4S_4 surface is determined from Henry's Law ($p_{O2} = [DO]/k$), where p_{O2} is the partial pressure of O_2 (atm.), [DO] is the concentration of dissolved oxygen in solution (M), and k is 1.3×10^{-3} $molL^{-1}atm^{-1}$. The model approach assumes a thin air gap at the mineral-water interface due to the demonstrated hydrophobicity of the surface. The theoretical rates are shown in Table 3.7 for a [DO] = 2.2×10^{-4} M (p_{O2} = 0.168 atm.) and T = 298 K. The theoretical rate of 7.4×10^{-10} $mol \cdot m^{-2} \cdot s^{-1}$ for O_2 dissociation with co-adsorbed $(OH)^-$ comes is of the same order as the experimental value of $\sim 1 \times 10^{-10}$ $mol \cdot m^{-2} \cdot s^{-1}$ ([DO] = 2.2×10^{-4} M; pH 8; T = 298 K) determined by Lengke and Tempel (2003). However, two assumptions must be noted in order to compare the theoretical rate obtained in this study with the experimental value. First, that the dissociation of O_2 is the rate-limiting step in oxidation mechanism. Lengke and Tempel suggest this is the case because of the magnitude of the activation energy and square root dependency of the rate law on the concentration of dissolved oxygen. However, they do not differentiate between the spin transition and the O_2 dissociation as described in this study. Our assumption is that the O_2 dissociation step is rate limiting due to it having more than two times the activation energy than the spin transition when $(OH)^-$ is co-adsorbed. Second, that a co-adsorbed $(OH)^-$ is

Table 4.7. Rates determined for the spin transition and the O_2 dissociation step for O_2 reacting with As_4S_4 (with and without OH^-) at 298 K. Assuming [DO] = 2.2×10^{-4} M (p_{o2} = 0.168 atm.).

	Boltzmann factor	**Theoretical rate ($mol \cdot m^{-2} \cdot s^{-1}$)**
Spin transition (As_4S_4-O_2)	2.5×10^{-19}	2.7×10^{-16}
O_2 dissociation (As_4S_4-O_2)	6.12×10^{-16}	6.6×10^{-13}
Spin transition (HO-As_4S_4-O_2)	8.5×10^{-6}	9.2×10^{-3}
O_2 dissociation (HO-As_4S_4-O_2)	6.8×10^{-13}	7.4×10^{-10}

proximate to every O_2 binding site, and that this condition reflects the actual concentration of hydroxyl groups on the realgar surface at pH 8. To our knowledge, there is no data in the literature describing the surface charge and coverage of surface hydroxyl groups on realgar as a function of pH. It is most likely that only a fraction of the surface As_4S_4 units will have adsorbed $(OH)^-$ ions and that the actual rate is a weighted average of the individual rates for $O_2 + As_4S_4$, $O_2 + As_4S_4$-$(OH)^-$(hydroxyl on the same cluster) as shown in Eqn. 7:

$$\text{Rate} = A[DO]^{1/2}\exp(-E_{a(noprox)}/RT) + (1-A)[DO]^{1/2}\exp(-E_{a(prox)}/RT) \qquad (7)$$

where *A* is the frequency factor relating to the probability that O_2 will react with an As_4S_4 cluster not containing a co-adsorbed $(OH)^-$. $E_{a(noprox)}$ and $E_{a(prox)}$ are the activation energies for the activated step that is rate limiting (*i.e.,* either the spin transition or O_2 dissociation) for the case of O_2 adsorbing without a co-adsorbed $(OH)^-$ and with $(OH)^-$, respectively. An additional term could be added to the rate expression in Eqn. 7 to account for modification of E_a by $(OH)^-$ ions on neighboring clusters.

The theoretical rates in this study are of the same order as experimental values and show a significant increase when oxidation occurs in the presence of a $(OH)^-$ co-adsorbate. The results suggest the possibility of a pH dependent rate constant for realgar that is not accounted for in current rate expressions. Further confirmation of this hypothesis comes from the Lengke and Tempel activation energies at pH 8 (25-40 °C); their value of 64 ± 10 kJ/mol is similar to the theoretical value (69 kJ/mol) calculated in this study based on the dissociation of O_2 on As_4S_4 with co-adsorbed $(OH)^-$. However, we suggest that the activation energy may exceed 100 kJ/mol at lower pH values based on our calculations. Thus, a simple exponential dependence on a species in the rate law

may not be accurate to describe the rate over wide pH, $p(CO_3^{2-})$, $p(SO_4^{2-})$, etc. ranges. This idea has broad implications for refining the rate laws for many sulfide minerals.

Similar processes may also influence oxidation of a host of arsenic sulfides with molecular structures similar to realgar. These include minerals with 3D arrangements of As_mS_n molecules held together by van der Waals forces such as alacranite (β-As_4S_4), dimorphite (As_4S_3), and uzonite (As_4S_5) as well as the light-induced degradation product, pararealgar, that forms thin films and spherules on the surface of realgar crystals. Arsenic sulfides with ribbon-like arrangements of As-S bonds such as orpiment (As_2S_3) may also be affected, and in this case, indirect interactions between adsorbates may extend to further separation distances due to the continuous edge sharing chains than run parallel to its prominent cleavage surface. Lengke and Tempel (2003) have shown that oxidation of amorphous arsenic sulfides (i.e phases of randomly-packed As_mS_n molecular units) and orpiment show a similar pH dependency to realgar suggesting that similar oxidation mechanisms may be at work on these surfaces.

The results in this study may also have implications for the oxidation mechanisms for sulfides like galena and pyrite. Lattice deformation and indirect interactions caused by adsorbates or surface defect sites is shown on galena surfaces. Rosso and Becker (2003) demonstrated that a single adsorbed O in a bridging configuration on the galena surface causes a local increase in the Pb-S bond length by ~0.6 Å, followed by an oscillatory deformation (or rumpling) of Pb-S bond lengths further away. It is not yet known if these deformations are capable of initiating lower activated energy paths for the O_2 spin transition or dissociation on the surface, however STM images of galena (100) crystal planes oxidized in air show the systematic growth of isolated patches of oxidation

products on the terrace surface (Laajalehto *et al.*, 1993; Becker and Hochella, 1996). The authors suggest that oxidation may be initiated by point defects or impurities on the surface.

Evidence also suggests that nonmicrobially-mediated pyrite oxidation rates increase as pH increases. Specifically, formation of surface carbonate complexes, identified by Evangelou *et al.* (1998), is suggested to promote abiotic oxidation of Fe(II) to Fe(III) followed by the subsequent oxidation of S on the pyrite surface by the regenerated Fe(III). This hypothesis is supported by Nicholson *et al.* (1990) who report an initial increase in pyrite oxidation kinetics in bicarbonate-buffered systems. In light of the results of this study, we suggest that adsorbates such as $(OH)^-$, $(CO_3)^{2-}$, or pH-independent species such as SO_4^{2-} may promote alternative, low-energy activated paths for the O_2 spin transition and/or O_2 dissociation, thus increasing the turnover of Fe(II) to Fe(III). It is also possible that high-spin Fe(II) or Fe(III) on the surface accommodates the spin of the approaching $^3O_2$, thus reducing the energy barrier for the spin transition. In this way, Fe may act as a true spin catalyst on the surface to increase the rate of oxidation by O_2 rather than or in addition to being the actual oxidant.

Conclusions

Quantum mechanical calculations show that at low pH (*i.e.,* no co-adsorbing hydroxide) the paramagnetic ($^3O_2$) to diamagnetic ($^1O_2$) spin transition is the rate-limiting step in the oxidation of As_4S_4. At high pH, the rate-limiting step is oxygen dissociation on the surface. The theoretically calculated oxidation rate ($\sim 10^{-10}$ mol·m^{-2}·s^{-1}) is of the

same order as empirically-derived rates from experiments at T = 298 K, pH = 8, and similar dissolved oxygen concentrations.

While this comparison is an indication that the type of calculations presented here identify the rate-limiting processes of realgar oxidation in different pH regimes, in other oxidation processes, other mechanisms, such as bulk diffusion in solution and through the Stern layer, and surface diffusion may be potential rate-limiting steps. Especially the first two of these are close to impossible to capture quantum mechanically and even stretch the limits of, e.g., molecular-dynamics simulations using classical force fields.

Activation energy barriers due to spin transitions may affect the kinetics of a host of common sulfide, arsenide, and oxide minerals. Understanding the extent of these activated processes, and how they may be attenuated by background electrolytes, has broad implications for refining empirically-derived rate expressions for oxidation, as well as for developing catalytic surfaces that alleviate the spin transition. In the former case, one could consider the role of Fe^{3+} as a spin transition modifier and not as the actual oxidant in the oxidation of pyrite, for instance. However, this latter case would have to be examined and much could be learned from biologically-mediated reactions to come up with new spin transition catalysts if oxidation is the desired reaction to be promoted.

Acknowledgments

Support for this research was received from National Science Foundation NIRT Grant EAR-0403732.

References

Ardizzone, S., Hoiland, H., Lagioni, C., and Sivieri, E. (1998) Pyridine and aniline adsorption from an apolar solvent: the role of the solid adsorbent. Journal of Electroanalytical Chemistry, 447, 17-23.

Babic, D., Rabii, S., and Bernholc, J. (1989) Structural and electronic-properties of arsenic chalcogenide molecules. Physical. Review, B. 39, 10831-10838.

Banerjee, A., Jensen, J. O., and Jensen, J. L. (2003) A theoretical study of As_4S_4: Bonding, vibrational analysis and infrared and Raman spectra. Journal of Molecular Structure –Theochem, 626, 63-75.

Becke, A. D. (1993) A new mixing of hartree fock and local density-functional theories. Journal of Chemical Physics, 98, 1372-1377.

Becker, U., Rosso, K. M., and Hochella, M. F. (2001) The proximity effect on semiconducting mineral surfaces: A new aspect of mineral surface reactivity and surface complexation theory? Geochimica et Cosmochimica. Acta, 65, 2641-2649.

Becker, U., and Hochella, M.F. (1996) The Calculation of STM images, STS spectra, and XPS peak shifts for galena: New tools for understanding mineral surface chemistry. Geochimica et Cosmochimica. Acta, 60, 2413-2426.

Behler, J., Delley, B., Lorenz, S., Reuter, K., and Scheffler, M. (2005) Dissociation of O_2 at Al(111): The role of spin selection rules. Physical Review Letters, 94, 4.

Binetti, M., Weisse, O., Hasselbrink, E., Komrowski, A. J., and Kummel, A. C., (2000) Abstractive chemisorptions of O_2 on Al(111). Faraday Discussions, 117, 313-320.

Bondzie, V. A., Parker, S. C., and Campbell, C. T. (1999) The kinetics of CO oxidation by adsorbed oxygen on well-defined gold particles on TiO_2(110). Catalysis Letters, 63, 143-151.

Buchachenko, A. L. and Berdinsky, V. L. (1996) Spin catalysis of chemical reactions. Journal of Physical Chemistry, 100, 18292-18299.

Cossi, M., Barone, V., Cammi, R., and Tomasi, J. (1996) *Ab initio* study of solvated molecules: A new implementation of the polarizable continuum model. Chemical Physics Letters, 255, 327-335.

De Giudici, G., Rossi, A., Fanfani, L., and Lattanzi, P. (2005) Mechanisms of galena dissolution in oxygen-saturated solutions: Evaluation of pH effect on apparent activation energies and mineral-water interface. Geochimica et Cosmochimica. Acta, 69, 2321-2331.

De Giudici, G. and Zuddas, P. (2001) In situ investigation of galena dissolution in oxygen saturated solution: Evolution of surface features and kinetic rate. Geochimica et Cosmochimica. Acta, 65, 1381-1389.

Eggleston, C. M., Ehrhardt, J. J., and Stumm, W. (1996) Surface structural controls on pyrite oxidation kinetics: An XPS-UPS, STM, and modeling study. American Mineralogist, 81, 1036-1056.

Eggleston, C. M. and Hochella, M. F. (1990) Scanning tunneling microscopy of sulfide surfaces. Geochimica et Cosmochimica. Acta, 54, 1511-1517.

Eggleston, C. M. and Hochella, M. F. (1991) Scanning tunneling microscopy of galena(100) surface oxidation and sorption of aqueous gold. Science, 254, 983-986.

Eggleston, C. M. and Hochella, M. F. (1993) Tunneling spectroscopy applied to PBS (001) surfaces – fresh surfaces, oxidation, and sorption of aqueous Au. American Mineralogist, 78, 877-883.

Eggleston, C. M. and Hochella, M. F. (1994) Atomic and electronic-structure of PBS (100) surfaces and chemisorptions-oxidation reactions. In Environmental Geochemistry of Sulfide Oxidation (Editors: C.N. Alpers and D.W. Blowes), American Chemical Society, Washington, DC. Pp. 201-222.

Evangelou, V. P., Seta, A. K., and Holt, A. (1998) Potential role of bicarbonate during pyrite oxidation. Environmental Science and Technology, 32, 2084-2091.

Frisch, M. J., Trucks, G. W., Schlegel, H. B., Scuseria, G. E., Robb, M. A., Cheeseman, J. R., Montgomery, J., J. A., Vreven, T., Kudin, K. N., Burant, J. C., Millam, J. M., Iyengar, S. S., Tomasi, J., Barone, V., Mennucci, B., Cossi, M., Scalmani, G.,

Rega, N., Petersson, G. A., Nakatsuji, H., Hada, M., Ehara, M., Toyota, K., Fukuda, R., Hasegawa, J., Ishida, M., Nakajima, T., Honda, Y., Kitao, O., Nakai, H., Klene, M., Li, X., Knox, J. E., Hratchian, H. P., Cross, J. B., Bakken, V., Adamo, C., Jaramillo, J., Gomperts, R., Stratmann, R. E., Yazyev, O., Austin, A. J., Cammi, R., Pomelli, C., Ochterski, J. W., Ayala, P. Y., Morokuma, K., Voth, G. A., Salvador, P., Dannenberg, J. J., Zakrzewski, V. G., Dapprich, S., Daniels, A. D., Strain, M. C., Farkas, O., Malick, D. K., Rabuck, A. D., Raghavachari, K., Foresman, J. B., Ortiz, J. V., Cui, Q., Baboul, A. G., Clifford, S., Cioslowski, J., Stefanov, B. B., Liu, G., Liashenko, A., Piskorz, P., Komaromi, I., Martin, R. L., Fox, D. J., Keith, T., Al-Laham, M. A., Peng, C. Y., Nanayakkara, A., Challacombe, M., Gill, P. M. W., Johnson, B., Chen, W., Wong, M. W., Gonzalez, C., and Pople, J. A. (2004) Gaussian Inc., Wallingford CT.

Gallegos, T. J., Hyun, S. P., and Hayes, K. F. (2007) Spectroscopic investigation of the uptake of arsenite from solution by synthetic mackinawite. Environmental Science and Technology, 41, 7781-7786.

Guevremont, J. M., Bebie, J., Elsetinow, A. R., Strongin, D. R., and Schoonen, M. A. A. (1998a) Reactivity of the (100) plane of pyrite in oxidizing gaseous and aqueous environments: Effects of surface imperfections. Environmental Science and Technology, 32, 3743-3748.

Guevremont, J. M., Elsetinow, A. R., Strongin, D. R., Bebie, J., and Schoonen, M. A. A. (1998b) Structure sensitivity of pyrite oxidation: Comparison of the (100) and (111) planes. American Mineralogist, 83, 1353-1356.

Guevremont, J. M., Strongin, D. R., and Schoonen, M. A. A. (1998c) Photoemission of adsorbed xenon, X-ray photoelectron spectroscopy, and temperature-programmed desorption studies of H_2O on FeS_2(100). Langmuir, 14, 1361-1366.

Guevremont, J. M., Strongin, D. R., and Schoonen, M. A. A. (1998d) Thermal chemistry of H_2S and H_2O on the (100) plane of pyrite: Unique reactivity of defect sites. American Mineralogist, 83, 1246-1255.

Guevremont, J. M., Strongin, D. R., and Schoonen, M. A. A. (1997) Effects of surface imperfections on the binding of CH_3OH and H_2O on FeS_2(100) using adsorbed Xe as a probe of mineral surface structure. Surface Science, 391, 109-124.

Huber, R., Sacher, M., Vollmann, A., Huber, H., and Rose, D. (2000) Respiration of arsenate and selenate by hyperthermophilic archaea. Systematic and Applied Microbiology, 23, 305-314.

Inskeep, W. P., McDermott, T. R., and Fendorf, S. (2002) Environmental Chemistry of Arsenic, Dekker, New York.

Kim, M. J., Nriagu, J., and Haack, S. (2000) Carbonate ions and arsenic dissolution by groundwater. Environmental Science and Technology, 34, 3094-3100.

Kinoshita, K. (1992) Electrochemical Oxygen Technology, Wiley, New York.

Komrowski, A. J., Sexton, J. Z., Kummel, A. C., Binetti, M., Weisse, O., and Hasselbrink, E. (2001) Oxygen abstraction from dioxygen on the Al(111) surface. Physical Review Letters, 87, 246103.

Laajalehto, K., Smart, R. S., Ralston, J., and Suoninen, E. (1993) STM and XPS investigation of reaction of galena in air. Applied Surface Science, 64, 29-39.

Lasaga, A. C. (1981) Rate laws of chemical reactions. In: Kinetics of Geochemical Processes (Editors: A.C. Lasaga and R.J. Kirkpatrick), Mineralogical Society of America, Washington, DC. pp. 1-68.

Lengke, M. F. and Tempel, R. N. (2005) Geochemical modeling of arsenic sulfide oxidation kinetics in a mining environment. Geochimica et Cosmochimica Acta, 69, 341-356.

Lengke, M. F. and Tempel, R. N. (2003) Natural realgar and amorphous AsS oxidation kinetics. Geochimica et Cosmochimica Acta, 67, 859-871.

Luther, G. W. and Rickard, D. T. (2005) Metal sulfide cluster complexes and their biogeochemical importance in the environment. Journal of Nanoparticle Research, 7, 389-407.

Makovicky, E. (2006) Crystal Structures of Sulfides and other Chalcogenides. In: Reviews in Mineralogy and Geochemistry 61 (Editor: J. J. Rosso), Mineralogical Society of America, Chantilly, VA. pp. 7-125.

Marcus, Y. (1994) A simple empirical-model describing the thermodynamics of hydration of ions of widely varying charges, sizes, and shapes. Biophysical Chemistry, 51, 111-127.

McKibben, M. A. and Barnes, H. L. (1986) Oxidation of pyrite in low-temperature acidic solutions - rate laws and surface textures. Geochimica et Cosmochimica Acta**,** 50, 1509-1520.

Minaev, B. F. (1982) The removal of spin-forbidden character in the reactions of triplet molecular-oxygen. Journal of Structural Chemistry, 23, 170-175.

Mullen, D. J. E. and Nowacki, W. (1972) Refinement of crystal-structures of realgar, AsS and orpiment, As_2S_3. Zeitschrift fur Kristallograhie, 136, 48-65.

Nicholson, R. V., Gillham, R. W., and Reardon, E. J. (1990) Pyrite oxidation in carbonate-buffered solution .2. rate control by oxide coatings. Geochimica et Cosmochimica Acta**,** 54, 395-402.

O'Day, P. A., Vlassopoulos, D., Root, R., and Rivera, N. (2004) The influence of sulfur and iron on dissolved arsenic concentrations in the shallow subsurface under changing redox conditions. Proceedings of the National Academy of Sciences of the United States of America, 101, 13703-13708.

Ozcan, O. (1992) Classification of minerals according to their critical surface-tension of wetting values. International Journal of Mineral Processing, 34, 191-204.

Perdew, J. P., Burke, K., and Ernzerhof, M. (1996) Generalized gradient approximation made simple. Physical Review Letters, 77, 3865-3868.

Pietro, W. J., Francl, M. M., Hehre, W. J., Defrees, D. J., Pople, J. A., and Binkley, J. S. (1982) Self-consistent molecular-orbital methods .24. supplemented small split-valence basis-sets for 2nd-row elements. Journal of the American Chemical Society, 104, 5039-5048.

Prabhakar, R., Siegbahn, P. E. M., Minaev, B. F., and Agren, H. (2004) Spin transition during H_2O_2 formation in the oxidative half-reaction of copper amine oxidases. Journal of Physical Chemistry B, 108, 13882-13892.

Rashin, A. A. and Honig, B. (1985) Reevaluation of the born model of ion hydration. Journal of Physical Chemistry, 89, 5588-5593.

Renock, D., Gallegos, T., Utsunomiya, S., Hayes, K.F., Ewing, R.C., and Becker, U. (2009) Chemical and structural characterization of As immobilization by nanoparticles of mackinawite (FeS_m). Chemical Geology, 268**,** 116-125.

Rosso, K. M. and Becker, U. (2003) Proximity effects on semiconducting mineral surfaces II: Distance dependence of indirect interactions. Geochimica et Cosmochimica Acta**,** 67, 941-953.

Rosso, K. M., Becker, U., and Hochella, M. F. (1999) Atomically resolved electronic structure of pyrite {100} surfaces: An experimental and theoretical investigation with implications for reactivity. American Mineralogist, 84, 1535-1548.

Sawyer, D. T. (1991) Oxygen Chemistry, Oxford University Press, New York.

Sadiq, M. (1992) Toxic Metal Chemistry in marine environments, Marcel Dekker, Inc., New York.

Schaftenaar, G. and Noordik, J.H. (2000) Molden: a pre- and post-processing program for molecular and electronic structures. Journal of Computer-Aided Molecular Design, 14, 123-134.

Segall, M. D., Lindan, P. J. D., Probert, M. J., Pickard, C. J., Hasnip, P. J., Clark, S. J., and Payne, M. C. (2002) First-principles simulation: ideas, illustrations and the CASTEP code. Journal of Physics: Condensed Matter, 14, 2717-2744.

Skomurski, F. N., Shuller, L. C., Ewing, R. C., and Becker, U. (2008) Corrosion of UO_2 and ThO_2: A quantum-mechanical investigation. Journal of Nuclear Materials, 375, 290-310.

Soma, M., Tanaka, A., Seyama, H., and Satake, K. (1994) Characterization of arsenic in lake-sediments by x-ray photoelectron-spectroscopy. Geochimica et Cosmochimica Acta**,** 58, 2743-2745.

Verhoef, R. W., Kelly, D., and Weinberg, W. H. (1995) Dissociative chemisorption of oxygen on Ir(110) as a function of surface coverage. Surface Science, 328, 1-20.

Wadt, W. R. and Hay, P. J. (1985) *Ab initio* effective core potentials for molecular calculations - potentials for main group elements Na to Bi. Journal of Chemical Physics, 82, 284-298.

Zhang, H. Z., Rustad, J. R., and Banfield, J. F. (2007) Interaction between water molecules and zinc sulfide nanoparticles studied by temperature-programmed desorption and molecular dynamics simulations. Journal of Physical Chemistry. A, 111, 5008-5014.

Chapter 4

A first principles study of coupled substitution in galena

Abstract

Coupled substitution is an important mechanism responsible for Ag enrichment in galena. Studies show that the concentration of Ag in galena will tend to equal the sum of the concentrations of Sb and Bi (Foord *et al.*, 1988). The thermodynamic mixing properties of the binary solid solution: Pb_2S_2-$AgSbS_2$, Pb_2S_2-$AgBiS_2$, and Pb_2S_2-$AgAsS_2$ have been investigated using quantum-mechanical and Monte-Carlo simulations. Quantum-mechanical methods were used to account for electron transfer between the substituting species. Total energies for different substitution configurations were used in Monte-Carlo calculations to derive the excess enthalpy of mixing (ΔH_{mix}), entropy of mixing (ΔS_{mix}), and free energy of mixing (ΔG_{mix}) at temperatures ranging from 200 ˚C to 1300 ˚C. ΔG_{mix} was used to calculate phase diagrams that can be compared with experiment. Electron transfer between Ag and either Sb, Bi, or As is shown to affect cation ordering in these systems. Quantum-mechanical simulations allow for the visualization of specific orbitals that are predominantly responsible for this electron transfer. Intermediates of the Pb_2S_2-$AgBiS_2$ solid solution tend to order into alternating

Ag-rich and Pb/Bi-rich layers parallel to [111]. Phase diagrams were determined for each solid solution series and Ag solubility limit of 5.2 mol% of $AgSbS_2$ was determined to be in reasonable agreement with experiments showing a value of ~5.5 mol% $AgSbS_2$.

Introduction

Coupled substitution is an important mechanism responsible for, e.g., noble-metal enrichment in sulfide minerals. The incorporation of Ag in galena (PbS) is one of the best examples of a coupled substitution mechanism in a sulfide. Experimental evidence suggests that only low concentrations of Ag^+ can be substituted into the PbS structure [a maximum of 0.4 mol% Ag_2S at 615 °C, and less at lower temperatures (Van Hook, 1960)] unless the substitution is coupled with the substitution of Sb^{3+} and/or Bi^{3+}. In the case of coupled substitution, concentrations of Ag as high as 9 wt% Ag in the 350-400 ˚C range have been reported (which would be 19.9 % cation substitution, provided the Ag would replace Pb cations in the structure rather than forming separate phases) (Foord and Shawe, 1989; Foord *et al.*, 1988). Specifically, studies show that the concentration of Ag in solid solution in PbS will tend to equal the sum of the molar concentrations of Sb and Bi (*i.e.,* bulk Ag:(Sb,Bi) molar ratio of ~1). However, it should be noted that in natural galena, these concentrations often include the presence of included Ag minerals such as diaphorite ($Pb_2Ag_3Sb_3S_8$), miargyrite ($AgSbS_2$), matildite ($AgBiS_2$), freiesledenite ($AgPbSbS_3$), and aramayoite ($Ag(Sb,Bi)S_2$) (Sharp and Buseck, 1993). Very little metallic Ag^0 can be accommodated into PbS (Costagliola *et al.*, 2003). Chutas *et al.* (2008) suggested that all of the Ag in high-temperature deposits may originate from a ternary assemblage between Pb_2S_2-$AgSbS_2$-$AgBiS_2$ that has a complete solid solution at

temperatures >441.7 °C. In this ternary system, phases with miargyrite and matildite compositions are isostructural with PbS at high temperatures. These high-temperature phases have been previously described (Graham, 1951). Hoda and Chang (1975) have shown the cubic-monoclinic transition temperature for $AgSbS_2$ to occur at a temperature of ~380 ˚C. XRD data suggest that PbS does not experience any changes in symmetry with the addition of significant fractions of $AgSbS_2$ and $AgBiS_2$ (Chutas *et al.*, 2008). As a consequence, phase assemblages and textures commonly observed in Ag-bearing ore deposits (formed at high temperature) and containing considerable quantities of PbS may be due to retrograde, solid-state reactions that redistribute Ag via exsolution during cooling from an original solid solution, *i.e.,* a homogeneous crystal.

The evolution of a hydrothermal fluid (*i.e.,* the increase of both concentrations of Ag and Sb in solution) has been offered as a possible explanation for Ag enrichment and correlations between Ag and Sb in some deposits, and undoubtedly plays a role in ore-forming environments (Hackbarth and Peterson, 1984). However, little is known about the extent of the electronic and crystallographic controls that play a role in the Ag and Sb/Bi correlations observed in PbS. For example, are there structural or electronic constraints that promote or hinder the formation of Ag-As couples over Ag-Sb ones? Thus, understanding the atomic scale mechanism underpinning the coupled substitution reactions is important to understanding the distribution of precious metal in these systems.

Galena has the well-known rocksalt structure with both S- and Pb-forming fcc sublattices and with both atoms being in octahedral coordination (space group *Fm3m*). Generally, the coupled substitution mechanism in galena is explained by Ag and Sb

(and/or Bi) substituting for two Pb atoms at or above temperatures of ore formation (T > 240 °C). Charge balance is achieved by the mechanism [$Ag^{+1} + (Sb,Bi)^{3+} = 2Pb^{2+}$] and this allows higher concentrations of Ag to be incorporated relative to a single substitution event [$2Ag^{+} = Pb^{2+}$]. In the latter case, the lower concentrations are commonly explained by the unfavorable energetics of Ag substitution into an interstitial site within the galena structure. Ionic charge and size (ionic radius) are often invoked to explain structural changes and thermodynamics of substitutional processes. For example, Madelung energies can be calculated accurately for ionic solids based simply on the geometric arrangement of the ions, but these energies are not a good representation of the lattice energy for materials with increasing covalent and metallic bond character. Galena is a small-band-gap semiconductor with a band gap on the order 0.3-0.5 eV (Tossell and Vaughan, 1987), and is held together by Pb-S bonds that are semi-metallic. Galena is an intrinsic semiconductor (*i.e.,* the thermal excitation of valence band electrons in the conduction band of a defect free PbS crystal), but often contains impurities or defects in natural samples that alter the position of the Fermi level in the band gap and give rise to extrinsic semiconduction (*i.e.,* conduction caused by electrons or holes from the impurities). Thus, galena may be either n- or p-type depending on the types of impurities and defects present (Pridmore and Shuey, 1976). Natural samples are usually n-type due to formation conditions that favor sulfur vacancies (donors) over lead vacancies (acceptors). N-type behavior may also be caused by substitutional donor impurities such as Sb and Bi, whereas p-type behavior can result from high concentrations of Ag, a substitutional acceptor (Bloem, 1956). From the viewpoint of defect chemistry, the Ag:(Sb,Bi) molar ratio of ~1 is suggested to be due to the association of acceptor Ag with

donor Sb and/or Bi (*i.e.,* donors and acceptors increase each other's solubility in galena) (Kroger, 1974). In effect, each impurity decreases the incorporation energy of the other via charge transfer (or redox) interactions between the two. Examples of mutual increases in solubility between donor and acceptor impurities are numerous. For instance, the mutual increase in solubility is so large for coupled substitution of Cu (acceptor) and Ga (donor) in ZnS that a complete solid solution exists between the two isostructural end members (*i.e.,* Zn_2S_2-$CuGaS_2$). The same can be said for a large number of compounds, ABX_2, having the zincblende or chalcopyrite ($CuFeS_2$) structure. $AgSbS_2$, $AgBiS_2$, $AgSbSe_2$, $AgSbTe_2$, and $AgBiTe_2$ have structures similar to PbTe and PbS and also have a wide range of solid solubilities between each pairing of end members. Another analog in the materials science literature would be group III-V semiconductors, where, a group III (e.g., Ga) and group V (e.g., As) replace two Si atoms with four valence electrons to control the electronic properties of the compound.

To the author's knowledge, there is little information in the literature as to how acceptor–donor interactions between Ag and (Sb and Bi) affect their incorporation into galena and thus, the thermodynamic mixing properties of their respective solid solutions. Prior to this study, the solubility of $AgAsS_2$ in galena appears to be completely unknown. In addition, it has to be noted that interactions between noble metals and group 15 cations have often been treated as if the +1 and +3 cations are located on Pb lattice sites with just Coulomb interactions between them. However, atomic relaxations, beyond-Coulomb energy exchange, and the covalent character of orbitals that encompass both cations of the coupled pair have not been investigated so far. Therefore, in this study, first-principles (*ab initio*) methods were applied to determine the structural changes,

electronics, and ultimately the energetics of Ag, Au, and Cu (*i.e.,* substitutional acceptors) substitution into bulk galena, either as a single substitution event or as a coupled substitution with a donor atom (*i.e.,* Group 15 elements: As, Sb, or Bi). Substitution energies corresponding to different geometric configurations of donor-acceptor atoms were determined. In addition, the energetics of coupled substitution of $Ag^{+} + Sb^{3+}$, $Ag^{+} + Bi^{3+}$, and $Ag^{+} + As^{3+}$ was calculated for multiple compositions and configurations within three compositional series: $AgSbS_2$-Pb_2S_2, $AgBiS_2$-Pb_2S_2, and $AgAsS_2$-Pb_2S_2. In order to derive meaningful thermodynamic results for these solid solutions, Monte-Carlo simulations were performed on supercells of sufficient size to capture all of the possible cationic configurations. Excess enthalpies of mixing (ΔH_{mix}) were determined, and subsequently, the Gibbs free energy (ΔG_{mix}) and entropy (ΔS_{mix}) of mixing were calculated using a Bogoliubov integration scheme. Based on the thermodynamic data at equilibrium, T-X_{AgSb}, T-X_{AgBi}, and T-X_{AgAs} phase diagrams for all binaries are presented and the simulation results compared to available experimental and analytical data.

Computational Methods

A three-step process was used to calculate the thermodynamic properties of $AgSbS_2$-Pb_2S_2, $AgBiS_2$-Pb_2S_2, and $AgAsS_2$-Pb_2S_2 solid solutions at elevated temperatures: 1) a quantum-mechanical (q.m.) first-principles approach was used to calculate the total energy for different cation-cation configurations and compositions (and ΔE_{mix} by relating the energy of an intermediate to the energy of a linear mix of the end members), 2) cation-cation interaction parameters (or *J*'s) were determined by fitting the ΔE_{mix}

determined from q.m. runs, and 3) the excess enthalpy of mixing (ΔH_{mix}) was determined by using the interaction parameters in combination with a Monte-Carlo simulation to evaluate the energy of millions of possible configurations as a function of composition and temperature. Thermodynamic integration is then used to determine the excess free energy and entropy of mixing (ΔG_{mix}, ΔS_{mix}). The general methodology used in this study is described by Bosenik *et al.* (2001), Dove (2001), and Becker *et al.* (2000), but the specifics closely follow the method of Reich and Becker (2006) in their study of the thermodynamic mixing properties of arsenian pyrite and marcasite. However, as further detailed below, modifications to the Monte-Carlo method had to be made to account for the swapping of unequally-charged species in a coupled substitution system and the presence of heterocationic interactions in the non-galena end member.

First principles total-energy calculations

A quantum-mechanical approach was required in this study to account for the possibility that electron transfer between substituting atoms may affect the total energy. The total energy of each configuration was calculated using a density functional theory-based (DFT, Hohenberg and Kohn, 1964) quantum mechanical code, CASTEP (CAmbridge Serial Total Energy Package), which is part of the Materials Studio Modeling package (version 4.4) (Segall *et al.,* 2002). A generalized-gradient approximation (GGA) with exchange correlation approximated by the Perdew-Burke-Ernzerhof (PBE) functional (Perdew *et al.*, 1996) was used to capture the interaction of valence electrons between different atoms. Ultrasoft pseudopotentials were used to approximate the effect of the core electrons on the energies of the valence electrons

(Payne *et al.*, 1992). Planewaves were employed as basis functions to model the wavefunctions that describe the distribution of electrons in the system. A k-point grid spacing of 0.04 1/Å and a planewave cutoff energy of 400 eV were used in the calculations. A 1×1×2 Pb_8S_8 supercell (8 exchangeable cation sites) of the conventional galena unit cell was used for all q.m. calculations. Full geometry optimizations without symmetry constraints were performed to determine total energies. In some cases, atoms had to be manually displaced initially if the initial position was a saddle point, in order for full relaxation to take place.

Calculation of cation-cation interaction parameters

The calculation of cation-cation interaction parameters (*J*'s) allow for the total energies of millions of configurations in a large supercell to be evaluated, a process that would be unwieldy using quantum mechanics alone. The total energy for a solid solution composition at a specific configuration can be expressed in a general way by Eqn. 1:

$$E = E^0(x) + \sum_{i,l} n_l^i J_l^i \tag{1}$$

$$^kE_{qm} \xleftarrow{=} E^0_{m\arg}(^kx) + \sum_{i,l} {}^k n_l^i J_l^i \tag{1a}$$

where E is the total energy of the system, $E_0(x)$ is a composition(x)-dependent energy constant that describes the configuration-independent energy of the system for a given composition x, i is a heterocationic interaction type (e.g., i=1: first (I), i=2: second (II), i=3: third (III) nearest neighbor) and l defines the substitution couple: Ag-Pb (l=1), Sb-Pb (l=2), or Ag-Sb (l=3). Thus, n_l^i is the number of i-type heterocationic interactions connecting a specific couple l, and J is the ith interaction parameter for a particular

substitution couple *l*. The different interaction types, *i*, depends on the geometric relations between the exchangeable cations and correspond to the three different cation sites relative to Ag in Figure 5.1. The three interaction types are labeled I, II, and III in Figure 5.1 and will be referenced as such for the remainder of the text. Thus, J_l^i is an energy term associated with the sole exchange between two substituting atoms (e.g. Ag-Sb in Eqn. 2) in a specific configuration:

$$J^i_{Ag-Sb} = E^i_{Ag-Sb} - \frac{1}{2}\left(E^i_{Ag-Ag} + E^i_{Sb-Sb}\right) \tag{2}$$

J values are determined by fitting the energies using the *J* terminology (right side in Eqns. 1 and 1a) for a given configuration *k* to the quantum-mechanically obtained excess energies for multiple configurations in each solid-solution series. The configuration-independent part of the excess energies, $E^0(x)$, in Eqn. 1a is approximated by a two-parameter Margules function [$E^0_{marg}(x) = x(1-x)(Ax+B(1-x))$] simultaneously with the *J's*. The Margules function describes the asymmetry of the spread of excess energies along the binary and represents the composition-dependent energy constant (E_0 in Eqn. 1). In other words, it represents the case where all J^i*'s* equal zero. In practice, the fit in Eqn. 1a is performed in such a way that for a given configuration *k,* the number of interactions n_l^i are determined (specific for that configuration) and the configuration-independent Margules parameters, A and B, and the *J*'s are determined such that the sum of squares of the deviations from the q.m. energies, ${}^mE_{qm}$ is minimal. For a given interaction type, *i*, a positive *J* value indicates that homocationic interactions (e.g., Ag-Ag, Sb-Sb, Pb-Pb) are more energetically favorable, while a negative *J* means that the heterocationic interactions (e.g., Ag-Pb, Sb-Pb, Ag-Sb) are favored.

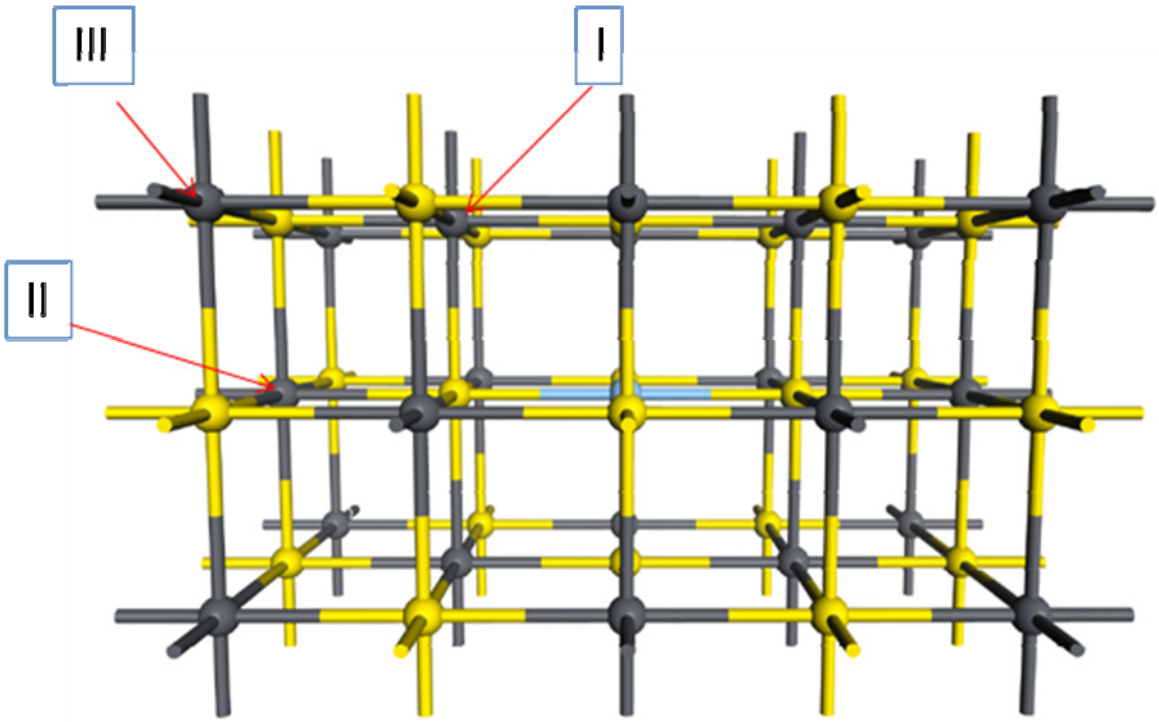

Interactions	Distance (Å)
I	4.3
II	6.0
III	7.4

Figure 5.1. Schematic of the 2x2x1 galena supercell showing the different structural relations (interaction types) between substitution couples (e.g., Ag, Sb).

In a binary system, both endmember energies are automatically zero because the number of heterocationic interactions n_l^i is zero. However, a modification to Eqn. 1 is required for systems involving coupled substitutions due to an endmember necessarily having a nonzero number of heteroatomic interactions (*i.e.,* between the substitution couples or, e.g., Ag-Sb interactions in the endmember with miargyrite composition). Since the energy of the second endmember in the formalism of Eqn. 1 would have the energy $\sum_{i,l} m_l^i J_l^i$ (E^0 is automatically zero for $x = 1$, m_l^i is the number of interactions in the second endmember), a linear proportion of this amount is subtracted in the new formalism for coupled substitution. In this case, a linear correction is subtracted from the excess energy term to account for the heteroatomic interactions of the end member. Thus, Eqn. 1 turns into the respective Eqn. 3:

$$E = E^0(x) + \sum_{i,l} n_l^i J_l^i - x\sum_{i,l} m_l^i J_l^i \qquad (3)$$

and the fit is being performed using Eqn. 3a (instead of 1a):

$${}^k E_{qm} \xleftarrow{=} E^0_{m\arg}({}^k x) + \sum_{i,l} {}^k n_l^i J_l^i - x\sum_{i,l} m_l^i J_l^i \qquad (3a)$$

where x is the molar fraction of the second end member and m^i is the number of i-type heteroatomic interactions present in the non-galena end member. The calculated J's for each solid solution series are shown in Table 5.1.

Monte-Carlo simulation: determination of thermodynamic properties

Interaction parameters J^i_l can be used to calculate the lattice energies for millions of different cationic configurations in each solid solution series. This is accomplished by using a Monte-Carlo simulation that randomly swaps the positions of two

Table 5.1. Fitted interaction parameters (J_i) in kJ/(mol interaction) for the three possible interaction types in the Pb_2S_2-$AgSbS_2$, Pb_2S_2-$AgBiS_2$, and Pb_2S_2-$AgAsS_2$ solid solutions.

Interaction parameters J_i ***(kJ/mol interactions)***	**interaction**		
	I	**II**	**III**
Pb_2S_2-$AgSbS_2$			
$J_{Pb\text{-}Ag}$	0.089	-0.102	-0.0007
$J_{Pb\text{-}Sb}$	-0.197	0.266	0.028
$J_{Ag\text{-}Sb}$	-0.148	0.114	0.099
Pb_2S_2-$AgBiS_2$			
$J_{Pb\text{-}Ag}$	-0.185	-1.03	-0.210
$J_{Pb\text{-}Bi}$	-0.041	0.632	0.181
$J_{Ag\text{-}Bi}$	-0.357	-0.552	0.000
Pb_2S_2-$AgAsS_2$			
$J_{Pb\text{-}Ag}$	0.122	-0.275	-0.0017
$J_{Pb\text{-}As}$	-0.250	0.197	-0.016
$J_{Ag\text{-}As}$	-0.191	-0.302	0.000

exchangeable cations in a supercell (*i.e.,* 2048 cations) and determines the associated change in energy ΔE for each swap (Becker *et al.*, 2000; Myers, 1998). If the energy for new configuration (*i.e.,* after the swap) is lower than the energy of the previous configuration (*i.e.,* negative or zero), then the swap is accepted, and the lattice energy for the new configuration is determined by $\Sigma(n^i J^i)$ as described in the previous section. If the change in energy is positive, then the probability (P) that the swap will be accepted is based on a Boltzmann distribution (Eqn. 4):

$$P = e^{\left(-\frac{\Delta E_{swap}}{k_B T}\right)} \tag{4}$$

where k_B is 1.3807 × 10^{-23} J/K and T is temperature (K). In this case, the swap is accepted if P is greater than a random number between 0 and 1 (random numbers are regenerated for each swap attempt). This acceptance procedure converges the set of configurations to the Boltzmann distribution (Metropolis *et al.*, 1953). The simulation allows 100,000 successful swaps to occur at every temperature and configuration to equilibrate the system. After the equilibrium step, the enthalpies are averaged over the next 100,000 successful swaps at every temperature. A complication to the Monte-Carlo swapping procedure arises when cations of unequal charge swap for one another in the large supercell (e.g. $Ag^{+1} \leftrightarrow Sb^{+3}$). The large supercell in this study consists of 256 of the original 2×1×1 unit cells (designated as the "small" unit cell), *i.e.,* 2048 cations altogether. Swapping two cations of unequal charge from anywhere within the large supercell can result in the build-up of local non-neutral charges, *i.e.,* the formation of non-neutral "small" unit cells. Since the original q.m. calculations, from which interaction parameters were derived, were based on charge-neutral conditions at a local

scale due to the small q.m. unit cell, any Monte-Carlo simulation resulting in non-neutral domains would increase the Coulomb energy of the system. Thus, swaps that result in a non-neutral "small" unit cell would result in a gain in energy of $\sum_i const \times chg_i^2$ where an empirically-derived *const* of 5 eV was used, chg_i is the charge of an individual "small" unit cell, and this Coulomb term is summed over the entire large 2048-cation cell. The value of 5 eV for *const* is ~2× the difference in energy for single substitution of Ag into Pb_8S_8 compared to coupled substitution (obtained from q.m.). In addition, swaps are only allowed between cations that are in nearest- and next-nearest neighbor positions.

The configurational entropy and free energy of mixing (ΔS_{mix} and ΔG_{mix}) were then calculated by thermodynamic integration using a Bogoliubov integration scheme (Yeomans, 1992; Myers, 1998). It should be noted that the entropy of mixing is composed of two major contributions, configurational entropy and vibrational entropy. The latter is not considered in this study. However, estimates for other systems have shown that for similar temperatures the vibrational entropy can lower ΔG_{mix} by up to 10% (Pollok and Becker, 2002). However, this effect has only a small influence on the phase diagram, such as the positions of the miscibility gaps. The former is associated with the distribution of elements within the crystal structure. The configurational entropy ($S_{conf)}$ is determined from the Boltzmann relation (Eqn. 5):

$$S_{conf} = k_B \ln W \tag{5}$$

where W is the number of possible arrangements of atoms in the crystal structure. For a solid solution with only two exchangeable cations, such as in magnesian calcite, or its

ordered form dolomite, $CaMg(CO_3)_2$, the so-called point entropy, ΔS_{mix}, of the disordered case is defined by Eqn. 6 for components A and B:

$$\Delta S_{excess} = -R(x_A \ln x_A + (1 - x_A) \ln(1 - x_A)) \quad (6)$$

However, the solid solution in this study contains three exchangeable cations, and must therefore be treated by the three component entropy term shown in Eqn. 7 for components A, B, and C (where A = Ag; B =As,Sb, or Bi; C = Pb):

$$\Delta S_{excess} = -R(x_A \ln x_A + x_B \ln x_B + x_C \ln x_C) \quad (7)$$

Since $x_A = x_B$ in this system, $x_c = 1\text{-}2x_A$, and therefore Eqn. 7 can be written as:

$$\Delta S_{excess} = -R(2x_A \ln x_A + (1 - 2x_A) \ln(1 - 2x_A)) \quad (7a)$$

The maximum configurational entropy for a three component system occurs at $x_{AgM} = x_{Ag} + x_M = 0.66$ (where M=As, Sb, or Bi). Another characteristic of the three-component entropy term is a non-zero, positive entropy value at the non-galena end member due to the possibility for multiple arrangements of Ag and either As, Sb, and Bi. Only if the system would fully order would the configurational entropy go to zero.

Results

Determination of coupled substitution energies, ΔE_{sub}

Before the thermodynamics of the entire solid solutions can be evaluated, it is instructive to describe the energetics, structural relaxations, and changes in the electronic structure of single substitution events. The optimized geometries and associated total energies were determined for the coupled substitutions of Cu^{+}+As^{3+}, Cu^{+}+Sb^{3+}, Cu^{+1}+Bi^{3+}, Ag^{+}+As^{3+}, Ag^{+}+Sb^{3+}, Ag^{+}+Bi^{3+}, Au^{+}+As^{3+}, Au^{+}+Sb^{3+}, and Au^{+}+Bi^{3+} for

$2Pb^{2+}$ atoms in Pb_8S_8 (oxidation states are included to show that the neutrality condition is obeyed in each case). If one out of eight Pb atoms is replaced by either Ag, Au, or Cu, then the molar fraction of substituted metal is 12.5 %, which translates into weight % of substituted metal of 6 wt% for Ag, 11 wt% for Au, and 4 wt% for Cu, and based on the 2×1×1 unit cell (Pb_8S_8). For each composition, total energies were determined for the 3 different configurations (*i.e.,* interactions I, II, and III) depending on the structural relations and distance between the two substituting cations such as previously described in Figure 5.1. Coupled substitution energies (ΔE_{sub}) were determined for simple, stoichiometric reactions involving Pb_8S_8 as a reactant phase and different source phases for the Cu, Ag, Au, As, Sb, and Bi. The products include the substituted Pb_8S_8 (as a sink for the substituting atoms) and other phases (when necessary) to maintain stoichiometry. The total energy for each product and reactant phase (*i.e.,* source and sink phases) was determined from the quantum mechanical runs and ΔE_{sub} was calculated using equation (8) for the following reactions (Eqns.9-29):

$$\Delta E_{sub} = \sum E_{products} - E_{reac\,tants} \quad (8)$$

Reactants		Products	ΔE_{sub} (eV)	
Coupled substitution with 1 sulfosalt source phase for both Ag and (As, Sb, Bi):				
¾ Pb_8S_8 + 1/6 $Ag_6As_6S_{12}$ (trechmannite)	→	Pb_6AgAsS_8	I: 0.31 II: 0.44 III: 0.58	(9)
¾ Pb_8S_8 + 1/6$Ag_4Sb_4S_8$ (miargyrite)	→	Pb_6AgSbS_8	I: 0.33 II: 0.50 III: 0.67	(10)
¾ Pb_8S_8 + 1/6$Ag_3Bi_3S_6$ (matildite)	→	Pb_6AgBiS_8	I: 0.44 II: 0.40 III: 0.56	(11)
Coupled substitution with 2 different source phases for Ag and (As, Sb, Bi):				
¾ Pb_8S_8 + 1/8Ag_8S_4 + 1/8As_8S_{12}	→	Pb_6AgAsS_8	I: 0.28	(12)

(acanthite) (orpiment) II: 0.41
III: 0.55

¾ Pb_8S_8 + 1/8Ag_8S_4 + 1/8Sb_8S_{12} → Pb_6AgSbS_8 I: 0.30 (13)
(acanthite) (stibnite) II: 0.47
III: 0.63

¾ Pb_8S_8 + 1/8Ag_8S_4 + 1/8Bi_8S_{12} → Pb_6AgBiS_8 I: 0.45 (14)
(acanthite) (bismuthinite) II: 0.41
III: 0.58

Coupled substitution with 2 different source phases for Au and (As, Sb, Bi):

¾ Pb_8S_8 + 1/8$Ag_{24}Au_8S_{16}$ + 1/6 $Ag_6As_6S_{12}$ → Pb_6AuAsS_8 + 1/2Ag_8S_4 I: 0.47 (15)
(uytenbogaardite) (trechmannite) (acanthite) II: 0.60
III: 0.67

¾ Pb_8S_8 + 1/8$Ag_{24}Au_8S_{16}$ + 1/4 $Ag_4Sb_4S_8$ → Pb_6AuSbS_8 + 1/2Ag_8S_4 I: 0.42 (16)
(uytenbogaardite) (miargyrite) (acanthite) II: 0.39
III: 0.58

¾ Pb_8S_8 + 1/8$Ag_{24}Au_8S_{16}$ + 1/3 $Ag_3Bi_3S_6$ → Pb_6AuBiS_8 + 1/2Ag_8S_4 I: 0.66 (17)
(uytenbogaardite) (matildite) (acanthite) II: 0.67
III: 0.64

Coupled substitution with 2 different source phases for Au and (As, Sb, Bi):

¾ Pb_8S_8 + 1/4Au_4S_2 + 1/8As_8S_{12} → Pb_6AuAsS_8 I: 0.63 (18)
(synthetic) (orpiment) II: 0.76
III: 0.83

¾ Pb_8S_8 + 1/4Au_4S_2 + 1/8Sb_8S_{12} → Pb_6AuSbS_8 I: 0.58 (19)
(synthetic) (stibnite) II: 0.56
III: 0.74

¾ Pb_8S_8 + 1/4Au_4S_2 + 1/8Bi_8S_{12} → Pb_6AuBiS_8 I: 0.86 (20)
(synthetic) (bismuthinite) II: 0.87
III: 0.84

Coupled substitution with 1 sulfosalt source phase for both Cu and (As, Sb, Bi):

¾ Pb_8S_8 + ¼ $Cu_4As_4S_8$ → Pb_6CuAsS_8 I: 0.46 (21)
(emplectite) II: 0.50
III:0.61

¾ Pb_8S_8 + ¼ $Cu_4Sb_4S_8$ → Pb_6CuSbS_8 I: 0.50 (22)
(chalcostibite) II: 0.49
III:0.63

¾ Pb_8S_8 + ¼ $Cu_4Bi_4S_8$ → Pb_6CuBiS_8 I: 0.54 (23)
(synthetic) II: 0.48
III:0.62

Coupled substitution with 2 different source phases for Cu and (As, Sb, Bi):

¾ Pb_8S_8 + 1/8 Cu_8S_4 + 1/8 As_8S_{12} → Pb_6CuAsS_8 I: 0.34 (24)

(chalcocite) (orpiment)			II: 0.37 III:0.49	
¾ Pb_8S_8 + 1/8 Cu_8S_4 + 1/8 Sb_8S_{12} (chalcocite) (stibnite)	→	Pb_6CuSbS_8	I: 0.35 II: 0.37 III:0.49	(25)
¾ Pb_8S_8 + 1/8 Cu_8S_4 + 1/8 Bi_8S_{12} (chalcocite) (bismuthinite)	→	Pb_6CuBiS_8	I: 0.48 II: 0.42 III:0.56	(26)
Single substitution (Ag, Au, Cu)				
7 Pb_8S_8 + Ag_8S_4 + Fe_4S_8 (acanthite) (pyrite)	→	8 Pb_7AgS_8 + 2 Fe_2S_2 (mackinawite)	2.3	(27)
7 Pb_8S_8 + 2 Au_4S_2 + Fe_4S_8 (synthetic) (pyrite)	→	8 Pb_7AuS_8 + 2 Fe_2S_2 (mackinawite)	2.9	(28)
7 Pb_8S_8 + Cu_8S_4 + Fe_4S_8 (chalcocite) (pyrite)	→	8 Pb_7CuS_8 + 2 Fe_2S_2 (mackinawite)	2.2	(29)

Ag coupled substitution:

In the case of coupled substitutions involving Ag (*i.e.,* reactions: 9-14), the source phase of Ag and (As,Sb,Bi) is a sulfosalt containing both elements in its structure. Hexagonal trechmannite ($AgAsS_2$), monoclinic miargyrite ($AgSbS_2$), and trigonal matildite ($AgBiS_2$) are used as sources for Ag^++As^{3+}, Ag^++Sb^{3+}, and Ag^++Bi^{3+} substitutions, respectively. Reactions (12-14) involve two independent sources for Ag and either As, Sb, or Bi. Monoclinic acanthite (Ag_8S_4), monoclinic orpiment (As_8S_{12}), orthorhombic stibnite (Sb_8S_{12}), and orthorhombic bismuthinite (Bi_8S_{12}) are used as sources for Ag, As, Sb, and Bi, respectively. The sulfosalts and sulfides chosen in this series are all phases that are known to appear in trace amounts in galena. ΔE_{sub} was determined for both series of reactions to verify the accuracy of the total energies obtained for different source phases. The relaxed lattice parameters for source and sink phases (determined using a GGA/PBE functional) are in satisfactory agreement with

experimental values (< 5%). All of the ΔE_{sub} values (*i.e.,* Eqns. 9-26) are positive and < 1 eV, and vary by as much as 0.34 eV, depending on the configuration. Regardless of composition, the most energetically favorable (*i.e.,* the least positive ΔE_{sub}) of the three configurations are those with interactions I or II (*i.e.,* Ag and its coupled substitution partner are nearest neighbors or next-nearest neighbors). The least energetically favorable configuration in all cases is configuration III. Coupled substitution in larger, 2×2×1, supercells (~3 wt% Ag) showed similar trends and values for ΔE_{sub}, and thus, interactions between adjacent unit cells were considered to have a minor effect on the ΔE_{sub} values shown in Eqns. 9-26. For comparison, ΔE_{sub} for the substitution of Ag for Pb (*i.e.,* $Ag^{+} + S^{-} \rightarrow Pb^{2+} + S^{2-}$ shown in Eqn. 27) is +2.30 eV (*i.e.,* ~2 eV more unfavorable than coupled substitution). It should also be noted that there are only minor differences (± 0.04 eV) between ΔE_{sub} values obtained from having either a single sulfosalt source phase (Eqns. 9-11) or two source phases (Eqns. 12-14), thus validating the energies obtained from these phases.

Figure 5.2A and Figure 5.2B show the structural relaxation of $Ag^{+} + Sb^{3+}$ substitution for two Pb^{2+} atoms in Pb_8S_8 in configurations I and III, respectively. For comparison, the structure for the substitution of $Ag^{+} + S^{-}$ for $Pb^{2+} + S^{2-}$ is shown in Figure 5.2C. In each coupled substitution case, the lowest-energy structure shows Ag coordinated to three of the S atoms from the original octahedral coordination of Pb. The three Ag-S bond lengths vary between 2.5 and 2.7 Å. In comparison, the position of the Ag atom in Pb_7AgS_8 is slightly offset from the original position of the Pb that it substituted for in

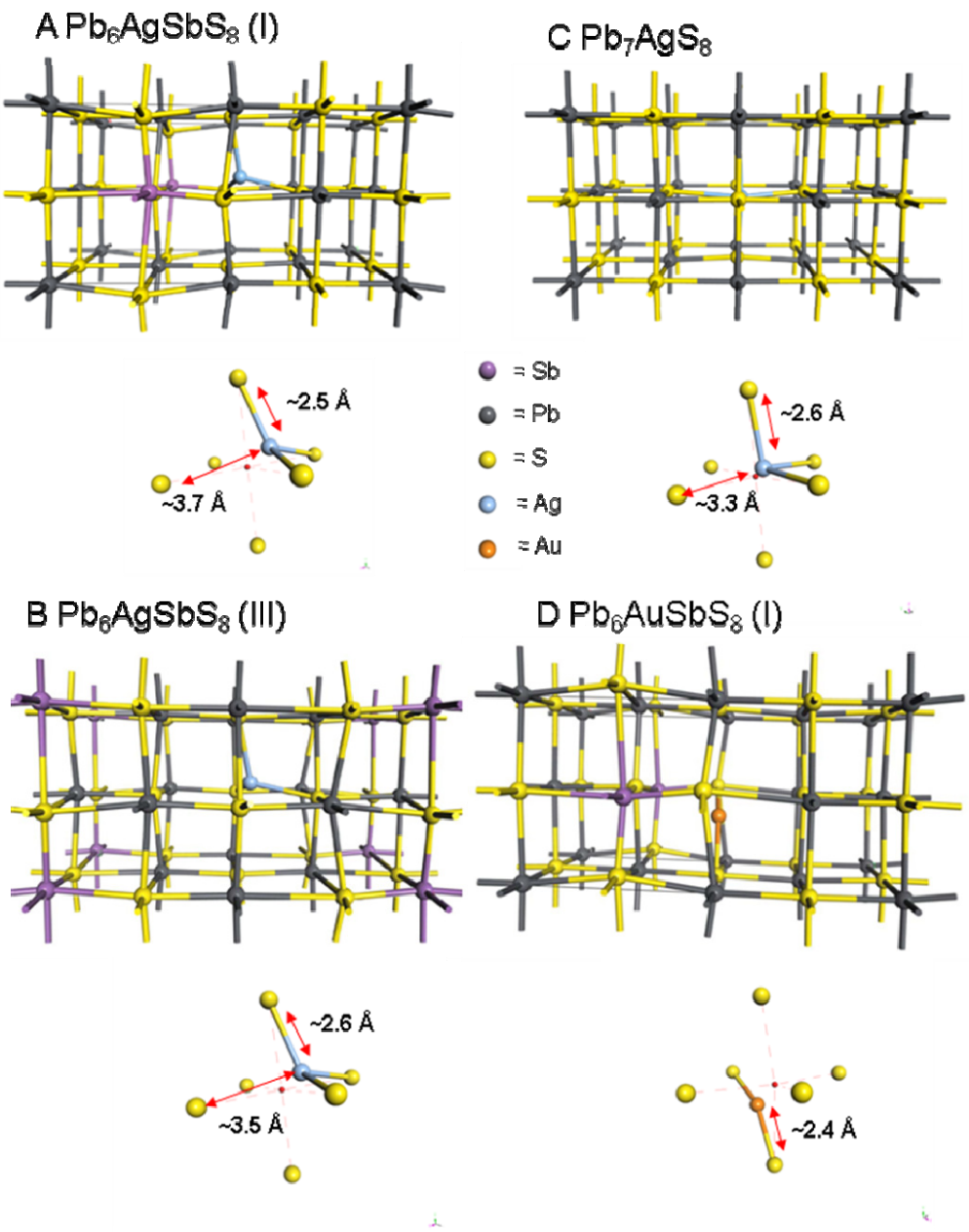

Figure 5.2. Ball-and-stick models of substituted galena 2x1x1 supercells. A) Pb_6AgSbS_8 *interaction I*, B) Pb_6AgSbS_8 *interaction III*, C) Pb_7AgS_8 *single substitution*, D) Pb_6AuSbS_8 *interaction I*. Insets below models show how the coordination environment and bond lengths for Ag or Au in the supercell above.

the structure, but not to the same extent as the coupled substitution case (comparing Figure 5.2A and Figure 5.2B with Figure 5.2C). Figure 5.2 shows the Mulliken charges (M.C.) of Ag and the Group 15 cation as well as the unit cell volume and change in u.c. volume for each substituted structure. In each structure (including Pb_7AgS_8), the M.C. of Ag is neutral to slightly negative (~-0.05 u.c.) relative to the M.C. of Pb (+0.7 u.c.) in Pb_8S_8. The M.C. of the Group 15 cation increases from As (~0.45 u.c.) to Sb (~0.68 u.c.) to Bi (~0.82 u.c.), a trend that is expected based on their electronegativity values. The M.C. of As, Sb, and Bi in coupled substitution structures are more positive than the values for single substitution (no Ag) of As (0.25 u.c.), Sb (0.47 u.c.), and Bi (0.53 u.c.) into Pb_8S_8, respectively. This suggests that partial charge transfer is taking place as part of the substitution mechanism and that Bi transfers more charge (~0.3 u.c.) than both Sb (0.21 u.c.) and As (0.20 u.c.). The largest deviations in unit cell volume are observed for Pb_7AgS_8 and Pb_6AgSbS_8 (III), but for most of the configurations, the unit cell volume deviates by less than 2%. Deviations in bond lengths and bond angles are most prominent for single substitution and for coupled substitution using interaction III (Figure 5.2).

Au coupled substitution:

In the case of coupled substitutions involving Au (*i.e.,* Eqns. 15-20), two series of reactions with separate source phases for Au and As/Sb/Bi are shown. In part, this is due to the lack of pure Au(I) sulfide and sulfosalt mineral phases in nature (Barton 1980). In reactions 15-17, a silver-gold chalcogenide, uytenbogaardite (Ag_3AuS_2, tetragonal), was used as the source phase of Au. In order to balance the reaction when using a

Table 5.2. Mulliken charges for substituting cations, unit cell volume for substituted Pb_8S_8, and Δ in unit cell volume.

substitution partners→ ↓	M.C. (metal) / M.C. (Grp. 15 cation) /unit cell volume (Å^3) / Δ unit cell volume (%)		
	Ag	Au	Cu
single substitution	-0.01//421.84 (-3.3%)	-0.28//434.068	-0.1//432.65
As			
I	-0.01/+0.43/430.95 (-1.25%)	-0.30/+0.45/436.15 (-0.06%)	-0.13/+0.44/428.15 (-1.89%)
II	-0.08/+0.46/434.61 (-0.41%)	-0.33/+0.47/436.08 (-0.07%)	-0.15/+0.46/431.47 (-1.13%)
III	-0.04/+0.45/436.67(+0.06%)	-0.26/+0.47/445.35 (+2.03%)	-0.12/+0.44/433.64 (-0.63%)
Sb			
I	-0.04/+0.67/433.19 (-0.74%)	-0.25/+0.65/444.021 (+1.74%)	-0.13/+0.66/430.44 (-1.37%)
II	-0.07/+0.68/417.68 (-4.30%)	-0.25/+0.68/438.98 (+0.59%)	-0.15/+0.67/433.33 (-0.71%)
III	-0.05/+0.66/417.68 (-4.30%)	-0.260/+0.67/447.86 (+2.62%)	-0.12/0.67/434.10 (-0.53%)
Bi			
I	-0.05/+0.81/430.75 (-1.29%)	-0.27/+0.81/438.28 (+0.43%)	-0.14/+0.8/427.44 (-2.06%)
II	-0.06/+0.83/432.47 (-0.90%)	-0.29/+0.83/440.29 (+0.89%)	-0.14/+0.82/430.97 (-1.25%)
III	-0.05/+0.81/432.57 (-0.88%)	-0.27/+0.81/442.314 (+1.35%)	-0.13/+0.82/430.07 (-1.45%)

phase containing Ag and Au, a sulfosalt source phase, and a sink for Ag were also included in the reaction. In reactions 18-20, the source of Au is a synthetic Au_2S phase with a cuprite-type structure previously described by Ishikawa *et al.* (1995). Equations 15-20 list the ΔE_{sub} values for Au substitution reactions for each of the three configurations. The ΔE_{sub} values are all positive and less than 1 eV. ΔE_{sub} values are energetically unfavorable (by ~ 0.2 eV) for the reactions 18-20, presumably due to the metastability of Au_2S and the inability of GGA/PBE to predict an accurate ground state energy (Ishikawa *et al.*, 1995). For comparison, ΔE_{sub} for the single substitution of a Au atom for Pb is 2.88 eV (Eqn. 28).

Figure 5.2D shows $Au^+ + Sb^{3+}$ substituted for 2 Pb^{2+} atoms in Pb_8S_8 for interaction II. The coordination environment of Au, in the substituted galena, differs from that of Ag in that it bonds to only two of the original octahedral S atoms (instead of 3 as in the case of Ag) with a Au-S bond length of ~2.4 Å. Table 5.2 shows the changes in unit cell volume associated with Au substitutions. The M.C.'s for Au are between -0.25 and -0.30 u.c. relative to Pb (+0.7 u.c.).

Cu coupled substitution:

In the case of coupled substitutions involving Cu (*i.e.,* Eqns. 21-26), two series of reactions are shown. Eqns: 21-23 contain an orthorhombic sulfosalt as the source phase for Cu: chalcostibite ($CuSbS_2$, *Pnma*) is used for Cu^++Sb^{3+}, emplectite ($CuBiS_2$, *Pnma*) for Cu^++Bi^{3+}, and $CuAsS_2$ *Pnma* is used for Cu^++As^{3+}. Eqns. 24-26 contain monoclinic chalcocite (Cu_2S) as the Cu source along with the sources for As, Sb, and Bi previously described. The values for each configuration vary only slightly (<0.05 eV) between the

different compositions and show the same trends in energy with interaction I being the most energetically favorable and III being the least. Cu has a M.C. of ~-0.14 u.c. in the structure and the unit cell volumes are all slightly lower than Pb_8S_8 (Table 5.2).

Electronic structure

The band gap for galena was determined to be ~0.6 eV, which slightly overestimates the experimental value of 0.3-0.5 eV from Tossell and Vaughan (1987), but is common using the GGA functional. Figure 5.3 shows the projected density of states (PDOS) for Ag substituting for a Pb in bulk galena (*i.e.,* $Ag^{+} + S^{-} \rightarrow Pb^{2+} + S^{2-}$) from the top of the conduction band to -6.0 eV into the valence band. The orbital-character of the main peaks in the PDOS for Ag (*i.e.,* resolved according to the angular momentum of the states) are also shown below in Figure 5.3. Overlaid with the PDOS of Ag *alone* is the PDOS for Ag when Sb, Bi, and As is present in a nearest neighbor site (*i.e.,* interaction I). The difference in the PDOS between Ag *alone* and Ag with a coupled substitution partner is a decrease of unoccupied states (*i.e.,* unoccupied Ag 5s and 3p

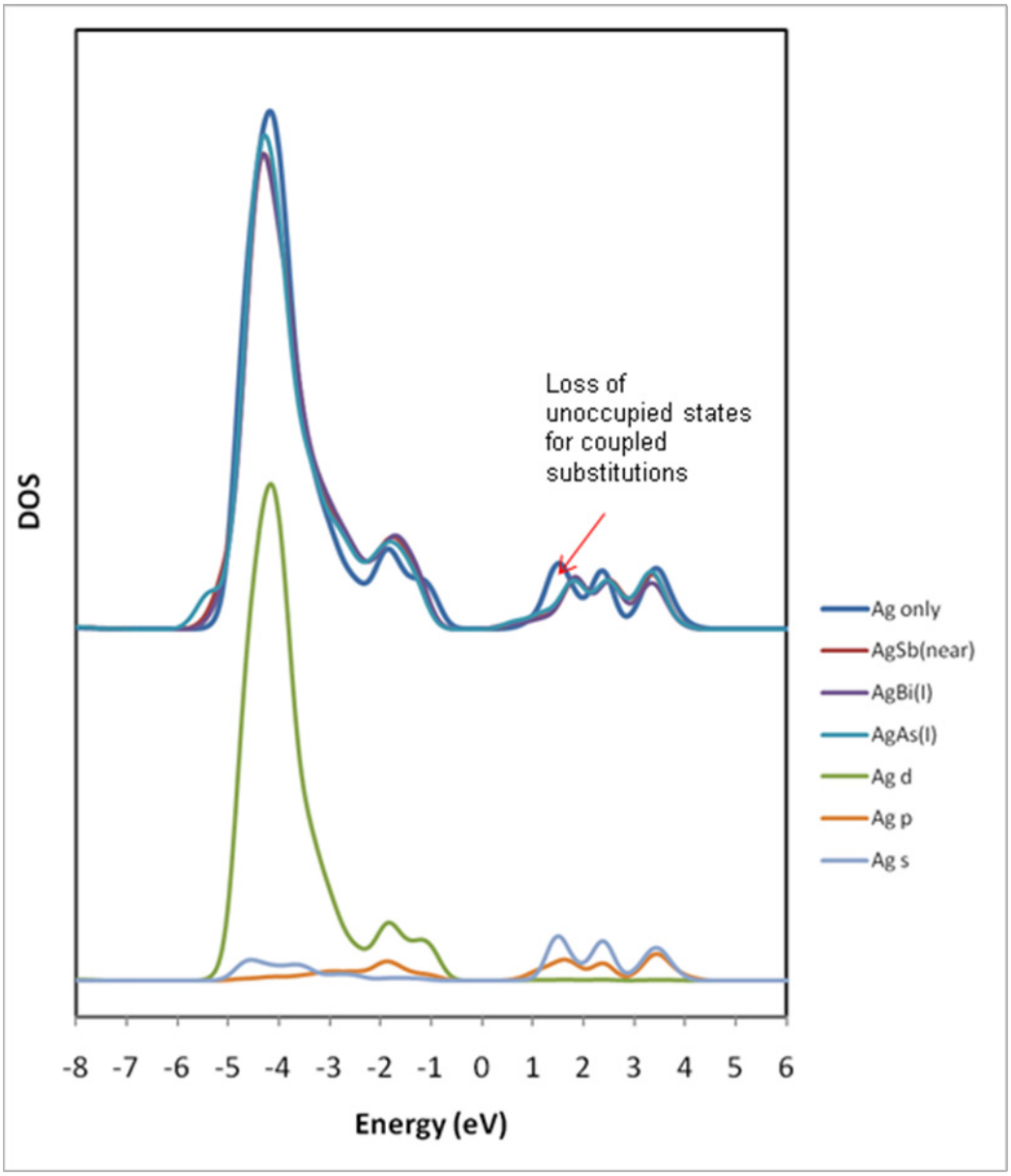

Figure 5.3. Projected density of states (PDOS) for Ag substituting for a Pb in bulk galena overlaid with PDOS for Ag when Sb, Bi, and As are present in a nearest neighbor site (interaction I). The orbital character of the main peaks in the PDOS is shown below for Ag (no substitution partner). The figure shows that when Ag is coupled with either Sb, Bi, or As there is a decrease in unoccupied states at the bottom of the conduction band.

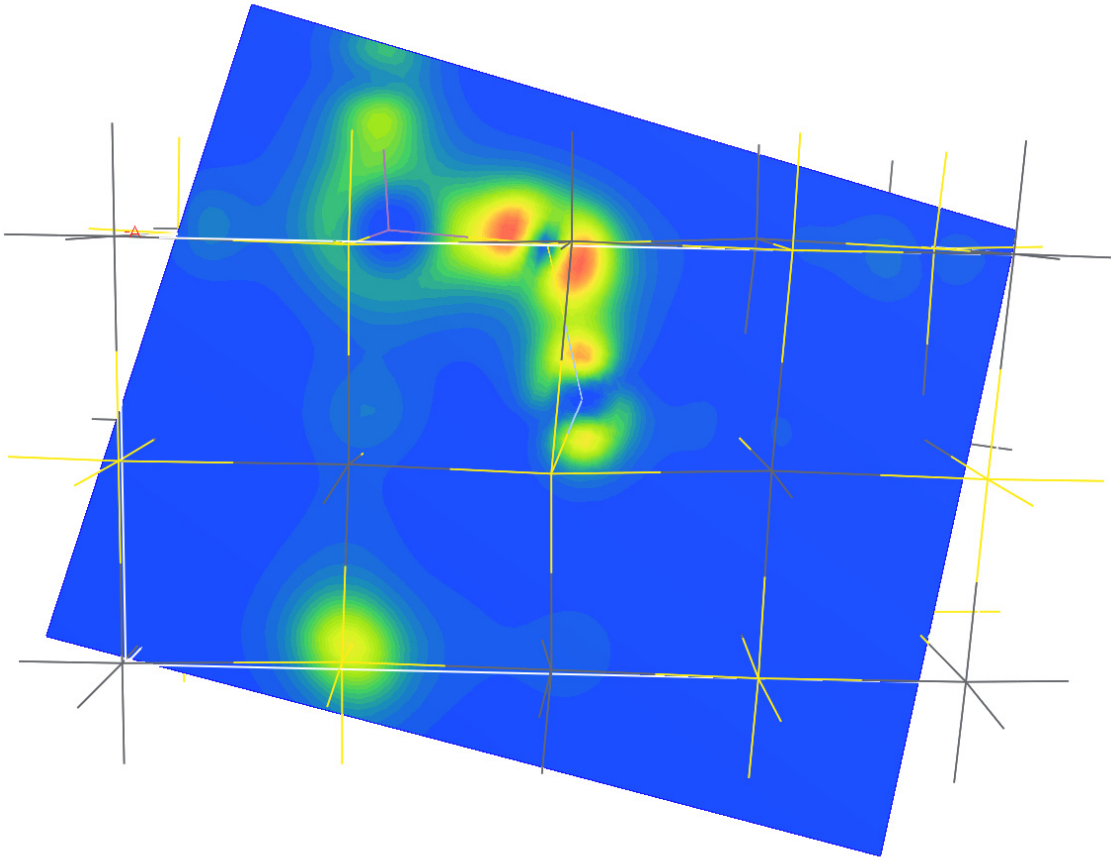

Figure 5.4. Two-dimensional contour map of the electronic structure of the $Pb_6AgSbS_8(I)$ between -3.5 and -4.5 eV below the Fermi level. 2-D map slices through the Sb, Ag, and the S that bridges them in the lattice. The positions in the original galena supercell are shown by the grey and yellow lines. Brighter areas show regions of shared electron density between Ag and Sb in the structure where charge transfer can take place.

states) at the bottom of the conduction band (indicated in the figure), between +1.0 and +2.0 eV above the Fermi level and a gain of states between 0 and -3.0 eV into the valence band.

Figure 5.4 shows a two-dimensional contour map of the electronic structure of the AgSb-substituted galena (i.e., interaction I) between ~-3.5 and -4.6 eV below the Fermi level. The slice is oriented in such a way to show the electron density in a plane fit through Sb and Ag and includes the S that bridges the two in this configuration. Regions of shared electron density between Sb (4p states), S (2p states), and Ag (5s states) show up bright in the 2-D contour. The hybridized molecular orbital shows a direct path for electron transfer from Sb to Ag via a bridging S atom in galena.

Enthalpy of mixing in galena

The excess enthalpies of mixing (ΔH_{mix}) for $AgSbS_2$-Pb_2S_2, $AgBiS_2$-Pb_2S_2, and $AgAsS_2$-Pb_2S_2 solid solutions are presented in Figure 5.5(A-C). All of the compositions are constrained within the original galena cubic framework. The plots are presented as a function of the molar fraction of $AgMS_2$, X_{AgM} (where M = As, Sb, or Bi), and temperature T. In the $AgSbS_2$-Pb_2S_2 series (A), the enthalpy shows one minimum at $X_{AgSb} = 0.5$, for T < 900 ˚C. Both $AgBiS_2$-Pb_2S_2 (B) and $AgAsS_2$-Pb_2S_2 (C) show different enthalpy characteristics than the $AgSbS_2$-Pb_2S_2 curve. The $AgBiS_2$-Pb_2S_2 series (B) shows only a slight enthalpy change at temperatures below 900 ˚C. At 200 ˚C (B), the two most negative points of the enthalpy curve are ~6 kJ/(mol exchangeable cations) more energetically favorable than the end members. The enthalpy curve for $AgAsS_2$-Pb_2S_2 (C) reaches a minimum at $X_{AgAs} \geq 0.625$ indicating that, in general, it

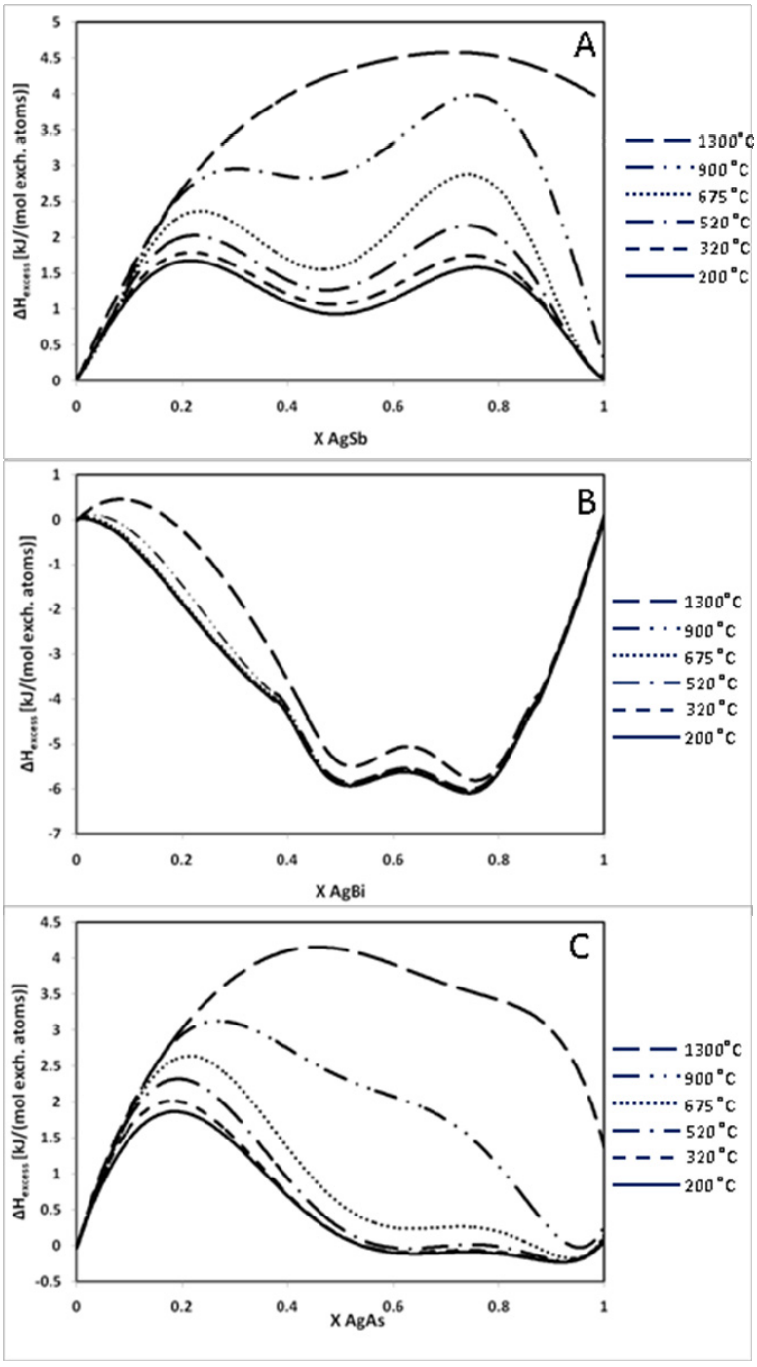

Figure 5.5. Enthalpy of mixing (ΔH_{mix}) for A) Pb_2S_2-$AgSbS_2$, B) Pb_2S_2-$AgBiS_2$, and C) Pb_2S_2-$AgAsS_2$. ΔH_{mix} is shown for six different temperatures.

is energetically more favorable to substitute 2 Pb^{2+} into the $AgAsS_2$ end member than to substitute Ag + As into the Pb_2S_2 end member.

Configurational entropy

The configurational entropy of mixing (ΔS_{mix}) for $AgSbS_2$-Pb_2S_2, $AgBiS_2$-Pb_2S_2, $AgAsS_2$-Pb_2S_2 series was obtained from the relation $\Delta G = \Delta H - T\Delta S$ and is shown in Figure 5.6(A-C). The magnitude of the reduction in ΔS_{mix} from the point entropy curve (*i.e.,* T_∞ in Figure 5.6A-C) indicates the degree of ordering within the system. All three solid solutions show ordering over a wide compositional range between 900 – 200 ˚C. The $AgSbS_2$-Pb_2S_2(A) and $AgAsS_2$-Pb_2S_2(C) series show ordering that extends from the non-galena end member to $X_{AgSb} = 0.07$ and $X_{AgAs} = 0.05$, respectively. The non-galena end members for the ΔS_{mix} curves in A and C show a decrease in ΔS_{mix} of 1.4 and 1.0 kJ/(K·mol·exchangeable cations), respectively, indicating some degree of cation ordering. $AgBiS_2$-Pb_2S_2 shows ordering across the entire compositional range, but less at $X_{AgBi} > 0.5$ than the equivalent concentrations for Ag-Sb and Ag-As. In the case of Ag-Bi, the ordering is less dependent on temperature than Ag-S and Ag-Sb, in that order.

Gibbs free energy of mixing in galena

Figure 5.7(A-C) shows the excess Gibbs free energy of mixing (ΔG_{mix}) for the $AgSbS_2$-Pb_2S_2 (A), $AgBiS_2$-Pb_2S_2 (B), and $AgAsS_2$-Pb_2S_2 (C) series calculated using a post-Monte-Carlo Bogoliubov integration scheme. Deviations from ideality in the free energy curves indicate limited solid solutions at $T \leq 675$ ˚C for all three solid solution series. The $AgSbS_2$-Pb_2S_2 series (A) shows two positive deviations in the free energy curves indicating miscibility gaps to the left and right of $X_{AgSb} = 0.5$ at $T \leq 675$ ˚C.

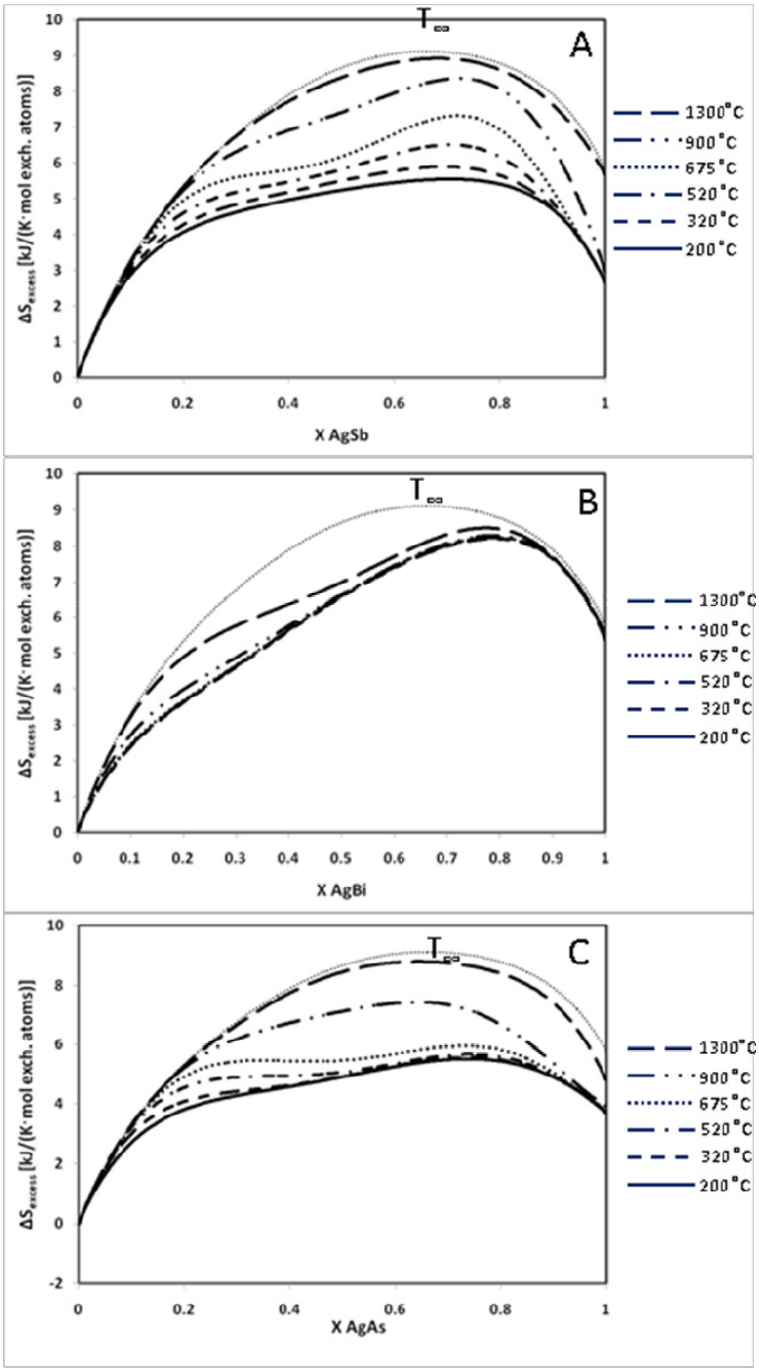

Figure 5.6. Entropy of mixing (ΔS_{mix}) for A) Pb_2S_2-$AgSbS_2$, B) Pb_2S_2-$AgBiS_2$, and C) Pb_2S_2-$AgAsS_2$. There is indication for some ordering in all three series as by the deviation of the entropy of mixing from the point entropy (T=∞).

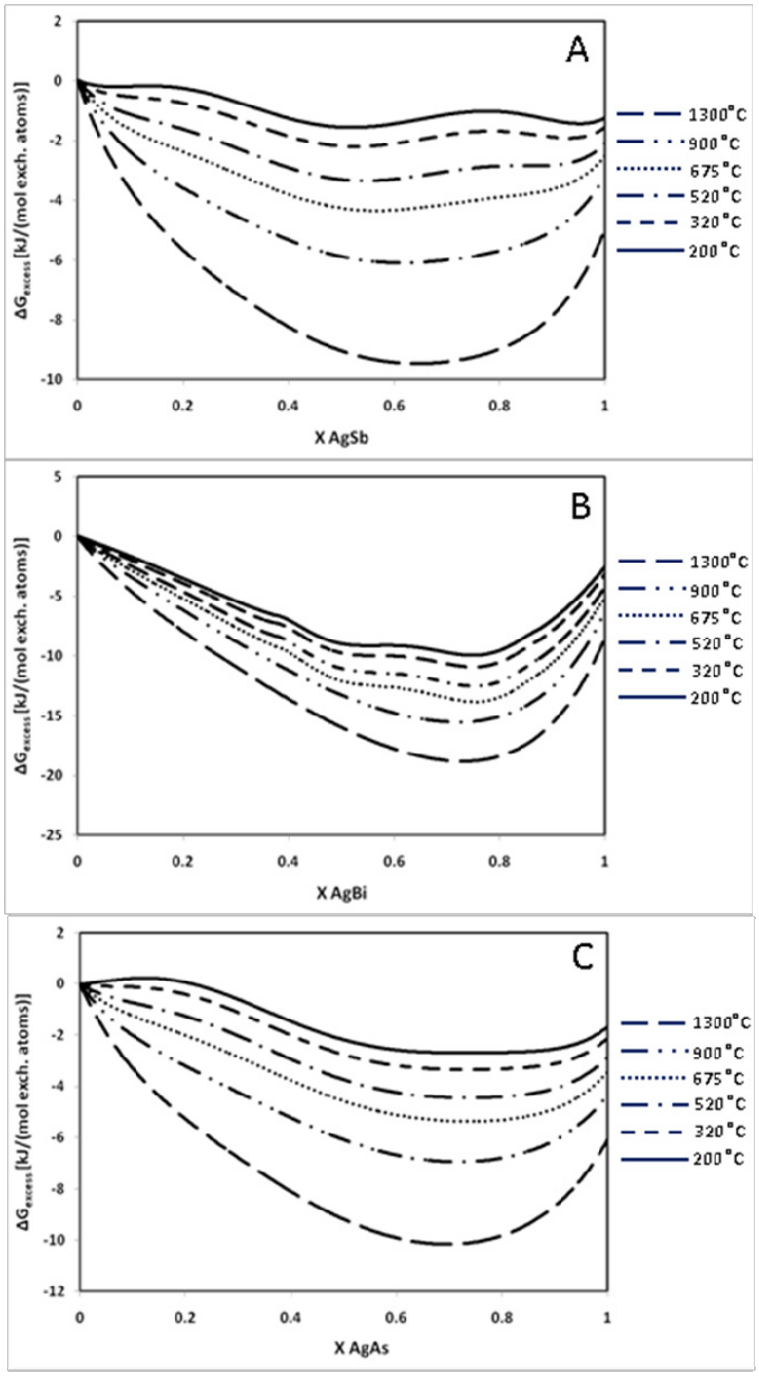

Figure 5.7. Free energy of mixing (ΔS_{mix}) for A) Pb_2S_2-$AgSbS_2$, B) Pb_2S_2-$AgBiS_2$, and C) Pb_2S_2-$AgAsS_2$. Deviations from ideality in the free energy curves indicate limited solid solutions in all three series.

Complete miscibility is shown at T ≥ 910 ˚C suggesting the existence of a phase boundary between 675 – 900 ˚C. The $AgAsS_2$-Pb_2S_2 series shows a miscibility gap at $X_{AgAs} < 0.55$ at T ≤ 675 ˚C with a phase boundary between 675 – 900 ˚C. $AgBiS_2$-Pb_2S_2 (B) shows two deviations in the free energy curves to the left and right of $X_{AgBi} = 0.5$ at T ≤ 675 ˚C.

From the free energy curves in Figure 5.7 and the deviations from ideality, phase diagrams can be generated for their respective solid solutions (shown in Figure 5.8)) by extending tie lines tangent to the two minima created by the deviation(s) in the free energy curves. Dashed lines show regions of the diagram where the phase boundary is not accurately known between 675 – 900 ˚C. In cases where the solubility near X = 0 is low, the solubility of Ag in galena is approximated by Eqn. 27 as described in Ferriss *et al.* (2008) (an error in the sign of the argument in Ferriss *et al.* (2008) has been corrected in Eqn. 30):

$$x_{Ag} = \frac{e^{\left(-\frac{\Delta H_1}{RTx_1}\right)}}{1 + e^{\left(-\frac{\Delta H_1}{RTx_1}\right)}} \tag{30}$$

Discussion

Ab initio quantum-mechanical calculations show that the coupled substitution of Ag^+ + (Sb^{3+}, Bi^{3+}, or As^{3+}) for two Pb^{2+} (Eqns. 9-14) is on the order of 2 eV more energetically favorable than the substitution of $Ag^+ + S^-$ for $Pb^{2+} + S^{2-}$ (Eqn. 27) in a 2×1×1 unit cell of galena (Pb_8S_8). The magnitude of the energy gained by coupled substitution is similar for reactions involving Au and Cu as the substituting metal

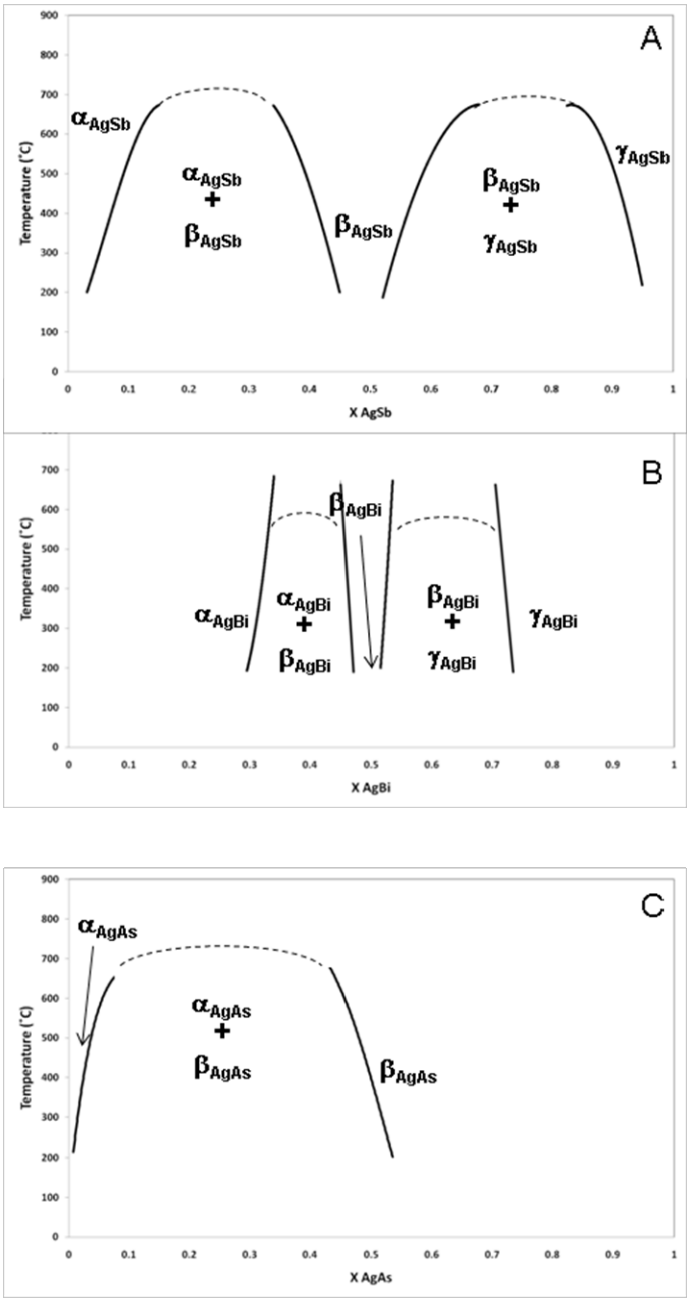

Figure 5.8. Calculated phase diagrams for A) Pb_2S_2-$AgSbS_2$, B) Pb_2S_2-$AgBiS_2$, and C) Pb_2S_2-$AgAsS_2$. A) The miscibility gap between x_{AgSb} = 0.05-0.45 consists of two phases, α_{AgSb} and β_{AgSb}, that are a galena-rich phase and a phase with a x_{AgSb} ~0.5 (with an ordering that is shown in Fig. 4.9), respectively. The γ_{AgSb} phase is AgSb-rich and forms a two-phase region with β_{AgSb} between x_{AgSb} = 0.5-0.95. Similar phase relations are shown for Pb_2S_2-$AgBiS_2$ (B) and Pb_2S_2-$AgAsS_2$ (C).

(Eqns. 15-26, 28,29). The unfavorable energetics associated with the single substitution of Ag into galena is supported by experimental studies which show Ag to be virtually insoluble in galena through the simple substitution of $2Ag^{+} \rightarrow Pb^{2+}$ [*i.e.,* maximum solubility ~0.4 mol.% at 615 ˚C (Van Hook, 1960)], but increasing to ~ 9 wt% (350-400 ˚C) when substitution is coupled with Sb and/or Bi. In addition, the total energy of the argentiferous galena lattice varies with respect to the Ag-(Sb, Bi, or As) atomic distance. Configurations in which the Group 15 cation is in a nearest-neighbor cation site (interaction I) are more energetically favorable than those in which Group 15 cation is further away (interaction III) as indicated by ΔE_{sub} values in Eqns. 9-26.

Charge transfer between substitutional donors, such as Sb, Bi, and As, and substitutional acceptors (*i.e.,* Ag, Au, and Cu), has been proposed as an explanation for the increased solubility of the metals in galena via coupled substitution mechanisms (Kroger, 1974). Mulliken charges for Ag (-0.05), Au(-0.27), and Cu(-0.14) are neutral or slightly negative relative to the values for Sb(+0.67), Bi(+0.81), and As(0.45) in the substituted unit cells. In addition, Mulliken charges for Sb, Bi, and As are ~2× more positive when substitution is coupled with a metal as opposed to single substitution, suggesting that the coupled substitution mechanism involves charge transfer. The Group 15 atom donates charge to nearby S atoms in the structure to satisfy charge of the reduced metal and ultimately partially to the reduced noble metal. Further evidence for charge transfer can be seen by comparing the projected density of state (PDOS) for Ag in the case of single and coupled substitution (Figure 5.3). The disappearance of unoccupied Ag 4p and 5s states at the bottom of the conduction band with a concomitant increase in

states up to 5.5 eV deep into the valence band is only present for coupled substitutions involving Sb, Bi, and As.

Figure 5.2 shows the structures of substituted Pb_8S_8. Significant distortions in bond lengths and in the octahedral coordination of the cations, when compared to the original galena structure, are apparent in the case of coupled substitutions (Figure 5.2 A-B, D). In the case of single Ag substitution (Fig. 4.2 C), the distortions are not as visible, because Ag occupies the Pb lattice position; however, the unit cell volume contracts by ~3.3% to accommodate Ag into the structure. The distortions are a result of the redistribution of electron density to accommodate reduced Ag (or Au or Cu) into the structure. These redistributions are possible due to the high degree of shared electron density within the structure. Distortions are localized within nearest-neighbor distances when the coupled species cluster together (shown in Fig. 4.2 A) as opposed to the distortions occurring throughout the P_8S_8 unit cell in Fig. 4.2(B). Charge transfer can occur more effectively through nearest-neighbor bonding as shown in the two-dimensional electron density contours in Figure 5.4. Thus, clustering due to charge transfer reactions between coupled-substitution partners results in structures that are more energetically favorable.

Monte-Carlo calculations were performed on each Ag series in order to assess whether or not short-range ordering due to redox interactions translates to long-range ordering at higher $AgSbS_2$, $AgBiS_2$, and $AgAsS_2$ concentrations. The trends described by quantum-mechanical results are reflected by the magnitude and the sign of the heterocationic interaction parameters (*i.e.,* Ag-Sb, Ag-Bi, and Ag-As) listed in Table 5.1. In this case, clustering (or ordering) is promoted (*i.e.,* negative *J*'s) by atomic-scale interactions between Ag and either Sb, Bi, or As. The *J*'s for both Ag-Bi and Ag-As

nearest neighbor (I) and next-nearest neighbor (II) interactions are all negative. Ag-Sb has a negative *J* for (I) and a positive *J* for (II). The extent of ordering and exsolution were determined from the ΔS_{mix} and ΔG_{mix}, respectively. There is indication for some ordering in all three series as shown in Figure 5.6 by the deviation of the entropy of mixing from the point entropy (T=∞), which indicates that the thermodynamic mixing properties and, thus, the extent of miscibility in these systems are affected by interactions between the substituting atoms. In the Ag-Sb case at $X_{Ag\text{-}Sb} = 0.5$ (T = 200 ˚C), Figure 5.9 shows the equilibrium configuration for the 2048 cation unit cell. S atoms are omitted from the figure so that the degree of cation ordering can be more easily shown. Ordering in this series is due to the formation of Sb-rich rows alternating with Ag-Pb-rich rows parallel to the ⟨100⟩ direction (or its symmetry-equivalents). The Ag-Pb-rich rows have an approximate composition of 33% Ag and 66% Pb. The equilibrium configurations at each binary composition (T = 200 ˚C) shows similar ordering with alternating Sb-rich rows. Similar ordering is present in the end member with miargyrite composition (not shown), which contains alternating rows of Ag and Sb parallel to the [100] and [010] direction and alternating cations along the [001] direction. This pattern gives rise to the hypothesis, due to the cubic nature of galena, that there may be nano-domains where the cations align in rows parallel to either the [100], the [010], or the [001] direction. A small degree of disorder is retained in the endmember with miargyrite composition and this is reflected by the nonzero ΔS_{mix} for the endmember in Figure 5.6.

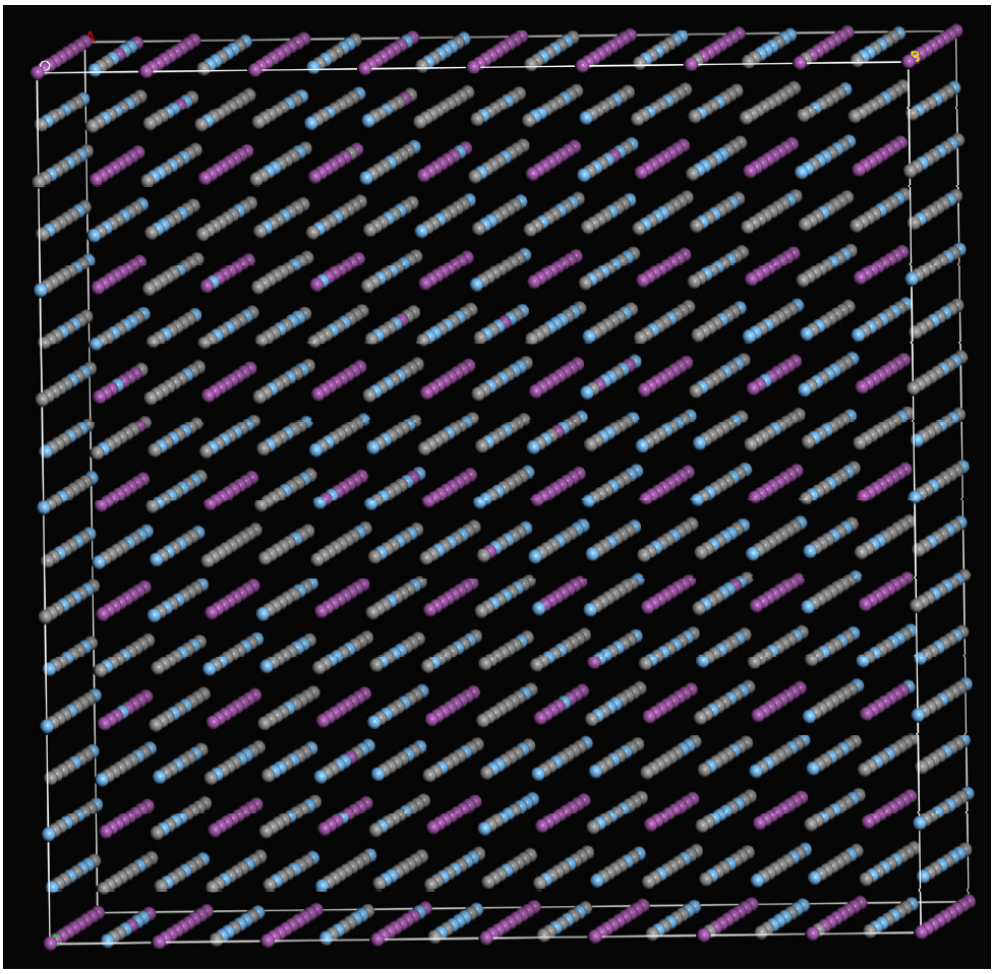

Figure 5.9. Ball-and-stick model of the 2x1x1 galena supercell (x_{AgSb} = 0.50, T = 200 ˚C). The model shows the most energetically favorable configuration from Monte-Carlo simulations. Sb(purple balls) forms alternating rows parallel to the ⟨100⟩ direction. In between Sb rows are rows rich in Ag (blue balls) and Pb (gray balls).

Exsolution within the miscibility gaps is shown in Figure 5.10 for $X_{Ag\ Sb} = 0.25$ (T = 200 ˚C). In this case, miscibility is due to the formation of a two-phase mixture consisting of Ag-Sb rich domains and galena-rich domains (identified in the figure). The presence of a two-phase field at this composition and temperature is consistent with the observations and interpretations of Hoda and Chang (1975), Nenasheva (1975), and Chutas *et al.* (2008) who show a phase with a high $AgSbS_2$ content and one with a lower $AgSbS_2$ content. Similar two-phase fields are present for Ag-Bi and Ag-As series with Ag-Bi-rich or Ag-As-rich domains approximately four atomic layers thick separated by Pb-rich domains (not shown).

The ordering in the Ag-Bi and Ag-As systems is similar to Ag-Sb showing alternating rows of Bi and As, respectively, separated by galena-rich rows parallel to ⟨100⟩. In addition, Ag-Bi and Ag-As show a degree of ordering that is not present in Ag-Sb with alternating Ag-rich and Pb-Bi-rich (or Pb-As-rich) layers parallel to the [111] direction (which, again, could lead to layered ordering into the symmetry equivalent direction in different domains, such that one could define this as layered ordering in the ⟨111⟩ family of direction). This type of ordering can be observed for $x_{Ag\text{-}Bi} = 0.5 - 1.0$, and is most clearly shown in the Ag-Bi endmember in Figure 5.11. The ordering shown in the [111] cannot be explained simply by differences in the ionic radii between Ag and the Group 15 atom. The Pauling's and Ahrens' radius for Ag^+ is 1.26 Å compared to the radii for Sb^{3+} (0.76 Å), Bi^{3+} (0.96 Å), and As^{3+} (0.58 Å) (Bloss, 1994). Using the difference in ionic radii as the sole criterion for ordering would predict Ag and Sb to order to a greater extent than Ag-Bi due to the greater difference in size. Monte-Carlo simulations show a different trend in ordering which is further evidence that electronic interactions may be

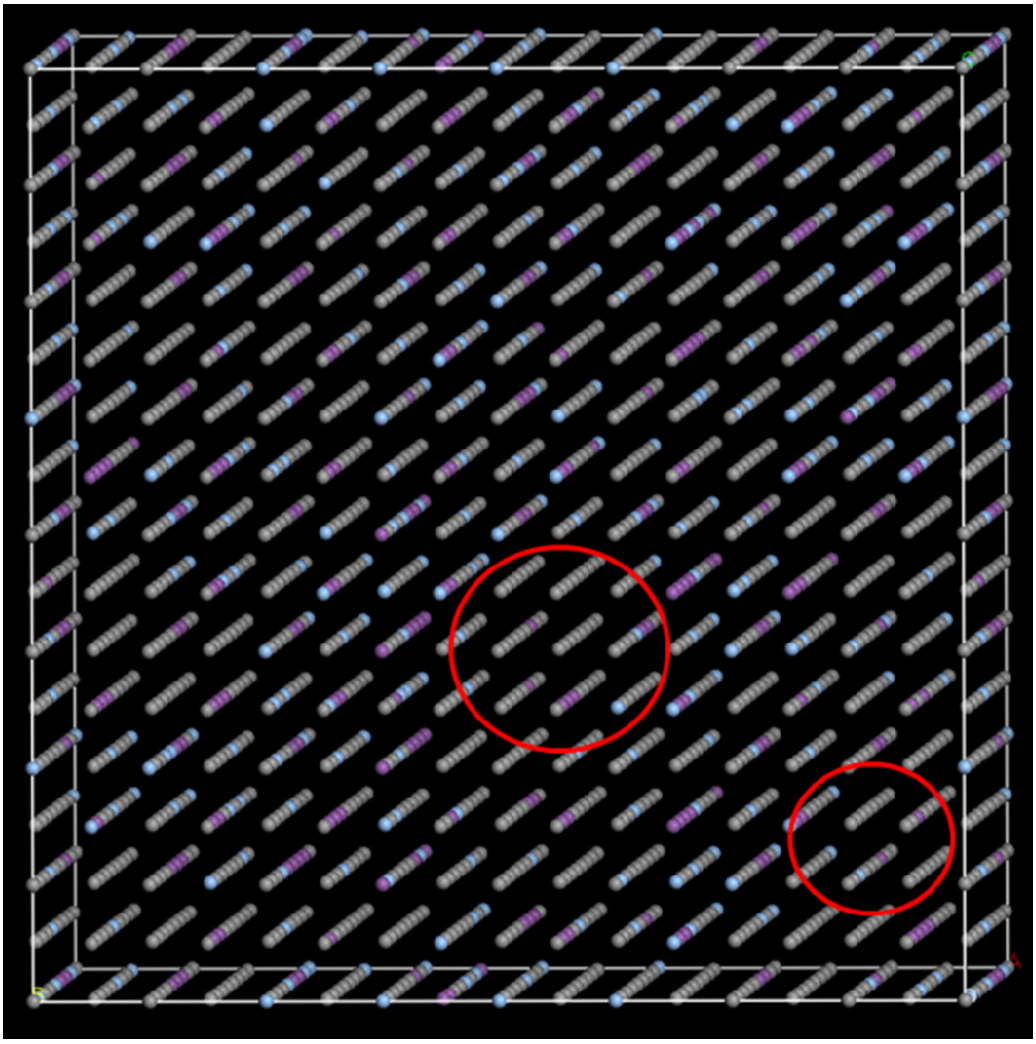

Figure 5.10. Ball-and-stick model of the 2x1x1 galena supercell (x_{AgSb} = 0.25, T = 200 ˚C). The models shows the most energetically favorable configuration from Monte-Carlo simulations for Sb(purple balls), Ag (blue balls), and Pb (gray balls). Miscibility shown in the phase diagram (Fig.4.8) for this composition and temperature is due to the formation of a two-phase mixture consisting of Ag-Sb rich domains and galena-rich domains. Red circles in the figure roughly define galena-rich domains in the supercell.

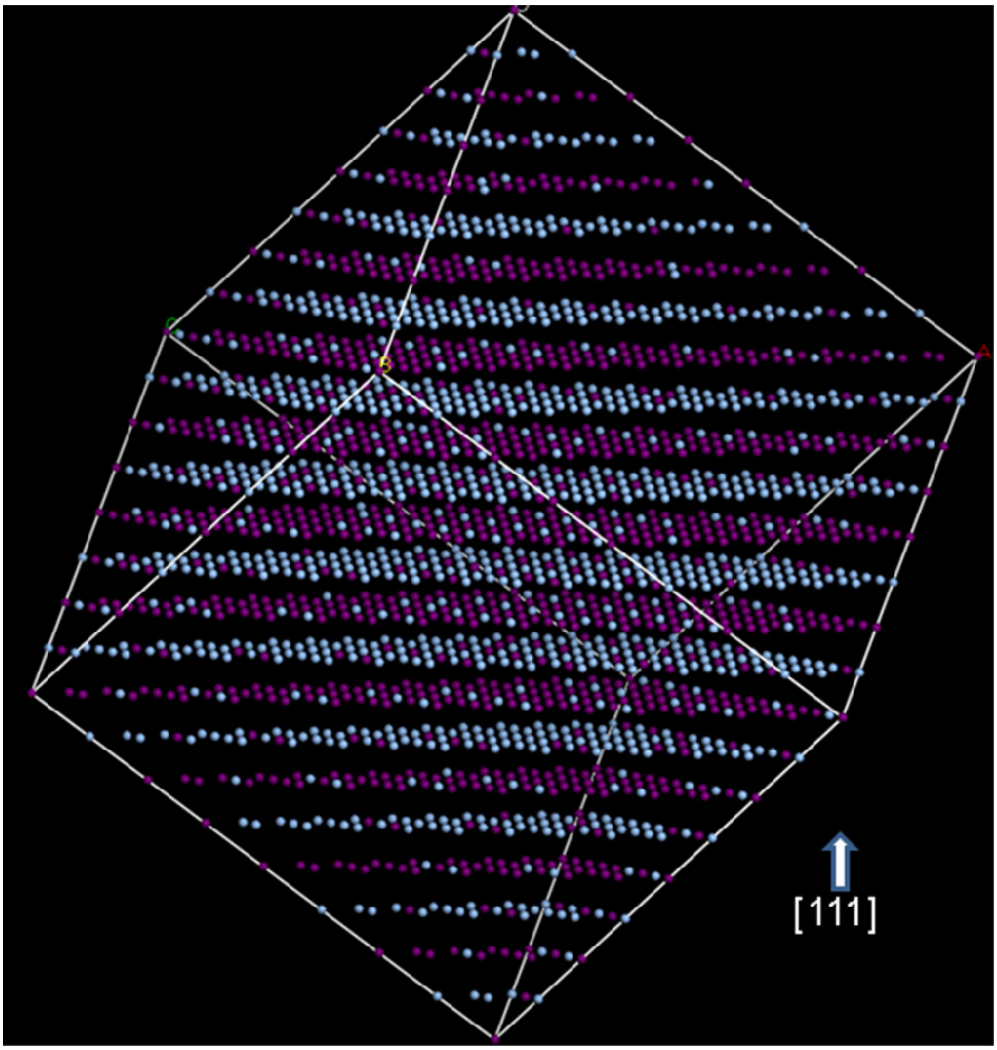

Figure 5.11. Ball-and-stick model of the 2x1x1 galena supercell (x_{AgBi} = 1.0, T = 200 ˚C). The models shows the most energetically favorable configuration from Monte-Carlo simulations for the end member with matildite composition: Bi (dark purple balls), and Ag (blue balls). The model is tilted on end so that the ordering of Bi-rich layers and Ag-rich layers parallel to the [111] is shown.

playing a role in the ordering within these systems and not just structural considerations based on ionic radii.

A comparison between the solubility of Ag in galena (*i.e.,* via coupled substitution with Sb) is shown in Table 5.3 between the Monte-Carlo simulation results from this study and experimental results by Chutas et al (2008) and Hoda and Chang (1975). Both experimental studies used an an evacuated glass capsule technique. Monte-Carlo simulations predict that at T = 350 ˚C, galena can contain 5.2 mol% of AgSbS in solid solution, and this is in reasonable agreement with experiments showing a value of ~5.5mol% of AgSbS. At T = 400 ˚C, our results indicate that galena can accommodate 7.1 mol% of AgSbS in comparison to ~12 mol% from experiment (Chutas *et al.*, 2008). Our results also indicate that the miscibility gaps for $AgSbS_2$-Pb_2S_2 and $AgBiS_2$-PbS_2 extend to higher temperatures than those determined from experiment. For example, our simulation results show that complete solid solution for $AgSbS_2$-Pb_2S_2 is only achieved at temperatures between 700-900 ˚C and above, whereas experiments indicate that complete solid solution is reached at T = ~430 ˚C. We propose three possible reasons for the differences between simulation and experimental results. First, simulations tend to overestimate the occurrence of exsolved nanodomains by underestimating interface energies between different phases. This is because, even though the chemical interaction across the interface is included in the interaction parameters and thus in the enthalpies obtained from Monte-Carlo runs, large-scale strain is not because it does not occur in the small unit cells used in the quantum-mechanical calculations. The overestimation of such exsolution nanodomains would artificially extend the miscibility gap to temperatures above the true temperature for complete solid solution. This may also be the reason that

Table 5.3. Solubility limit for $AgSbS_2$ in galena (mol %) determined from simulations and compared to experimental values. At 350 C°, our model results and experimental results for the maximum concentration of $AgSbS_2$ in galena are in reasonable agreement. Discrepancies between our model and experiment at low temperatures may be due to the extreme sluggishness of the kinetics at these temperatures. Deviations at higher temperatures may be due to our model not capturing the interface energy that must be overcome to form separate phases in the solid, and/or experimental analysis techniques not being able to spatially resolve nanoscale-size exsolved domains.

Temp. (°C)	**Chutas *et al.*, 2008 (mol %)**	**This study (mol %)**
450	Complete solid solution	10.0
400	12.0	7.1
350	5.5	5.2
250	1.0	4.0
200	0.5	3.1

the simulations predict two miscibility gaps in the Pb_2S_2-$AgBiS_2$ binary between $X_{Ag\text{-}Bi}$ = 0.3 and 0.8 whereas experiments show a complete solid solution at temperatures above 220 ˚C. A second possibility may be the extreme sluggishness of the reactions responsible for ordering in these systems. In the latter, both Chutas et al (2008) and Hoda and Chang (1975) acknowledge that experiments with potential unmixing may run for too short a period of time (max. 200 hours) and that equilibrium may not be fully achieved in the timeframe of the experiments. In natural systems this would be exacerbated by the fact that most sulfosalt minerals are deposited at low temperatures and late in the ore mineral sequence. A third possibility may be that the experimental methods used to characterize chemical variations in these materials (*i.e.,* optics, microprobe, XRD) do not have the spatial resolution to identify phases and exsolution features in the nanoregime. This has been shown to be the case in oscillatory zoning in garnets (Pollok *et al.*, 2001) and in compositional zoning in As-rich pyrite where high –resolution TEM observations show alternating pyrite and arsenopyrite lamellae with thicknesses on the order of 10 Å (Fleet *et al.*, 1989; Simon *et al.*, 1999). Palenik *et al.* (2004) has shown As-rich domains on the order of 20 nm surrounding Au nanoparticles.

Conclusions

Quantum-mechanical calculations were performed to evaluate the energetics of single and coupled substitutions using different incorporation mechanisms. These calculations show that it is energetically favorable for cation pairs (*i.e.,* AgM, AuM, or CuM, where M = Sb, Bi, or As) to be in nearest neighbor positions in the structure rather than farther apart. Based on these first-principles calculations, a Monte-Carlo simulation technique

was developed to calculate the thermodynamic mixing properties for coupled substitution mechanisms over the entire concentration range in these solid solutions. One result of these atomistic thermodynamic calculations is that the short-range ordering related to charge transfer processes between coupled substitution species affects the long-range ordering as shown from the deviations from the three-species point entropy for each series. Phase diagrams were determined for each solid solution series and a Ag solubility limit of 5.2 mol% of $AgSbS_2$ was determined to be in reasonable agreement with experiments showing a value of ~5.4 mol% $AgSbS_2$. The results demonstrate the applicability of quantum-mechanics and Monte-Carlo simulations as a tool to investigate coupled substitutions in sulfide systems. For instance, the results presented here are the first time the solubility of $AgAsS_2$ in galena has been quantified.

The results of this study may also be applied to understanding ordering and phase relations that result from coupled substitution in other sulfide systems. For example, extensive studies of arsenian pyrite from Carlin-type deposits reveal that incorporation of Au into pyrite structure is facilitated by a coupled substitution with As. Numerous investigators have shown that high Au contents are always correlated with As-rich compositions in natural and synthesized pyrites. In this case, Au can be in solid solution (*i.e.,* known as "invisible" gold) with a maximum Au/As molar ratio of 0.02 (Reich *et al.,* 2005); above this ratio, gold exists as nanoparticles of metallic Au^0 (Palenik *et al.,* 2004). Based on the donor-acceptor interaction for coupled substitution pairs in galena, we suggest the possibility that the solubility limit for Au defined by the Au/As molar ratio of 0.02 (*i.e.,* where one Au atom is related to 50 As atoms) may also be constrained by these interactions.

Acknowledgements

Support for this research was received from National Science Foundation NIRT Grant EAR-0403732.

References

Barton, M.D. (1980) The Ag-Au-S system. Economic Geology, 75, 303-316.

Becker, U., and Pollok, K. (2002) Molecular simulations of interfacial and thermodynamic mixing properties of grossular-andradite garnets. Physics and Chemistry of Minerals, 29, 52-64.

Becker, U., Fernandez-Gonzalez, A., Prieto, M., Harrison, R., and Putnis, A. (2000) Direct calculation of thermodynamic properties of the barite/celestite solid solution from molecular principles. Physics and Chemistry of Minerals, 27, 291-300.

Bloss, D.F. (1994) Crystallography and Crystal Chemistry. Mineralogical Society of America, Washington, D.C.205.

Bloem, J. (1956) Controlled conductivity in lead sulfide single crystals. Philips Res. Rep.,11, 273-336.

Bosenick, A., Dove, M.T., Myers, E.R., Palin, E.J., Sainz-Diaz, C.I., Guiton, B.S., Warren, M.C., Craig, M.S., and Redfern, S.A.T. (2001) Computational methods for the study of energies of cation distributions: applications to cation-ordering phase transitions and solid solutions. Mineralogical Magazine, 65, 193-219.

Chutas, N.I., Kress, V.C., Ghiorso, M.S., and Sack, R.O. (2008) A solution model for high-temperature PbS-$AgSbS_2$-$AgBiS_2$ galena. American Mineralogist, 93, 1630-1640.

Costagliola, P., Di Benedetto, F., Benvenuti, M., Bernardini, G.P., Cipriani, C., Lattanzi, P.F., and Romanelli, M. (2003) Chemical speciation of Ag in galena by EPR spectroscopy. American Mineralogist, 88, 1345-1350.

Dove, M.T. (2001) Computer simulations of solid solutions. European Mineralogical Union Notes in Mineralogy, 3, 225-250.

Fleet, M.E., MacLean, P.J., and Barbier, J. (1989) Oscillatory-zoned As-bearing pyrite from strata-bound and stratiform gold deposits; an indicator of ore fluid evolution. Economic Geology Monographs, 6, 356-362.

Foord, E.E., and Shawe, D.R. (1989) The Pb-Bi-Ag-Cu-(Hg) chemistry of galena and some associated sulfosalts - a review and some new data from Colorado, California and Pennsylvania. Canadian Mineralogist, 27, 363-382.

Foord, E.E., Shawe, D.R., and Conklin, N.M. (1988) Coexisting galena, PbS and sulfosalts - evidence for multiple episodes of mineralization in the Round Mountain and Manhattan gold districts, Nevada. Canadian Mineralogist, 26, 355-376.

Graham, A.R. (1951) Matildite, aramayoite, miargyrite. American Mineralogist, 36, 436-449.

Hackbarth, C.J., and Peterson, U. (1984) A fractional crystallization model for the deposition of argentian tetrahedrite. Economic Geology, 79, 448-460.

Hoda, S.N., and Chang, L.L.Y. (1975) Phase relations in systems PbS-Ag_2S-Sb_2S_3 and PbS-Ag_2S-Bi_2S_3. American Mineralogist, 60, 621-633.

Hohenberg, P., and Kohn, W. (1964) Inhomogeneous electron gas. Physical Review B, 136, B864.

Kroger, F.A. (1964) The chemistry of imperfect crystals. North-Holland, Amsterdam, 1039.

Metropolis, N., Rosenbluth, A.W., Rosenbluth, M.N., Teller, A.H., and Teller, E. (1953) Equation of state calculations by fast computing machines. Journal of Chemical Physics, 21, 1087-1092.

Myers, E.R. (1998) A statistical-mechanics model of ordering in aluminosilicate solid solutions. Physics and Chemistry of Minerals, 25, 465-468.

Palenik, C.S., Utsunomiya, S., Reich, M., Kesler, S.E., Wang, L.M., and Ewing, R.C. (2004) "Invisible" gold revealed: Direct imaging of gold nanoparticles in a Carlin-type deposit. American Mineralogist, 89, 1359-1366.

Payne, M.C., Teter, M.P., Allan, D.C., Arias, T.A., and Joannopoulos, J.D. (1992) Iterative minimization techniques for *ab initio* total-energy calculations - molecular-dynamics and conjugate gradients. Reviews of Modern Physics, 64, 1045-1097.

Perdew, J.P., Burke, K., and Ernzerhof, M. (1996) Generalized gradient approximation made simple. Physical Review Letters, 77, 3865-3868.

Pollok, K., Jamtveit, B., and Putnis, A. (2001) Analytical transmission electron microscopy of oscillatory zoned grandite garnets. Contributions to Mineralogy and Petrology, 141, 358-366.

Pridmore, D.F., and Shuey, R.T. (1975) The electrical resistivity of galena, pyrite, and chalcopyrite. American Mineralogist, 61, 248-259.

Reich, M., and Becker, U. (2006) First-principles calculations of the thermodynamic mixing properties of arsenic incorporation into pyrite and marcasite. Chemical Geology, 225, 278-290.

Reich, M., Kesler, S.E., Utsunomiya, S., Palenik, C.S., Chryssoulis, S.L., and Ewing, R.C. (2005) Solubility of gold in arsenian pyrite. Geochimica et Cosmochimica Acta, 69, 2781-2796.

Segall, M.D., Lindan, P.J.D., Probert, M.J., Pickard, C.J., Hasnip, P.J., Clark, S.J., and Payne, M.C. (2002) First-principles simulation: ideas, illustrations and the CASTEP code. Journal of Physics-Condensed Matter, 14, 2717-2744.

Sharp, T.G., and Buseck, P.R. (1993) The distribution of Ag and Sb in galena - inclusions versus solid-solution. American Mineralogist, 78, 85-95.

Simon, G., Kesler, S.E., and Chryssoulis, S. (1999) Geochemistry and textures of gold-bearing arsenian pyrite, Twin Creeks, Nevada; implications for deposition of gold in Carlin-type deposits. Economic Geology, 94, 405-421.

Tossell, J.A., and Vaughan, D.J. (1987) Electronic-structure and the chemical-reactivity of the surface of galena. Canadian Mineralogist, 25, 381-392.

Van Hook, H.J. (1960) The ternary system AgS_2-Bi_2S_3-PbS. Economic Geology, 55, 759-788.

Yeomans, J.M. (1992) Statistical mechanics of phase transitions, Oxford Science Publications, Clarendon Press, Oxford, 164.

Chapter 5

Conclusions

This thesis addresses fundamental questions concerning reaction mechanisms and geochemical processes involving sulfide minerals. The results and their implications show the importance of redox processes in some of the most abundant and widely distributed sulfide minerals in the near-surface environment. The implications of our results can be applied to a wide range of geochemical processes, from the interaction of aqueous species with nanoparticles (Chapter 2), to the importance of spin transitions on oxidation reaction rates (Chapter 3), to the formation of economically valuable sulfide ores (Chapter 4).

The results of Chapter 2 indicate that As(III) uptake from solution by mackinawite nanoparticles is strongly dependent on pH and redox conditions. Amorphous arsenic sulfide precipitates with "realgar-like" oxidation states were identified from HAADF-STEM and surface-probe techniques. Under the conditions of the study, the formation of amorphous arsenic sulfide particles accounts for the uptake of As(III) under acidic conditions. The characterization of these particles is significant because of the general lack of knowledge about the speciation and structure of arsenic solids in low-temperature

environments. This area is currently under intensive study with the goal of explaining or predicting the uptake and release of dissolved arsenic in natural waters. Our results are particularly significant in the light of findings by Lengke and Tempel (2003) that have shown the rate of oxidative dissolution of amorphous As_4S_4 is greater by a factor of 2 than that of crystalline realgar. In addition, As is deposited uniformly over the surface of mackinawite nanoparticles reacted at pH 9, providing further confirmation of studies by Gallegos *et al.* (2007, 2008) that show how the uptake mechanism for As changes under different pH conditions. Surface-probe results also indicate significant changes in the composition of the surface layers of mackinawite at pH 5 and pH 9. Understanding how the composition of the surface changes under different environmental conditions is essential to researchers/engineers who are modeling the removal of As(III) and other toxic elements (e.g., chromate and uranium) from groundwater using permeable reactive barrier technology.

The results of Chapter 3 highlight a significant oversight in the geochemical literature with regard to the key factors that control the oxidation rates of mineral surfaces. The magnitude of the activation-energy barriers due to spin transitions on surfaces is enough to alter the kinetics of surface mechanisms significantly. In this study, quantum-mechanical calculations show that at low pH (*i.e.,* no co-adsorbing hydroxide), the paramagnetic ($^3O_2$) to diamagnetic ($^1O_2$) spin transition is the rate-limiting step in the oxidation of As_4S_4. At high pH, the rate-limiting step is oxygen dissociation on the surface; however, the spin transition still contributes to the overall reaction rate. The theoretically calculated oxidation rate ($\sim 10^{-10}$ $mol \cdot m^{-2} \cdot s^{-1}$) is of the same order as empirically-derived rates from experiments at T = 298 K, pH = 8, and similar dissolved

oxygen concentrations. The attenuation of the activation energy by co-adsorbed anions suggests the possibility of pH- or p(co-adsorbate)-dependent activation energies that can be used to refine oxidation rate laws for sulfide minerals and other, especially semiconducting minerals, such as oxides.

The implications of this study extend beyond the dissolution-oxidation of As-bearing sulfides. We propose that similar spin transitions may dominate the oxidation kinetics of other sulfide mineral surfaces as well. Pyrite is the logical choice to investigate since it is the most abundant of all sulfide minerals and is often involved in the acidification of natural waters. It is known that the most important oxidants of pyrite are O_2 and Fe^{3+} and that the oxidation rate depends on the concentration of these two species. However, despite decades of research, the key controls of mechanisms and hence the rates of oxidation of pyrite remain poorly understood. The exact structure of the activated complex at the heart of the cathodic mechanism (*i.e.,* the rate-determining step) has not been previously detailed. It has been suggested that the activated complex might involve the transfer of an electron from Fe^{2+} in the mineral surface to a hydrated Fe^{3+} adsorbed from solution. The resulting hydrated Fe^{2+} is subsequently released back into solution and is replenished to Fe^{3+} by reaction with dissolved oxygen. The activation energy, E_a, for this overall reaction (without further specification whether the rate-controlling step is Fe^{3+} adsorption, electron transfer, release of Fe^{2+}, or finally the Fe^{2+}-to-Fe^{3+} re-oxidation in solution) has been determined to be in the range of 50-80 kJ/mol, and is high enough to support a chemical rather than a physical (*i.e.,* diffusional) control of the reaction rate (Williamson and Rimstidt, 1994). Based on our results which show the spin transition on As_4S_4 to have a similar E_a (~100 kJ/mol), we propose an alternative mechanism for the

cathodic reaction on pyrite that is based on the spin transition mechanism described in Chapter 2. In this case, adsorbed Fe^{3+} may act as a "spin catalyst" for the primary oxidant, O_2, rather than being the primary oxidant itself. In the case of oxidation by O_2, spin prohibition is involved in triplet O_2 approaching low spin surface of pyrite. The prohibition comes about because angular momentum must be conserved and the coupling of electron spins with the low spin surface is so weak that spin angular momentum is not readily exchanged in the timeframe of the O_2-surface collision. The proposed "spin catalysis" mechanism involving Fe^{3+} provides an alternative, lower energy pathway for the triplet to singlet transition, by accepting spin from the impinging O_2 molecule. We expect this mechanism resulting in oxidation rates that are proportional to the concentration of Fe^{3+} in solution. This hypothesis would have to be tested carefully on a number of sulfides at different environmental conditions (e.g., pH) and different co-adsorbates.

In addition to geologically important reactions, understanding the spin-transition mechanism and the conditions under which the activation energy barriers can be modulated could have profound impact on the development of heterogeneous catalysts, chemical sensors, anti-corrosion processes, photovoltaics, to name a few. For example, oxygen reduction catalysts could be developed to incorporate transition metal species that could act as spin catalysts in the same way that we propose Fe^{3+} to be acting on the pyrite surface.

Whereas Chapters 2 and 3 deal with redox processes on surfaces, Chapter 4 deals with electronic interactions or proximity effects between species some distance apart in the bulk, using galena as an example, and how these interactions affect the phase

relations and ordering in $AgSbS_2$-Pb_2S_2, $AgBiS_2$-Pb_2S_2 and $AgAsS_2$-Pb_2S_2. First, quantum-mechanical calculations were performed to evaluate the energetics of single and coupled substitutions using different incorporation mechanisms. These calculations show that it is energetically favorable for cation pairs (AgM, AuM, or CuM, where M = Sb, Bi, or As) to be in nearest neighbor positions in the structure rather than farther apart. Based on these first-principles calculations, a Monte-Carlo simulation technique was developed to calculate the thermodynamic mixing properties for coupled substitution mechanisms over the entire concentration range in these solid solutions. One result of these atomistic thermodynamic calculations is that the short-range ordering related to charge transfer processes between coupled substitution species affects the long-range ordering as shown from the deviations from the three-species point entropy for each series. Phase diagrams were determined for each solid solution series and Ag solubility was compared to experimentally determined values. Monte-Carlo simulations predict that at T = 350 ˚C, galena can contain 5.2 mol% of AgSbS in solid solution, and this is in reasonable agreement with experiments showing a value of ~5.5mol% of AgSbS. At T = 400 ˚C, our results indicate that galena can accommodate 7.1 mol% of AgSbS in comparison to ~12 mol% from experiment (Chutas *et al.*, 2008). Our results also indicate that the miscibility gaps for $AgSbS_2$-Pb_2S_2 and $AgBiS_2$-PbS_2 extend to higher temperatures than those determined from experiment. For example, our simulation results show that complete solid solution for $AgSbS_2$-Pb_2S_2 is only achieved at temperatures between 700-900 ˚C and above, whereas experiment indicate that complete solid solution is reached at T = ~430 ˚C (however, nanoscale exsolution at intermediate temperatures may not be

captured by experiment). The results presented here are also the first time the solubility of $AgAsS_2$ in galena has been quantified.

The results of this study may also be applied to understanding ordering and phase relations that result from coupled substitution in other sulfide systems. For example, extensive studies of arsenian pyrite from Carlin-type deposits reveal that incorporation of Au into pyrite structure is facilitated by a coupled substitution with As. Numerous investigators have shown that high Au contents are always correlated with As-rich compositions in natural and synthesized pyrites. In this case, Au can be in solid solution (known as "invisible" gold) with a maximum Au/As molar ratio of 0.02 (Reich *et al.,* 2005); above this ratio, gold exists as nanoparticles of metallic Au^0 (Palenik *et al.,* 2004).

Ab initio quantum mechanical calculations by Reich *et al.* (2005) show trends for the coupled substitution of Au and As in pyrite that are similar to those detailed in Chapter 4 for galena. In that study, their results reveal that the total energy of the auriferous arsenian pyrite lattice varies with respect to the Au-As atomic distance. Configurations, in which As atoms are clustered around an Au atom, are more energetically favorable than those in which an Au atom is in far vicinity to As atoms. Based on the donor-acceptor interaction for coupled substitution pairs in galena, we suggest the possibility that the solubility limit for Au defined by the Au/As molar ratio of 0.02 (where one Au atom is related to 50 As atoms) is also constrained by these interactions. For example, having >50 As atoms surrounding Au could provide enough charge to reduce the Au to a zero valence state and promote the formation of nanoparticle gold observed in experiment.

The results of the proposed research will improve the understanding of basic mineralogical questions such as the solid-state speciation of metals and metalloids in other sulfide minerals of different compositions (e.g., pyrrhotite, chalcopyrite, bornite, and tetrahedrite), coupled substitution mechanisms, and proximity effects in solid solutions of semiconducting sulfides. In consequence, this knowledge can be applied to a variety of geochemical problems such as the metallurgical recovery of ore metals, the formation conditions of hydrothermal ore deposits, and the redox processes involved in the release of toxic trace elements such as As into the environment, among others.

In addition, little is known regarding how these donor-acceptor interactions affect surface processes that are relevant to hydrothermal mineralization of galena ore deposits. Specific questions that are raised as a result of our research may include, "Does the presence of either a donor or acceptor adsorbed to, or incorporated within a semiconducting surface layer, perturb the surface electronic structure in such a way as to make adsorption of a second species more energetically favorable (or unfavorable)?" Such electronic-structure considerations are often considered when dopants are added to a semiconductor material to control whether the material is n-type or p-type, and thus the facility of oxidation or reduction reactions. However, rarely is this mechanism taken into account in natural systems to aid in understanding how impurities are incorporated during hydrothermal mineralization of semiconducting minerals. Answers to these questions will help to supplement the existing knowledge of how elements are transported and deposited in hydrothermal fluids.

References

Chutas, N.I., Kress, V.C., Ghiorso, M.S., and Sack, R.O. (2008) A solution model for high-temperature PbS-$AgSbS_2$-$AgBiS_2$ galena. American Mineralogist, 93, 1630-1640.

Gallegos, T.J., Han, Y.S., and Hayes, K.F. (2008) Model predictions of realgar precipitation by reaction of As(III) with synthetic mackinawite under anoxic conditions. Environmental Science & Technology, 42, 9338-9343.

Gallegos, T.J., Hyun, S.P., and Hayes, K.F. (2007) Spectroscopic investigation of the uptake of arsenite from solution by synthetic mackinawite. Environmental Science & Technology, 41, 7781-7786.

Ishikawa, K., Isonaga, T., Wakita, S., and Suzuki, Y. (1995) Structure and electrical properties of Au_2S. Solid State Ionics, 79, 60-66.

Lengke, M.F., and Tempel, R.N. (2003) Natural realgar and amorphous AsS oxidation kinetics, topical symposium on advances in oxide and sulfide mineral surface geochemistry, Hot Springs, Virginia, pp. 859-871.

Palenik, C.S., Utsunomiya, S., Reich, M., Kesler, S.E., Wang, L.M., and Ewing, R.C. (2004) "Invisible" gold revealed: Direct imaging of gold nanoparticles in a Carlin-type deposit. American Mineralogist, 89, 1359-1366.

Reich, M., Kesler, S.E., Utsunomiya, S., Palenik, C.S., Chryssoulis, S.L., and Ewing, R.C. (2005) Solubility of gold in arsenian pyrite. Geochimica et Cosmochimica Acta, 69, 2781-2796.

Williamson, M.A. and Rimstidt, J.D. (1994) The kinetics and electrochemical rate-determining step of aqueous pyrite oxidation. Geochimica et Cosmochimica Acta, 58, 5443-5454.